Investigating the effects of glass-fibre-reinforced polymer fabrics and bars on the flexural behaviour of sawn timber and glulam beams

by

Carmen Che

A thesis

presented to the University of Waterloo

in fulfilment of the

thesis requirement for the degree of

Master of Applied Science

in

Civil Engineering

Waterloo, Ontario, Canada, 2023

© Carmen Che 2023

Author’s Declaration

I hereby declare that I am the sole author of this thesis. This is a true copy of the thesis, including any required final revisions, as accepted by my examiners. I understand that my thesis may be made electronically available to the public.

Abstract

As climate change becomes an increasingly pressing issue worldwide, the buildings and construction industry remains to be a significant contributor to global carbon emissions. To address this, construction materials with high amounts of embodied carbon, such as cement and steel, may be substituted for more renewable resources, such as wood and mass timber, in applications beyond what was historically thought possible. Achieving this goal relies on a comprehensive understanding of their solid mechanics; to compensate for a lack thereof, modern building codes implement stringent, conservative restrictions on using these comparatively unfamiliar materials. These requirements, along with growing needs to design for more extreme loads (*e.g.*, seismic and blast), have prompted efforts to study and improve the performance of new and in-service wood structural elements, which themselves have evolved in recent decades beyond simply solid-sawn timber to include stronger, more efficiently engineered wood products such as glued-laminated (glulam) timber. One class of materials demonstrated to be well-suited for this task is fibre-reinforced polymer (FRP) composites, which come in a wide variety of forms and thus equally diverse applications.

The research presented herein investigates the effect of binding different types of glass-FRP reinforcement—specifically, in the forms of laminates of epoxy-impregnated glass-fibre fabric and of construction rebar—on the flexural behaviour different compositions of wood elements—specifically, sawn timber and glulam beams, composed of Spruce-Pine-Fir (SPF) No. 2, with dimensions of 140 mm × 140 mm × 2,025 mm and 110 mm × 140 mm × 2,025 mm, respectively. An FRP-to-wood ratio of 2% by cross-section area was used across eight reinforced specimens (two of each combination) for inter-comparison. An additional three control specimens were tested with no reinforcements to make a total of eleven beams in the study.

The results of the experiments found that the FRP fabric-laminates enhanced the strength by up to 52% and 36% in the sawn-timber and glulam beams, respectively. The bridging effect of natural defects in wood through the use of FRP as reinforcement resulted in a change in failure modes from the unreinforced beams. Due to cover requirements for FRP rebar, initial failure in this reinforcement configuration was still governed by the tensile strength of the extreme tension wood fibre; however, the stresses were subsequently transferred to the FRP bars, allowing for significant post-peak performance and greater overall sustained deformation. Analysis methods for predicting the strength of the reinforced beams were shown to be imprecise due to the highly variable nature of the natural wood material, demonstrating a need for larger sample sizes as well as tolerance for errors.

Acknowledgements

Heartfelt gratitude to all those who supported me, academically and personally, throughout the making of this thesis: my supervisor, Prof. Daniel Lacroix, for his valued academic guidance and for being my ever-patient advocate; my research colleagues, Maxime Cléroux, Tyler Hull, Benjamin O’Callaghan, and Yannick Vetter, whose precedents helped me navigate a pandemic edition of graduate studentship; the technical staff of the Advanced Materials and Structural Systems Laboratory at the University of Waterloo, particularly Robert Kaptein, Richard Morrison, and Peter Volcic, for imparting a wealth of knowledge in the hands-on aspects of structural research from specimen preparation to destructive testing; my engineering mentor, Dr. Sarah Wells, for constantly yet compassionately reminding me to keep things in perspective; my spouse, parents, in-laws, and dogs especially, for all their steadfast love, emotional support, and unwavering confidence in me.

The University of Waterloo acknowledges that much of our work takes place on the traditional territory of the Neutral, Anishinaabeg, and Haudenosaunee peoples. Our main campus is situated on the Haldimand Tract, the land granted to the Six Nations that includes ten kilometres on each side of the Grand River. Our active work toward reconciliation takes place across our campuses through research, learning, teaching, and community building, and is centralized within the Office of Indigenous Relations.

Table of Contents

List of Figures

List of Tables

Chapter 1
Introduction

1.1 General

Climate change is a pressing global issue with rapidly growing impacts (IPCC, 2018) which are not only limited to environmental concerns, but also far-reaching social, economic, and geopolitical interests, along with many others (IPCC, 2018). Consequently, there is an urgent need to reconsider, from various angles, where and how anthropogenic waste is generated, and to implement them with sustainable alternatives. The buildings and construction industry alone accounts for roughly 40% of global carbon emissions, of which roughly 28% is attributed to the production and distribution of construction materials (IEA, 2018). Cement and steel, namely, are major contributors to pollution, embodying a global warming potential equivalent to 0.94 and 1.27 kilograms of carbon dioxide (kg CO_2e) per kilogram of the respective material (C. Jones, 2019). In comparison, timber embodies just 0.49 kg CO_2e/kg; and being sourced from living, carbon-based materials, it also has carbon storage potential greater than its embodied carbon contribution, resulting in a net average reduction of 1.03 kg CO_2e/kg (C. Jones, 2019). Not only does wood contribute less pollution into the atmosphere, but it also sequesters it, making timber an ideal candidate for building greener structures.

Wood is one of the oldest known building materials in the world. History of its use spans millennia and has been evidenced in nearly all known cultures where it is or was available as a resource (Green, 2017). Wood continues to be used extensively in Europe and North America in low-rise residential buildings and short-to-medium-span bridges (Legg & Tingley, 2020; Ramage et al., 2017). Recent decades of advancements in engineered wood technologies have seen the application of wood in larger and increasingly complex structures all despite stringent modern design requirements. Among the properties that make wood a suitable structural material is that it is lightweight, possessing merely 5% the density of steel (CISC, 2021; Singh, 1987), yet having a comparable strength-to-weight ratio (Ramage et al., 2017).

However, the widespread use of wood structures remains vastly limited for reasons ranging from misplaced public perceptions to comparatively inadequate knowledge and experience with the material (Larasatie et al., 2018; Legg & Tingley, 2020). Furthermore, as wood infrastructure ages out and as new builds may strive for increasingly ambitious structural wood applications, it becomes of interest to study and establish reinforcement methods to enhance the mechanical properties, behaviour, and serviceable longevity of wood structures.

1.2 Research Needs

A suitable option for strengthening wood elements is to reinforce it using fibre-reinforced polymer (FRP) composites. As with wood, FRPs are very light and possess excellent strength-to-weight ratios; they also offer other benefits including durability, versatility of form, ease and speed of installation (Callister Jr. & Rethwisch, 2003), and compatibility with structural materials including wood and concrete (Legg & Tingley, 2020). Their use in construction has been well-established under the context of strengthening concrete elements under various types of loading—including compression (*e.g.*, Demers & Neale (1999), Hadi (2005), Micelli et al. (2001), Sulaiman et al. (2016), Y. Zhang et al. (2020), Zhou et al. (2019)), flexure (*e.g.*, J. A. Martin & Lamanna (2008), Nanni & Norris (1995), Tomlinson & Fam (2015), Triantafillou & Antonopoulos (2000), Yost et al. (2001), S. S. Zhang et al (2017)), seismic (*e.g.*, Iacobucci et al. (2003), Memon & Sheikh (2005)), and blast (*e.g.*, Buchan & Chen (2007), Jacques et al. (2015))—in various structural geometries, reinforcement configurations, and environmental conditions. The study of wood-FRP composites draws greatly from these concrete-FRP precedents and has become its own established field of study.

In terms of enhancing compressive strength, wrapping structural elements with FRP fabric wraps in confinement is a popular method for strengthening or rehabilitating wood columns, bridge piles, and abutments in situ (Caiza et al., 2012; Emerson, 2004; Kim & Andrawes, 2016). Full length confinement on cylindrical samples has been demonstrated by Chidiaq (2003), Najm et al. (2007), and Song et al. (2010) in agreement to improve peak strength, ductility, and durability in clear wood. In the interest of reducing the amount of reinforcing material required, Zhang et al. (2012) and Dong et al. (2015) experimented with applying only bands of FRP around wood columns, finding that such discontinuous confinement is also effective for increasing the load-carrying capacity. Studies by Song et al. (2010), Dong et al. (2015), and Kim & Andrawes (2016) showed that the ratio of FRP reinforcement applied in circumferential confinement is not directly proportional to the degree of compressive strengthening; however, André et al. (2013), by experimenting on small clear wood blocks, found this relationship between reinforcement ratio, strength, and also stiffness to be linear if the primary axis of the FRP wrap is applied parallel-to-grain rather than in the more conventional perpendicular-to-grain direction. Nevertheless, Heiduschke & Haller (2010) and O'Callaghan et al. (2021) observed that even small amounts of FRP confinement can increase the peak capacity to the extent of changing the failure mode of wood in compression.

The tensile strength in wood tends to be brittle compared to compressive strength, which is more ductile. This behaviour is critical for bending elements, and accordingly, the body of literature for reinforcing wood elements is largely focused on reinforcing wood members for flexure. Common applications for FRP-wood composites include the rehabilitation of timber bridges, particularly as a growing number of timber bridges throughout North America approach the end of their service lives (Buell & Saadatmanesh, 2005; CSA, 2019a; Gentile et al., 2002; Hay et al., 2006; Kim & Andrawes, 2016). Plevris & Triantafillou (1992) established that reinforcing just the tension face of a beam with a thin lamination of FRP comprising as little as 1% of the wood's cross-sectional area can result in substantial improvements to stiffness and flexural load capacity. These improvements may be attributed to the FRP bridging critical defects in the wood material. They also found that increasing the reinforcement ratio provides diminishing returns for strength and stiffness, levelling off after 3%, and concluded that the critical FRP reinforcement ratio is influenced by strain and stiffness ratios between FRP and wood. Johns & Lacroix (2000) and Gentile et al. (2002) were able to use this method to increase the ultimate flexural capacity by up to 50%, stiffness by up to 20%, and reduce overall variability due to the bridging of failure-inducing defects. Lindyberg & Dagher (2012) observed that 3% reinforcement ratios of this same configuration could increase the bending capacity of glued-laminated wood ("glulam") beams by over 100%. Raftery & Harte (2013) noted that glulam beams reinforced in this manner would develop evidence of compression failure, indicating increases in ductility.

One common issue with simple tension reinforcement in flexure, as reported by Dorey & Cheng (1996a, 1996b), Hernandez et al. (1997), and Lacroix & Doudak (2018a), is the sudden delamination of the FRP following failure in the wood tension surface. Lacroix & Doudak (2020), in experimenting with layering different FRP reinforcement schemes together on a single beam (*e.g.*, tension-only reinforcement with different types of confinements) with varying degrees of longitudinal continuity, found that the added confinement can limit crack development and delay wood-FRP debonding beyond peak resistance.

The use of FRP confinement is reintroduced for the benefit of shear reinforcement. Beams may be fully or partially confined (*e.g.,* to accommodate field applications in which some surfaces may be inaccessible), continuously or discontinuously, and with unidirectional or multidirectional FRP fabrics. Buell & Saadatmanesh (2005) found that confining timber beams with bidirectional FRP fabric results in significant improvements in the overall peak strength, stiffness, and deflection relative to beams without any reinforcement. Vetter (2022) applied combinations of FRP in full and partial confinement to glulam beams, and also compared the effects of confinement run continuously through the length with confinement added only to high-shear zones as "stirrups." Although the ultimate resistance was increased in all reinforced members, those reinforced with only simple tension laminates and partial half-depth confinement primarily failed in shear; however, when stirrups of full or gradated confinement were added, shear failure was partially contained and prevented premature debonding.

An alternative to reinforcing bending members with FRP fabric is using FRP rebar. FRP bars are often available with grooves or with a sand coating to develop adequate bonding shear. Gentile et al. (2002) studied the effect of near-surface-mounted GFRP bars on timber beams. Similar to fabric reinforcement, the bars bridged local defects, arrested crack opening, confined local rupture, and were able to transition the failure mechanism from brittle tensile failure to ductile compressive failure. Although debonding and delamination were common issues with tensile FRP fabric laminates on wood, Gentile et al. (2002) noted that FRP bars did not demonstrate this failure mechanism

Until mere recent decades, building codes did not have sufficient knowledge to safely permit tall or complex structures to be built with wood, opting instead to conservatively limit the size and scope of structures that can be built with wood. Advancements have since been made to understanding wood behaviour, engineered wood products, as well as reinforcing methods. However, despite growing popularity, much more must be investigated—and the resulting knowledge incorporated into design guidelines and building codes—before timber structures can compete more freely with concrete and steel structures in the interest of a more sustainable future. Additionally, as many existing wood bridges and structures approach the end of their serviceable lifespan, adequate knowledge of retrofitting methods can add years of usability, avoiding excess demolition and reducing costs. Insofar as FRP is a viable material to enhance wood behaviour, it remains a subject deserving of further study. Current research is lacking in the realms of how different forms of FRP influence different compositions of wood relative to one another. This knowledge would contribute to the ability to accurately model the effect of different combinations of wood and FRP, thus promoting their incorporation into codes and standards.

1.3 Research Objectives

The overarching aim of the research is to investigate the effects of types of wood products and fibre-reinforced polymer (FRP) reinforcement medium on the flexural behaviour of FRP composite beams subjected to four-point bending under static loading. More specifically, the goals are to

1. Investigate the effects of FRP fabric-laminate and FRP bars as simple tension reinforcement;
2. Determine the influence of wood product type—namely, sawn timber and glulam—on the flexural response when reinforced with FRP; and
3. Validate, compare, and adapt existing analysis methods for predicting the flexural behaviour of wood with or without FRP reinforcement in varying configurations.

1.4 Scope

The above-stated objectives are achieved through:

- Detailed literature review on the behaviour of wood subjected to static loading and the use of FRP as a strengthening material for wood structural elements;
- Review of analysis methods used for predicting the flexural capacity of wood beams reinforced with FRP;
- Testing wood and FRP coupons to determine base properties of the beam specimens to use as inputs for beam analysis;
- Testing a total of eleven full-scale sawn timber and glulam beams, unreinforced and reinforced with FRP fabric or bars, under four-point bending to establish resistance curves and failure modes;
- Analysis of the effects of wood composition and form of FRP reinforcement on flexural response;
- Discussion of results by comparing analytical and experimental results and proposing recommendations.

The scope of this project is limited to idealized boundary conditions to limit variables affecting the flexural response. Specific limitations of the research are further discussed through the thesis as well as the future recommendations section in Chapter 6.

1.5 Thesis Structure

The following provides a brief description of each chapter in this thesis:

- Chapter 1 introduces the subject and provides research needs, key objectives, and scope.
- Chapter 2 presents a detailed literature review comprised of studies investigating the behaviour of wood under flexural loading as well as the use of FRP as a reinforcing material for wood elements. Analysis methods for predicting the flexural behaviour of reinforced wood are also introduced.
- Chapter 3 presents the experimental methodology employed in the research program, including descriptions of the test specimens, their preparation, and the apparatuses used.

- Chapter 4 presents observations and data from the four-point bending tests on the control and reinforced wood beams. Coupon test results, used to obtain pure-tension and -compression data for the material components, are also provided.
- Chapter 5 discusses the results from the experimental program and how they compare to the predictive analysis methods.
- Chapter 6 concludes by summarizing key findings and proposing potential future work.
- Appendix A presents stress-strain data and failure images of the wood compression coupons.
- Appendix B presents stress-strain data and failure images of the wood tension coupons.
- Appendix C presents load-displacement data and images of key stages of failure progression of each of the flexural test specimens.
- Appendix D presents the relationship between load, displacement, wood-compression strain, wood-tension strain, and FRP-tension strain in each of the flexural test specimens.

Chapter 2

Background and Literature Review

2.1 General

This chapter presents a detailed review of existing research pertaining to wood and reinforced wood using fibre-reinforced polymer (FRP) composites. Provided below is an overview of wood and its use in the construction industry, alongside current knowledge of its material properties and behaviour under applied loading—specifically, tension, compression, and flexure. This is followed by a review of FRP composites, their compositions and mechanical strengths, and their use as strengthening and retrofitting materials for wood elements. Finally, analysis methods for predicting the flexural behaviour of FRP-reinforced wood are presented.

2.2 Wood as a Construction Material

2.2.1 Overview

Wood is a lightweight construction material with a high strength-to-weight ratio along with ease of constructability off- and on-site. As the only renewable major construction material, timber has seen revived and growing interest in recent decades as global attitudes shifted towards minimizing negative impacts on the climate crisis (IPCC, 2018). Its composition is of naturally embodied carbon captured from the atmosphere; in stark contrast, the production of concrete and steel, the predominant construction materials of the past decades, are heavily pollutive processes (Buchanan & Levine, 1999; Gustavsson & Sathre, 2006). When trees are harvested responsibly through sustainable forestry management programs and policies, the supply of wood can be ensured indefinitely for future generations. Canadian forests account for 362 million hectares—about 9% of the world's forested area—90% of which is publicly owned as Crown land. A total of 0.2% of the Canadian forest area was harvested in 2020, and less than 0.5% has been harvested since 1990 (Natural Resources Canada, 2022).

Exposed wood in a structure contributes to occupants' happiness, calmness, and creativity, a phenomenon known as biophilia (Demattè et al., 2018; Shen et al., 2020). However, common perceptions about the lifespan, maintenance, decay, fire resistance, vibration and acoustics hinder the uptake (Larasatie et al., 2018).

Building large timber structures in the old days relied on the availability of large trees to meet the required load demands. However, the logging of old-growth forests not only creates controversy but is unsustainable and particularly damaging to native ecosystems (Ramage et al., 2017). A modern alternative to large-sawn timber is the development of engineered wood products (EWPs), which use dimensional lumber glued together to form larger members, such as glued-laminated timber (glulam) and cross-laminated timber (CLT), as shown in Figure 2.1. Other common EWPs include parallel strand lumber (PSL) and laminated veneer lumber (LVL), both of which consist of small strands of wood bonded together to form larger cross-sections. EWPs offer advantages over sawn lumber in terms of strength; efficient use of material; and the ability to achieve large sections, greater lengths, as well as curved and tapered members. Low material weight also lends well to prefabrication options to cut costs by increasing construction speed and quality (Syed, 2020).

(a) Glulam beam (b) CLT panel

Reproduced from Canadian Wood Council (2022)

Figure 2.1: Common types of mass timber products

Member lengths may be achieved by joining sawn dimensional lumber end-to-end using adhesive and finger joints. Such joints are designed to be stronger than the wood itself so as not to create a weak point in the overall member. In glulam, for example, finger joints are offset between layers, as shown in Figure 2.2.

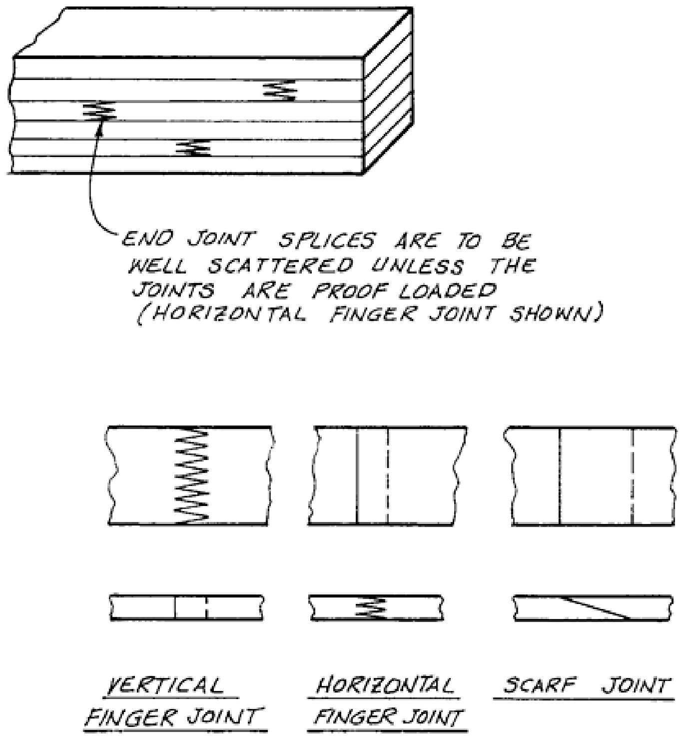

Reproduced from Breyer et al. (2015)

Figure 2.2: Finger jointing in glulam member

2.2.2 Material properties of wood

2.2.2.1 Anisotropy

Wood is an orthotropic material; its properties differ depending on the direction of loading. The cylindrical-polar shape and structure of a tree trunk lend to three mutually perpendicular axes: longitudinally along the stem, radially through the growth rings, and tangentially across the growth rings (Forest Products Laboratory, 2010). These axes are illustrated in Figure 2.3. Although all three are distinct, the two latter dimensions are often grouped to yield just two principal directions for engineering applications: parallel-to-grain and perpendicular-to-grain. There are two practical reasons for this simplification: first, their properties and behaviours are similar; and second, the precise cut used from the tree cannot be predicted from the design stage (Forest Products Laboratory, 2010).

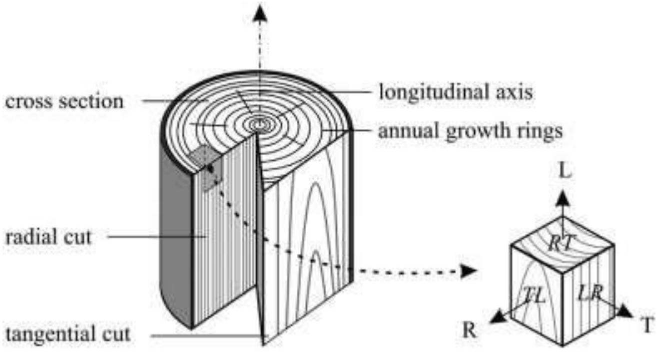

Reproduced from Legg & Tingley (2020)

Figure 2.3: Wood grain dimensions

Dimensional lumber is cut with its long dimension being parallel-to-grain to maximize use of the material. Another advantage of this practice is that the load capacity of wood is greatest when loads are applied axially (*i.e.*, in the parallel-to-grain direction) in compression, followed by loads applied axially in tension, whereas load capacity in the perpendicular-to-grain direction tends to be weaker for both compression and tension (Canadian Wood Council, 2017). These considerations are of particular importance in bearing and splitting scenarios, which typically imply the design for compressive perpendicular-to-grain loading (Canadian Wood Council, 2017).

Further physical distinctions can be found between sapwood and heartwood. Sapwood represents new, light-coloured growth on the outer cross-section leading up to the bark layer. Its porosity comes from its primary function to store and transport nutrients between the roots and leaves (Ramage et al., 2017). This same property lends itself to easier uptake of preservative treatment. As the tree grows, the need for structural support increases. Older wood cells die and fill with resinous materials and polyphenols to produce a decay-resistant, richly coloured, and denser core, also known as heartwood (Ramage et al., 2017).

2.2.2.2 Hygroscopy

Each wood cell is a long and hollow structure composed primarily of cellulose and lignin. The combined functions of these wood cells in the living tree are to store and transfer water and nutrients in addition to providing overall structure. Hence, wood is a hygroscopic and porous material (Legg & Tingley, 2020; Ramage et al., 2017). Moisture content in wood cells can be described as bound water and free water as shown in Figure 2.4. As wood dries, free water is lost first, followed by bound water. The fibre saturation point (FSP) marks the moisture content at which free water is completely drained from the wood cells and typically corresponds to 26-30% of its dry weight (Legg & Tingley, 2020). A significant consequence of changes in moisture content below the FSP is that its dimensions swell and shrink accordingly, particularly with ambient humidity during manufacture, construction, and while in service; above the FSP, such dimensional changes do not occur (Legg & Tingley, 2020).

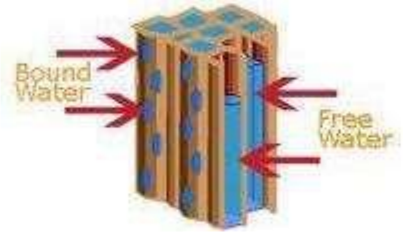

Reproduced from Legg & Tingley (2020)

Figure 2.4: Moisture in wood cells

Fluctuations in moisture level or ambient humidity result in dimensional changes in wood members, which in turn may induce additional stresses, which is a particularly important consideration in connection design. The rate of swelling or shrinkage is largest in the tangential direction, followed by the radial dimension, then in the longitudinal dimension (Legg & Tingley, 2020). When dried from the FSP to oven-dry conditions (*i.e.*, 0% moisture content), North American species undergo shrinkages of 5–13% tangentially and 2–7% radially (Canadian Wood Council, 2017; Forest Products Laboratory, 2010). This imbalance results in warping, cupping, cracks, or other distortions from the original cross-sectional shape of cut members (Legg & Tingley, 2020).

The strength of wood is inversely proportional to its moisture content, which varies with the ambient humidity in its service environment. A reduction factor is therefore applied for wood structures designed for service in wet conditions (*e.g.*, exterior applications where it can be exposed to precipitation or inside damp, humid rooms). If unprotected, exposure to excess moisture for prolonged periods may also lead to premature decay, therefore moisture management is critical to operational longevity (Legg & Tingley, 2020).

The ability of wood cells to take in moisture contributes to the viscoelastic property of wood (Breyer et al., 2015). Long-duration or cyclic loading can affect the strength of wood due to creep or fatigue, as shown in Figure 2.5, which describes the logarithmic decay of the bending capacity of wood beams sustaining load over time. Using a load duration of approximately 10 minutes as a baseline—a "standard-term" duration for common design situations—bearing a load for 60 minutes reduces its capacity to 90%; over several decades, the capacity falls to below 65% of the base load; and at the opposite end of the loading spectrum, if the duration is contained to merely one second, the same beam can resist 25% more than the base load (Breyer et al., 2015; Forest Products Laboratory, 2010). In the Canadian standard, *Engineering design in wood* (CSA O86), such "short-term" loads are assigned a load duration factor of 1.15, a conservative value which also accounts for construction loads up to seven days (*e.g.*, for formwork) (CSA, 2019b).

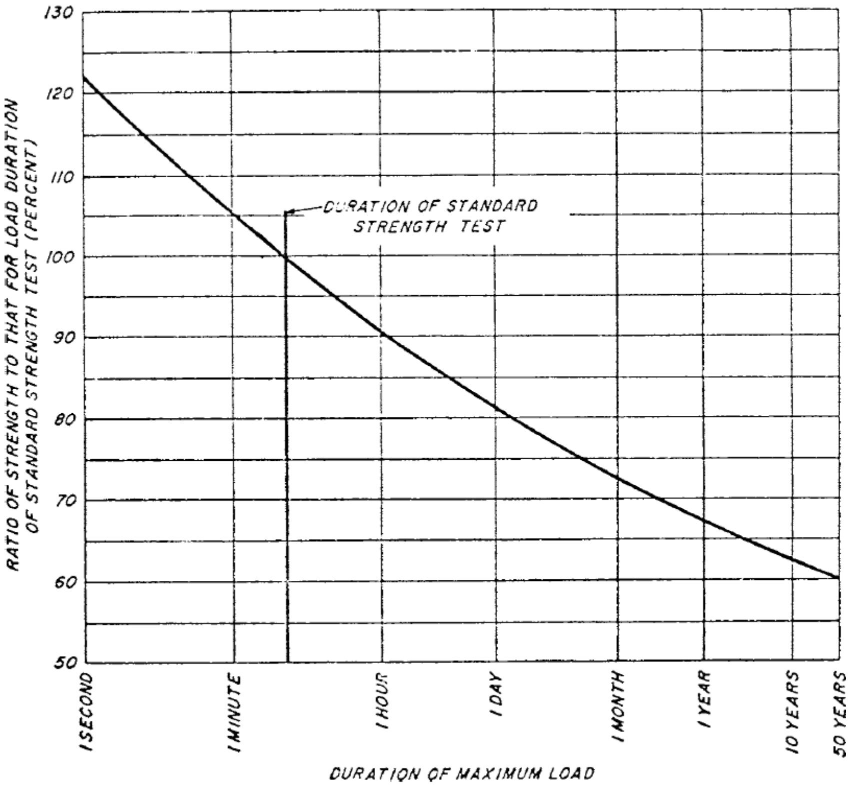

Reproduced from ASTM (2011a)

Figure 2.5: Load duration effects on the flexural strength of wood

2.2.2.3 Variability

Wood is commonly categorized broadly into hardwood and softwood species. Despite what these names imply, these categories are not distinguished by their hardness or density, but rather, by their botanical classifications. Hardwood is derived from angiosperm or flower-bearing trees, which are typically deciduous, and is more commonly used for furniture and flooring; softwood is derived from gymnosperm or cone-bearing trees, which are typically coniferous, and is more commonly used for structural members (Ramage et al., 2017). In most design guidelines, species are further sorted into groups with similar properties. The species combinations designated by CSA O86 are Douglas Fir-Larch (D Fir-L), which includes Douglas fir and western larch; Hem-Fir, which includes Pacific coast hemlock and amabilis fir; Spruce-Pine-Fir (SPF), which includes all species of spruce except coast Sitka spruce, Jack pine, lodgepole pine, balsam fir, and alpine fir; and Northern Species, which encompasses all other Canadian graded species (CSA, 2019b).

As an organic material, the environmental factors which a tree experiences in its lifetime have a significant impact on its material makeup, even within a single species. Variations in the growing conditions of each passing year—length of the growing season, daylight hours and intensity, temperature, humidity, available nutrients, wind, extreme weather, etc.—are reflected not only in a tree's growth or annual rings, but also in its grain density, grain straightness, and frequency of branches (Ramage et al., 2017). A tree's overall age and maturity also have an impact on the strength of its wood.

Random defects have a detrimental effect on the behaviour of wood. For example, knots, which are the result of branches forming off the main tree stem, create internal stress concentrations which may result in premature failure. In contrast, "clear" wood with no or few defects tends to behave more predictably and exhibits superior properties. Due to the inherently high variability of wood composition, and because defects are often not visible from the surface, determining the mechanical properties of wood is a relatively complex task (Barrett & Lau, 1994; Breyer et al., 2015; Forest Products Laboratory, 2010). In engineering design, the statistical likelihood of the presence of a strength-controlling defect is represented by applying a size factor based on the application (CSA, 2019b).

To further compensate for variability within species groups, grades or ratings are assigned to lumber. This process often takes the form of one of two general methods, visual inspection or machine rating, which have been verified against extensive test data (Barrett & Lau, 1994). Visually graded lumber considers the presence of surface defects in the wood (*e.g.*, twisted grains, knots, checks, and splits) as well as their intended application (*e.g.*, beams and stringers, columns and posts) (Canadian Wood Council, 2017). Machine stress-rated (MSR) and machine-evaluated (MEL) lumber are further categorized using non-destructive machine processes to measure the modulus of elasticity, which is then correlated to its strength. MEL differs from MSR in that it requires daily quality testing and control for tensile strength, bending strength, and stiffness (Brown & Woeste, 2022). The above grading methods are each capable of determining a modulus of elasticity in a piece of lumber, albeit with differing degrees of confidence; Figure 2.6 compares this variability based on wood which was evaluated to an average modulus of elasticity of 1.9 million psi (13 GPa) using different methods, demonstrating that the 5th percentile threshold for MSR lumber is greater than that of MEL lumber, which is greater than that of visually graded lumber (*i.e.*, grading variability is highest in visually graded lumber and lowest in MSR lumber). Although costlier, lower variability may be of particular importance in certain applications. For example, MSR lumber is often used for forming glulam beams due to the lower variability in this grading process (CSA, 2019b).

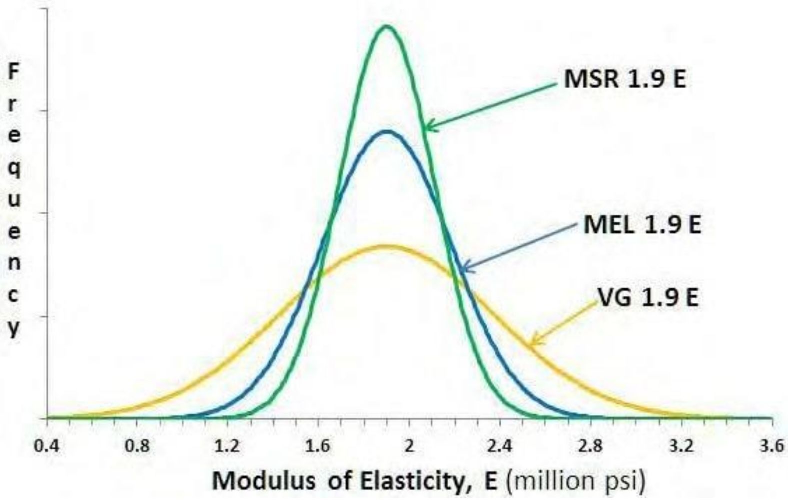

Reproduced from Brown & Woeste (2022)

Figure 2.6: MOE variation of different grading methods

2.2.2.4 Fire performance

Building developers and designers who are hesitant to build with wood frequently cite its combustibility as a primary concern (Larasatie et al., 2018). Great fires throughout history have felled entire cities as flames spread from one building to the next, and the aftermath often included a unified determination to legally restrict the widespread use of flammable materials in construction, as was the case following the Great Chicago Fire of 1871 (Pauly, 1984). There are some misconceptions in this logic, notably that unprotected steel loses much of its strength at temperatures well below combustion temperatures (Kodur & Naser, 2020). Wood structures, although indisputably combustible, can be engineered to behave quite predictably in fire events (Kodur & Naser, 2020; Legg & Tingley, 2020).

Fire performance is expressed in terms of a fire rating, which represents the duration in which structural stability can be ensured in the event of a fire. This design feature can buy the time necessary for building occupants to safely evacuate as well as for firefighters to arrive on the scene and perform rescue operations (Šulc et al., 2021). When combusted, exposed wood turns into a surface layer of char, which progresses inward at a predictable rate as temperatures remain elevated. Although char bears no strength, it serves as an insulating barrier that protects the underlying wood; the effective cross-sectional area of the member is reduced, but the intact core retains most of its original strength (Kodur & Yu, 2016). In light-frame wood construction, due to its relatively small initial cross-section, passive fire protection often relies on insulating building finishes such as gypsum board, fibreglass, or rock-wool insulation (Bénichou et al., 2002; Kodur & Naser, 2020). Such encapsulation methods may also be applied to mass timber, although it is not strictly necessary; fire performance in mass timber may be achieved by simply upsizing its dimensions such that a sacrificial outer layer can turn into char, allowing the underlying wood to continue bearing structural loads for a duration specified by the required fire rating (Kodur & Yu, 2016). This design approach allows the wood to remain exposed where aesthetically desired.

Chemical fire-retardant treatments for wood are available commercially in diverse formulations, employing a range of different mechanisms at elevated temperatures. Intumescent coatings can be brushed or sprayed onto exposed surfaces to insulate wood and prevent combustion. When exposed to elevated temperatures, these silica-based coatings expand and trap moisture within the element. For indoor applications, fire-retardant chemicals may be impregnated into the wood to inhibit the spread of flame, with the drawbacks of reducing wood strength, increasing char rate, and being unsuitable for wet service conditions including outdoor environments (Legg & Tingley, 2020).

2.2.3 Structural behaviour of wood under applied loads

2.2.3.1 Tension

The behaviour of wood under tension differs drastically whether the tensile loading is applied parallel-to-grain or perpendicular-to-grain. Parallel-to-grain tensile capacity is directly proportional to its cross-sectional area, and its behaviour is linear-elastic. Failure in tension parallel-to-grain is brittle, taking the form of wood grain rupture (Buchanan, 1990). Meanwhile, wood loaded in tension perpendicular-to-grain is usually considered by design guidelines to possess little capacity, its failure is also brittle and characterized by the fibres splitting away from each other (CSA, 2019b).

Tensile failure tends to govern design in both parallel- and perpendicular-to-grain directions. For example, in flexural applications, failure usually originates in the tension, hence flexural reinforcement strategies focus on strengthening the tension face (Plevris & Triantafillou, 1992).

2.2.3.2 Compression

The compressive strength of wood is strongest when loads are applied parallel-to-grain. Despite the compressive strength perpendicular-to-grain being substantially lower than the compressive strength parallel-to-grain, it is still greater than the tensile strength perpendicular-to-grain (Legg & Tingley, 2020).

The stress-strain behaviour of wood subjected to compression loaded parallel-to-grain can be described with a linear-elastic relationship up to yielding. Beyond this point, some level of residual strength is retained, the extent of which varies among models such as those shown in Figure 2.7. Neely (1898) proposed a simple elastoplastic model, which was elaborated upon by Malhotra & Mazur (1970) to address a softening effect observed in clear eastern spruce wood. However, neither of these models described the shape of the post-peak behaviour of wood under compression. Glos (1978) quantified the falling branch based on a comprehensive study of wood containing defects. Although this model was more representative of real behaviour, its parameters required calibration to the specific set of materials. Bazan (1980) simplified Glos' model into a bilinear model, with the slope of the softening portion parameterized later by Buchanan (1990).

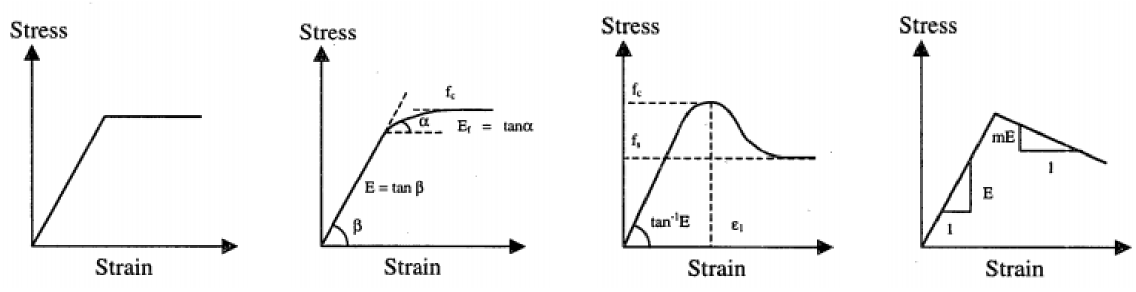

(a) Neely (1898) (b) Malhotra & Mazur (1970) (c) Glos (1978) (d) Bazan (1980) & Buchanan (1990)

Figure 2.7: Stress-strain behaviour models for wood under parallel-to-grain compression

Failure modes for clear wood specimens under compression parallel-to-grain can be categorized as crushing, wedge split, shearing, splitting, combined crushing-and-shearing, and brooming, as shown in Figure 2.8 (ASTM, 2021a). Crushing failure is characterized by a plane of rupture that is approximately horizontal (*i.e.*, perpendicular-to-grain). When the rupture is generally perpendicular-to-grain but not quite horizontal, it is considered a wedge split failure. Shearing failure is defined by a failure plane that is greater than 45° to the top of the specimen (or less than 45°-to-grain, if the grain is straight and parallel to the direction of loading). Splitting failure takes the form of a continuous longitudinal crack from end-to-end, parallel-to-grain, often originating from internal defects. Combined crushing-and-shearing is usually associated with cross-grained specimens in which the wood grains are not completely parallel relative to the direction of loading. Brooming or end-rolling failure occurs due to weak end conditions, a usual indicator of excess moisture and/or improper cutting. When occurring in small specimens, the former three failure modes (Figure 2.8a-c) are considered in ASTM D143 (2021a) as "acceptable" failures, whereas the latter three modes (Figure 2.8d-f) are general indicators of poor material quality and must be discarded.

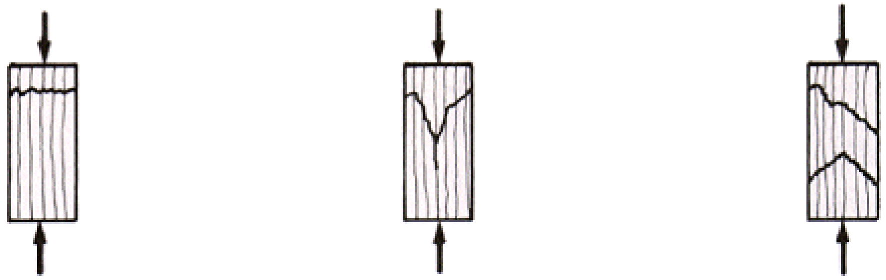

(a) Crushing (b) Wedge split (c) Shearing

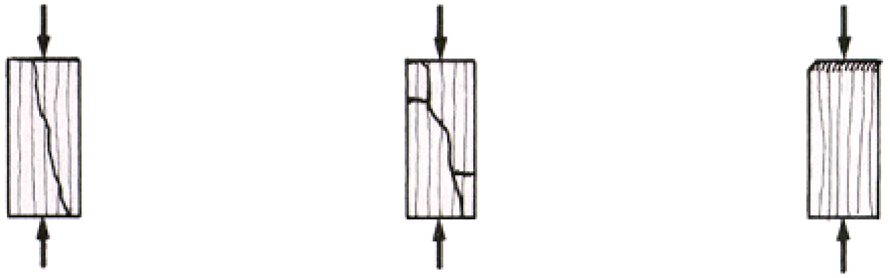

(d) Splitting (e) Combined crushing and parallel-to-grain shearing (f) End-rolling or brooming

Reproduced from ASTM (2021a)

Figure 2.8: Compressive failure modes of wood under parallel-to-grain compression

Past research and design standards modelling the compressive wood behaviour most frequently reference Bazan's (1980) bilinear falling-branch model, Figure 2.7d (*e.g.*, in Lacroix & Doudak (2018a) and Plevris & Triantafillou (1992)). In testing small rectangular samples of clear wood under uniaxial compression, Song et al. (2007) observed patterns between failure mode and stress-strain relationship: the authors noted that parallel-to-grain splitting (Figure 2.8d), which occurred most frequently, agreed well with Bazan's (1980) model; whereas the rarer failure modes of crushing (Figure 2.8a) and shearing (Figure 2.8c) agreed better with earlier models by Malhotra & Mazur (1970) and Glos (1978), respectively. André et al. (2014), using small cylindrical samples of clear wood, found a resemblance to Malhotra & Mazur's and Glos' models only. Although it is convenient to test smaller specimens, Barrett & Lau (1994) note that size has a significant effect on wood strength and behaviour, observing that small clear-wood samples bear limited representation to full-scale members which contain assorted defects and exhibit higher variability.

2.2.3.3 Flexure

In flexure, the longitudinal grain of wooden beams is typically parallel to the span, thereby engaging both tension and compression parallel-to-grain. It is, therefore, necessary to consider the constitutive relationship between tension and compression to accurately predict the flexural response of wooden beams. Figure 2.9a depicts the stress-strain curves employed by Buchanan (1990). Here, tensile strength is linear and brittle, peaking at a failure stress f_t which is dependent on the member size. The compressive strength is modelled to be bilinear, reaching a maximum stress f_c at its yield point ε_y before descending linearly into failure due to wood fibres crushing or buckling. Figure 2.9b shows the resulting strain and stress distributions through a planar rectangular cross-section. The falling branch portion in the compressive stress-strain relationship reflects that the extreme fibre bears not the maximum strength, but a reduced one whereupon residual compressive capacity takes over when yield strain is surpassed. It should be noted that the compressive capacity perpendicular-to-grain should be checked at locations of bearing; and that the tensile capacity perpendicular-to-grain should be checked at locations where there are hanging loads, splits, or notches.

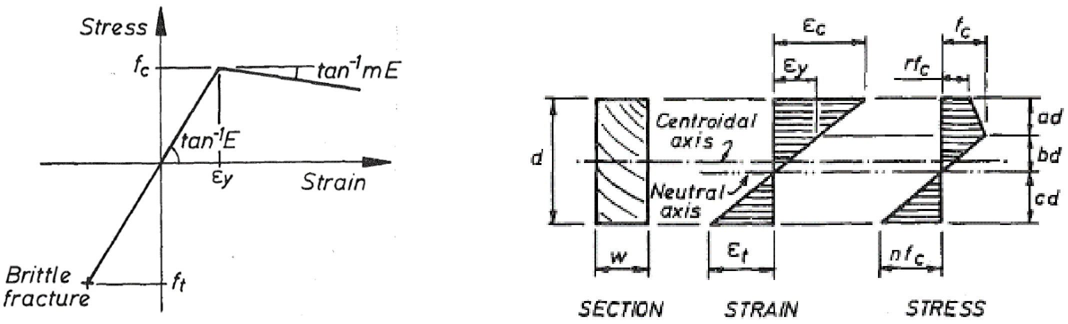

(a) Axial loading

(b) Flexural loading

Reproduced from Buchanan (1990)

Figure 2.9: Strength models of wood

Bending capacity in clear wood members is typically governed by tension failure, characterized by ruptured wood fibres originating at the extreme or outermost tension fibre, as shown in Figure 2.10a–d, and occurring in or near the region of maximum bending moment. When tensile failure is gradual, the tension fibres split into numerous splinters (Figure 2.10c). In contrast, when tensile failure is brash or abrupt, splintering does not occur (Figure 2.10d) (ASTM, 2021a). Compressive failure in flexure is frequently characterized by crumpling or wrinkling fibres (Figure 2.10e). The presence of defects may trigger other failure modes. Knots, in particular, result in points of high-stress concentrations from which cracks may develop and propagate (Figure 2.10b). Splits or checks may provide a pathway leading to a longitudinal shear failure (Figure 2.10f).

(a) Simple tension, side face

(b) Cross-grain tension, side face

(c) Splintering tension, tension face

(d) Brash tension, tension face

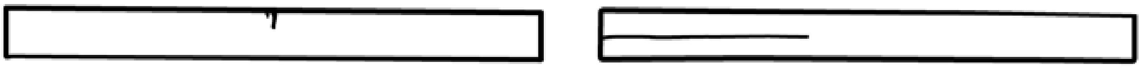

(e) Compression, side face

(f) Horizontal shear, side face

Reproduced from ASTM (2021a)

Figure 2.10: Failure modes of wood under static bending

Given that failures in wood members generally originate from defects, a common strategy for retrofitting and strengthening is to bridge such defects through the use of another medium to transfer stress over these points of weakness (Davids et al., 2008; Fox, 1978; Lacroix & Doudak, 2020; Lee & Kim, 2000; Moody et al., 1983; Plevris & Triantafillou, 1992, 1995; Raftery & Harte, 2013; Xiong, 1991; Yang et al., 2016). Methods developed in this vein are described in detail in Section 2.4.

2.3 FRP Composites as a Reinforcement Material

2.3.1 Overview

Fibre-reinforced polymer (FRP) composites are composed of continuous fibres embedded into a polymeric matrix. The high-strength fibres contribute to the bulk of the composite material’s strength. The polymer matrix, though comparatively weak, serves primarily as a binding agent which transfers stresses through the fibres and provides some limited ductility to the brittle fibres (Callister Jr. & Rethwisch, 2003). The combination of the two materials results in a very strong and stiff composite, as shown in Figure 2.11, that is also generally lightweight, workable, non-corrosive, and chemically stable. All these properties together make FRPs particularly well suited for numerous applications including aerospace engineering, automotive, watercraft, sporting equipment, and biomedicine (Egbo, 2021). In the construction industry, FRPs have gained increasing popularity as a strengthening and rehabilitation material in part due to their extremely high strength-to-weight ratio, especially when compared to steel (Callister Jr. & Rethwisch, 2003). This property allows greater strength to be achieved in much smaller cross-sections or to increase load capacity in new or existing structures with minimal increase to cross-sectional dimensions.

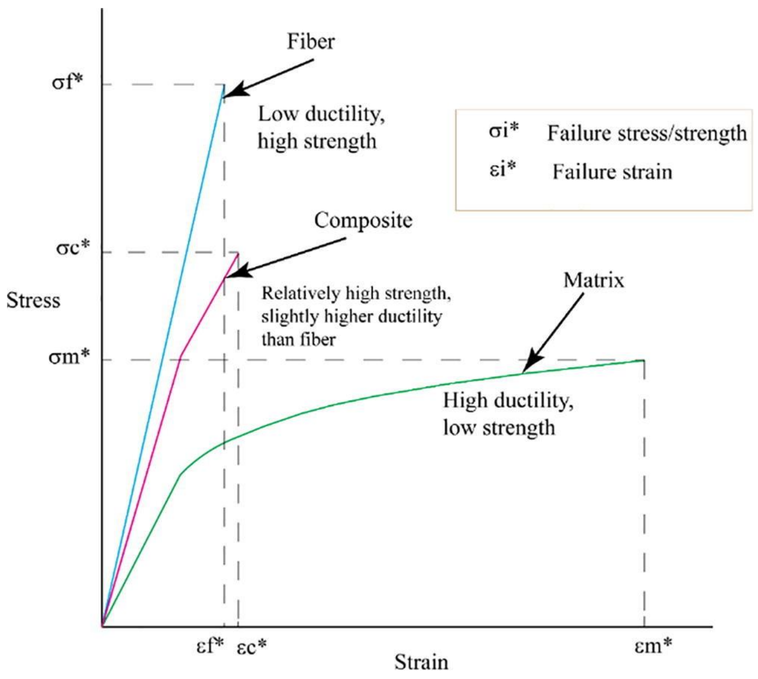

Reproduced from Egbo (2021)

Figure 2.11: Stress-strain behaviour of an FRP composite relative to its constituents

One major advantage of FRP is its extreme variability in form (Hollaway, 2010). Fibres are available in woven fabric sheets, which can be cut and applied in flexible configurations customized to the desired application (Legg & Tingley, 2020; Vetter, 2022). When using this method, one or more layers of these sheets are saturated with a liquid resin and then applied to the surface of the structural element. The fabric is bonded into place as the resin cures, forming a solid polymer matrix. Alternatively, FRP elements can be manufactured into a wide variety of shapes not limited to plates, rebar, shells, and a multitude of structural cross-sections. These elements can be bonded to a structural element by chemical adhesives or mechanical fasteners to suit the application. Stress transfer between FRP and wood elements is achieved most effectively by using adhesive bonding of the polymer matrix. Whereas mechanical fasteners may be used to fully or partially transfer stresses, they can introduce undesired stress concentrations, thereby resulting in undesirable failure modes (Custódio et al., 2009).

2.3.2 Fibre materials

The fibres used to reinforce FRP may be derived from various sources to achieve different mechanical properties and structural behaviours. The most used filaments are made from glass, carbon, aramid, and less commonly, basalt and plant-based fibres. Filament materials tend to be very stiff and brittle; however, due to the small, nano-sized diameters of each fibre, the presence of failure-causing defects is very low, allowing very high strengths to be achieved (Callister Jr. & Rethwisch, 2003). Because the fibre component is the primary contributor to the strength and performance of the overall FRP composite (Figure 2.11), the selection of the fibre material has a significant impact on the final product as well as its affordability (Callister Jr. & Rethwisch, 2003). Figure 2.12 compares the strengths of different types of FRP—glass, aramid, and carbon—against that of mild steel.

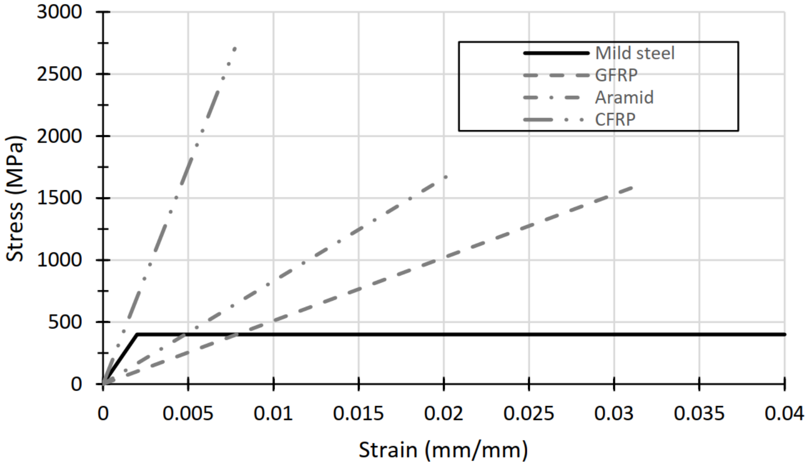

Reproduced from ACI (2008)

Figure 2.12: Average stress-strain curves for common FRP composites and mild steel

Glass-fibre-reinforced polymers (GFRPs) are the most widely used FRPs due to their low cost of production thus making them more commercially viable than other FRPs in most applications (O'Callaghan, 2021). Though glass fibres have high strength, low density, and are relatively chemically inert (Callister Jr. & Rethwisch, 2003), they tend to creep under sustained loading and are generally outperformed by other common FRP fibre materials (Balázs & Borosnyói, 2001). Glass filaments used in GFRP are made from readily available colemanite, limestone, kaolin, and sand. Depending on the ratios of each ingredient used, these filaments may be graded for particular uses based on the resulting strength, thermal or electrical conductivity, chemical resistance, and other properties (Fitzer et al., 2000).

Carbon-fibre-reinforced polymers (CFRPs), compared to other FRPs, exhibit higher tensile strength and stiffness, higher resistance to creep and fatigue, are less dense, have low thermal and electrical conductivity, exhibit low thermal expansion, but are susceptible to galvanic corrosion. Polyacrylonitrile is the most widely used form of carbon fibre in CFRP and is further classified by its modulus of elasticity and strength. High material cost is a primary deterrent to using CFRP; nonetheless, the superior performance of CFRP compared to other FRPs can make it a more cost-efficient option, particularly in specialized applications such as seismic column retrofits (Estrada & Lee, 2014).

Aramid-fibre-reinforced polymers (AFRPs), best known for their application in bulletproof armour, are highly resistant to impact damage. The term “aramid” is a portmanteau of “aromatic polyamide,” a thermoplastic polymer (McDaniel & Knight, 2014). These fibres are ductile, have a high strength-to-weight ratio, and are resistant to creep and fatigue; however, structural applications of AFRP are limited by its extreme sensitivity to environmental conditions (McDaniel & Knight, 2014).

2.3.3 Fibre orientation

The size, length, continuity, uniformity, density, and alignment of the fibres play a distinct role in the composite material properties and vary with the FRP production process. Fibre lengths can be generally classified as continuous or chopped, and their orientations as aligned or random; examples are shown in Figure 2.13. Chopped or short, randomly oriented fibres are cheaper to produce and are well suited for adding strength to complex, irregular shapes. Long, continuous fibres allow maximum tensile strength to be developed in their longitudinal direction but bear very little strength in their transverse direction (Fu & Lauke, 1996).

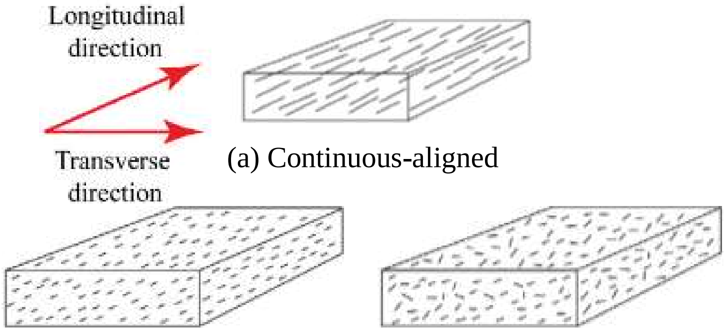

(a) Continuous-aligned

(b) Discontinuous-aligned (c) Discontinuous-random

Reproduced from Egbo (2021)

Figure 2.13: Fibre length and orientation

Continuous fibres are commercially available in the form of yarns or fabrics. If strengthening is only required in one known direction (*e.g.*, reinforcing a structural beam against tensile failure), continuous, unidirectional FRP achieves this purpose with the greatest efficiency. Biaxial fabrics split the direction of the fibres into a principal, longitudinal direction (“warp” fibres) and a secondary, usually perpendicular direction (“fill” or “weft” fibres). In addition to biaxial 0°-90° weaves, biaxial ±45° fabrics are also available, as well as various triaxial and quadraxial fabrics. Such multiaxial weaves allow for strengthening in multiple directions, albeit at the cost of having fewer fibres to reinforce each direction and at the risk of developing a non-linear behavioural response (O’Callaghan, 2021). Fabrics can alternatively be layered to provide further reinforcement in one or multiple directions (Vetter, 2022).

2.3.4 Polymeric matrices

Four primary functions of the polymer matrix are (1) to bind the fibres together, (2) to transfer stresses along and across the fibres, (3) to reduce the propagation of brittle cracks, and (4) to protect the fibres from physical abrasion and chemical exposure (Callister Jr. & Rethwisch, 2003). The polymer component, which accounts for 30% to 80% of the FRP composite by weight, has comparatively little strength (Figure 2.11), but it contributes reasonable ductility, durability, dimensional stability, and chemical stability (Hollaway, 2010). When set, the matrix provides lateral support against buckling fibres; and whether the fibres are broken or continuously intact, transfers shear stresses through the composite material.

Matrix polymers can be classified according to their thermal response into the categories of thermoplastics and thermosets. Thermoplastics (*e.g.*, polyethylene, polystyrene, polypropylene) are characterized by the ability to soften or melt in response to heating, and reversal upon re-cooling. Molecularly, this phenomenon is attributed to a linear or branched polymer chain structure. Thermoplastics are highly recyclable due to their ability to be reshaped, making them a popular choice for consumer plastics; however, they tend to be relatively soft and weak, have low durability, exhibit high creep, and are thermally unstable, therefore providing limited applications in structural engineering. Due to their high viscosity, thermoplastics are difficult to embed with continuous fibres but may be used with short fibres in injection-moulded forms (Mallick, 2007).

Thermosetting polymers (*e.g.*, polyester, polyurethane, epoxy) are produced in the form of a liquid resin which hardens in a curing process. In this exothermic process, the molecular polymer chains undergo extensive cross-linking in an irreversible chemical reaction often aided by a catalyst or curing agent; once cured, thermosets do not soften or melt upon heating, though extreme temperatures may cause them to permanently degrade (Callister Jr. & Rethwisch, 2003). As a result of the cross-linked structure, thermosets are generally stronger, harder, more chemically and thermally stable, experience less fatigue, and are therefore preferred plastics for structural applications; however, these properties make recycling difficult to achieve and disposal an environmental concern (Callister Jr. & Rethwisch, 2003). Stronger molecular bonds also result in the generally preferred use of thermosets over thermoplastic as an FRP matrix (Yan et al., 2012) or adhesives to combine dissimilar materials, including, specifically, wood and FRP (Custódio et al., 2009). Used as an FRP matrix, a liquid starting phase at ambient temperatures offers workability: fibres freshly saturated in resin allow for flexible application into infinite configurations. The polymer matrix used in this study is a two-part epoxy resin.

Compared to other thermosetting resins—specifically, polyesters, vinyl esters, and polyurethanes—epoxies are the most expensive by volume and require thorough mixing of carefully measured reagent components to achieve the best results (McDaniel & Knight, 2014).

Overall, polymers perform poorly at elevated temperatures. The polymer matrices used in FRP have low glass-transition temperatures which range from 60°C to 130°C. Exceeding these temperatures, the polymer undergoes a phase change from hard and brittle to viscous and rubbery, thereby severely compromising the rigidity and strength of the FRP composite. Further, in terms of fire performance, polymer matrices are highly combustible, spreading rapidly and generating toxic smoke when ignited (Zigler & Pokorný, 2015).

2.4 Behaviour of FRP-reinforced Wood Composites

2.4.1 Overview

Past efforts to reinforce wood and wood products have involved diverse configurations of reinforcement and applications. Applications of bonded metal plates (Hoyle Jr., 1975; Mark, 1961), metal bars (Bulleit et al., 1989), and pre- or post-stressed cables (Al-Hayek & Svecova, 2014; De Luca & Marano, 2012) have seen limited degrees of commercial success for flexural reinforcement.

Technological advancements, improvements to manufacturing capabilities, and rising demand have made FRPs an economically viable and increasingly popular material, including in the construction industry. The use of FRP as a strengthening material for structural members has been studied extensively for concrete specimens subject to different types of loading—including compression (*e.g.*, Demers & Neale (1999), Hadi (2005), Micelli et al. (2001), Sulaiman et al. (2016), Y. Zhang et al. (2020), and Zhou et al. (2019)), flexure (*e.g.*, J. A. Martin & Lamanna (2008), Nanni & Norris (1995), Tomlinson & Fam (2015), Triantafillou & Antonopoulos (2000), Yost et al. (2001), and S. S. Zhang et al. (2017)), seismic (*e.g.*, Iacobucci et al. (2003) and Memon & Sheikh (2005)), and blast (*e.g.*, Buchan & Chen (2007) and Jacques et al. (2015))—in various structural geometries, reinforcement configurations, and environmental conditions. Much of the research on FRP-reinforced wood has drawn from precedents with concrete but has since become its own established field of study.

In the context of fire, FRPs fail quickly when exposed to elevated temperatures. As such, externally bonded FRPs provide no fire protection and should not be relied upon. Fire-retardant chemical coatings, particularly those that employ an intumescent or foaming mechanism of protection, are not a suitable strategy with FRP because the glass-transition temperature is lower than that required to activate the desired foaming reaction (Ji et al., 2013). Physical isolation (*e.g.*, encasing, embedment, or near-surface mounting) is the best option for reinforcing wood members with FRP when fire performance is a priority, with the additional benefit of improved aesthetics (Z. A. Martin & Tingley, 2000). Some examples of achieving FRP isolation are shown in Figure 2.14. BS 5268-4 (2007) specifies 20 mm of wood cover to provide 30 minutes of fire resistance. A parametric study by Zigler & Pokorný (2015) found that near-surface mounting of FRP under an insulating wood cover of 25 mm can provide 15 minutes of fire resistance, and a cover of 40 mm can achieve 30 minutes of fire resistance.

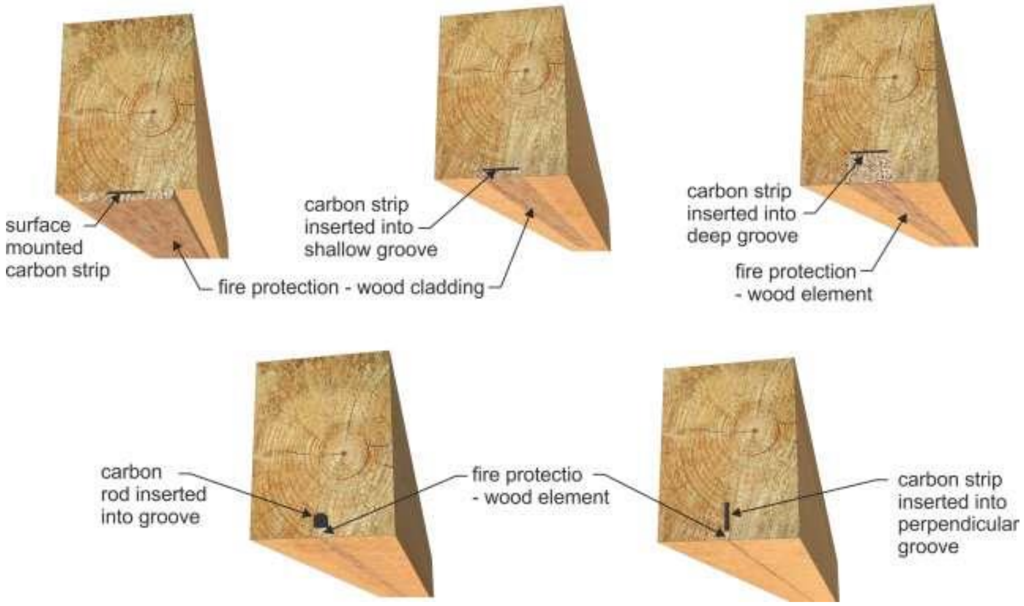

Reproduced from Zigler & Pokorný (2015)

Figure 2.14: Examples of fire protection for FRP elements

2.4.2 FRP-reinforced wood for compression resistance

FRP confinement is a popular form of reinforcement for wood columns, bridge piles, and abutments. Such methods are quick and simple to install, cost-effective, and can be done in situ and without closing or reducing service levels (Legg & Tingley, 2020).

Chidiaq (2003), Najm et al. (2007), and Song et al. (2010) investigated the behaviour of small cylindrical specimens of clear wood and drew common conclusions on the effectiveness of full-length FRP confinement on increasing peak strength, ductility, and durability. In heavy timber piles, Kim & Andrawes (2016) observed that continuous GFRP wraps provided significant improvement to peak strength and ductility. Emerson (2004) and Caiza et al. (2012) showed that this same reinforcement method can also be effective in restoring compressive and flexural strength in damaged timber piles in situ. As an alternative to continuous confinement over the full length, Dong et al. (2015) reported that partial confinement can also be quite effective for increasing the load-carrying capacity of square columns wrapped with bands of CFRP, AFRP, or basalt FRP (BFRP). Heiduschke & Haller (2010) and

O’Callaghan et al. (2021) observed that even small amounts of FRP confinement can increase the peak capacity to the extent of changing failure modes; Heiduschke & Haller (2010) investigated GFRP and CFRP wraps on hollow timber columns and observing their failure modes transition from sudden splitting towards ductile crushing and local buckling, while O’Callaghan et al. (2021) tested square lumber confined with varying configurations of continuous FRP confinement to determine the effect of fibre orientation on compressive resistance. Figure 2.15 shows representative failure modes from O’Callaghan (2021) where it can be noted that, whereas damage propagated throughout the unreinforced control specimens, the GFRP reinforcement caused wood fibres to “wrinkle” with localized damage.


(a) No confinement (b) Uniaxial FRP (c) Bidirectional FRP (d) Bidirectional FRP

Reproduced from O’Callaghan (2021)

Figure 2.15: Effect of GFRP confinement on square lumber columns

FRP confinement also does not need to be longitudinally continuous to successfully strengthen columns, as demonstrated by Zhang et al. (2012), who used FRP bands to reinforce longitudinally cracked full-scale square columns and observed an effective restoration of the load-carrying capacity to pre-cracked levels.

Studies by Song et al. (2010), Dong et al. (2015), and Kim & Andrawes (2016) showed that the degree of compressive strengthening by circumferential confinement is not directly proportional to the volume ratio of FRP applied. Conversely, André et al. (2013) found a linear relationship between reinforcement ratio with strength and stiffness to small clear wood blocks and dog-bone shapes when the direction of CFRP wrap is applied longitudinally or parallel-to-grain rather than transversally or perpendicular-to-grain.

2.4.3 FRP-reinforced wood for flexural resistance

The body of literature dedicated to reinforcing wood members puts much of its emphasis on members in flexure. Common applications for FRP-wood composites include the rehabilitation of timber bridges, which benefit greatly from the ease and speed of in-situ application, an economical alternative to demolition and replacement (Buell & Saadatmanesh, 2005; CSA, 2019a; Gentile et al., 2002; Hay et al., 2006).

Simple flexural reinforcement of the tension face with thin strips or plates of FRP has been shown to increase the ultimate flexural capacity by up to 50%, stiffness by up to 20%, as well as reduce overall variability due to the bridging of failure-inducing defects (Gentile et al., 2002; Johns & Lacroix, 2000). However, it should be noted that these results can be influenced greatly by the properties and quantity of the FRP used. Plevris & Triantafillou (1992) found that reinforcement ratios of just 1% by cross-sectional area resulted in substantial improvements to stiffness and flexural load capacity, resulting in increased compressive yielding behaviour; at higher reinforcement ratios, the stress transition was enough to even change the mode of failure, albeit with diminishing returns; and that reinforcement ratios beyond 3% provided limited benefit as the incremental gains to flexural capacity became negligible. The authors concluded that the critical FRP reinforcement ratio depended on only three parameters: the strain ratio at failure between wood in tension and wood in compression; the strain ratio between FRP tension at failure and wood compression at yielding; and the stiffness ratio between the FRP and wood. Lindyberg & Dagher (2012) observed that 3% reinforcement ratios of this same configuration could increase the bending capacity of glulam beams by over 100%. Raftery & Harte (2013) noted that when glulam beams under positive bending were reinforced with FRP plates on the tension face, wood lamination on the compressive side (*i.e.*, top of the beam) may yield or wrinkle, thereby introducing some increase in ductility. However, a common issue with simple tension reinforcement in flexure, as reported by Dorey & Cheng (1996a, 1996b), Hernandez et al. (1997), and Lacroix & Doudak (2018a), is the sudden debonding of the FRP following failure in the wood tension surface. Furthermore, while the external FRP bonding method is popular for its ease of application, such configurations are more susceptible to environmental damage (Raftery & Harte, 2013). Examples of FRP configurations for flexural reinforcement are shown in Figure 2.16 (Zigler & Pokorný, 2015).

(a) Surface-mounted reinforcing strip (b) CFRP strip inserted vertically into groove (c) CFRP rod inserted into groove

Reproduced from Zigler & Pokorný (2015)

Figure 2.16: Examples of external FRP reinforcement for flexure

When reinforcement is extended beyond only the tension face, the reinforcement ratio requirements described above by Plevris & Triantafillou (1992) become ambiguous and the body of research is comparatively smaller. FRP configurations for shear reinforcement involve full or partial confinement around the beam. Partial confinement, in this context, is generally applied when all transverse sides of the member are not easily accessible, such as in the case of slab supports and wall abutments. Unidirectional and/or bidirectional FRP fabrics are typically used in such contexts. Figure 2.17 presents basic cross-sectional arrangements for shear reinforcement using FRP.

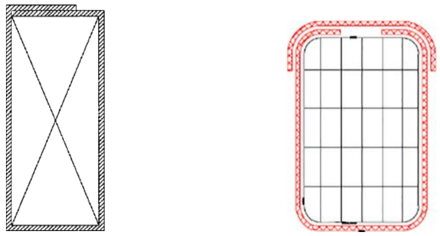

(a) Full confinement, continuous[1] (b) Full confinement, spliced[2]

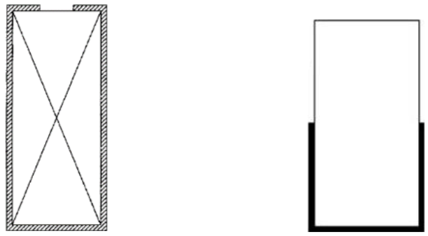

(c) Partial confinement, full depth[1] (d) Partial confinement, partial depth[3]

Reproduced from 1. Buell & Saadatmanesh (2005), 2. Lacroix & Doudak (2020), and 3. de la Rosa García et al. (2013)

Figure 2.17: Basic shear reinforcement schemes for FRP-reinforced beams

Buell & Saadatmanesh (2005) retrofitted existing bridge stringers and investigated the effect of wrapping the timber members using 0°/90° bidirectional CFRP. The authors tested the full-depth confinement configurations shown in Figure 2.17a and Figure 2.17c as well as timber beams with no or simple (tension-only) reinforcement. The bidirectional confinement was found to have reduced the detrimental effects of the defects, and the FRP reinforcements contributed significant improvements in the overall peak strength, stiffness, and deflection relative to the unretrofitted beams. Lacroix & Doudak (2020) studied the effects of layering different reinforcement schemes (Figure 2.17a-d) on the same member with varying combinations of tension reinforcement and degrees of longitudinal continuity (*e.g.*, continuous half-depth partial confinement with continuous or targeted, full or partial confinement). Confinement was shown to limit crack development and delay wood-FRP debonding beyond peak resistance, with full-length confinement contributing the most to ductility and post-peak resistance. Vetter (2022) applied combinations of GFRP in full (Figure 2.17a) and partial (Figure 2.17d) confinement to glulam beams, and also compared the effects of confinement run continuously through the length with confinement added only to high-shear zones as "stirrups." Although the ultimate resistance was increased in all reinforced members, those reinforced with only simple tension laminates and partial half-depth confinement primarily failed in shear. However, when stirrups of full or gradated confinement were added, shear failure was partially contained and prevented premature debonding (Vetter, 2022).

An alternative to reinforcing bending members with FRP fabric is using FRP rebar. FRP bars are often available with grooves or with a sand coating to develop adequate bonding shear. Gentile et al. (2002) studied the effect of near-surface-mounted GFRP bars on timber beams. Similar to fabric reinforcement, the bars bridged local defects, arrested crack opening, confined local rupture, and were able to transition the failure mechanism from brittle tensile failure to ductile compressive failure. Although debonding and delamination were common issues with tensile FRP fabric laminates on wood, the FRP bars did not demonstrate this failure mechanism (Gentile et al., 2002). The authors reported that bar reinforcements increased the numerical ultimate tensile strain failure in the extreme wood fibre by 64% over that of unreinforced beams. This strength enhancement was accounted for as a constant modification factor, α_m, which Yang et al. (2016) later incorporated into a model to predict the flexural strength of FRP and steel-reinforced glulam beams. Lacroix & Doudak (2018a, 2020) determined the modification experimentally by measuring strain increases through the use of strain gauges and reported increases of 1.17 and 1.2., respectively. Figure 2.18 compares typical load-deflection curves for simple tension FRP laminates and GFRP bars.

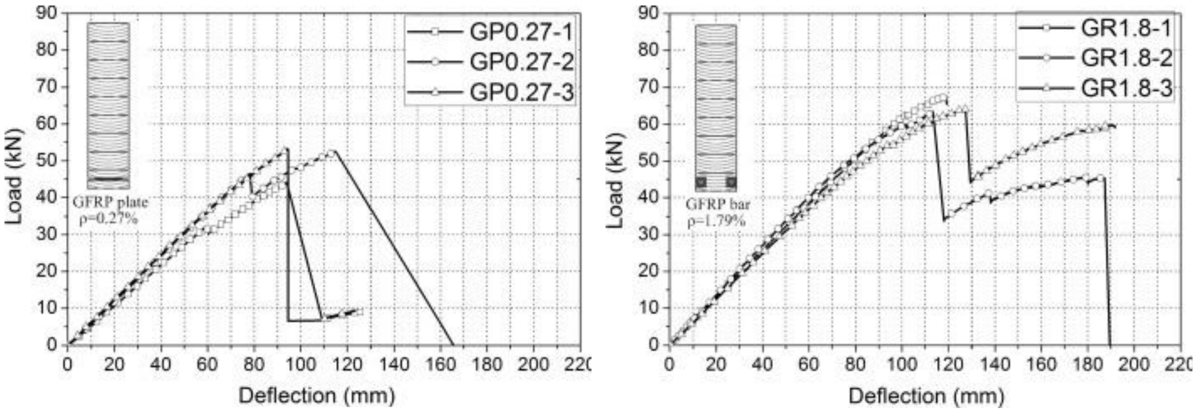

(a) FRP laminates

(b) FRP bars

Reproduced from Yang et al. (2016)

Figure 2.18: Typical load-deflection curves for retrofitted glulam beams

2.5 Predicting Flexural Resistance in FRP-reinforced Timber Beams

2.5.1 General

Methods for predicting the flexural resistance in FRP-reinforced timber beams often borrow principles from those established for other composite materials, particularly those of reinforced concrete beams. Such approaches to determine the flexural resistance depend on the constitutive relationships employed. As summarized in Section 2.2.3 and Section 2.3.2, the tensile strength models for wood parallel-to-grain and FRPs are generally linear and brittle; however, compressive strength models for wood parallel-to-grain are more nuanced and can be subject to greater scrutiny (Figure 2.7).

The transformed-area or transformed-section method is a popular technique for the analysis of composite sections. The basis for this method is to “transform” the cross-sectional areas of each material by a modular factor such that their geo-mechanical properties may be considered equivalent. Limitations to this method include that all material behaviour is assumed to be linear-elastic only and that no distinction is made between tensile and compressive behaviours (Beer et al., 2012).

The force-equilibrium method studies the distribution of internal forces at the midspan cross-section of a beam subject to bending loads. It builds upon the transformed-area method by considering that the material behaviour may not necessarily be entirely elastic. D’Ambrisi et al. (2014) approached this by taking compressive wood behaviour to be elastoplastic (Figure 2.7a). The moment-curvature method, as applied by Lacroix & Doudak (2018a), further builds upon this technique by adopting a bilinear compression model (Figure 2.7d).

Each of these flexural analysis methods assumes that stresses are perfectly transferred between materials (*i.e.*, bonds remain intact) and plane sections remain plane during bending. Variations between the model and the actual beam geometry, as well as variations within the material itself (e.g., distribution of knots in wood or bubbles in resin) also affect the accuracy of the predicted results.

2.5.2 Transformed-area method

For a simply-supported beam subjected to symmetrical four-point loading with each point load being of equal magnitude, the relationship between applied load and moment can be described as

$$M = \frac{PL}{6} \tag{2.1}$$

where M is the corresponding moment to P, P is the total applied load, and L is the span length of the beam. Assuming that failure is governed by tensile wood failure, the maximum load resistance, P_r, can be obtained for this load configuration by equating Equation 2.1 and Equation 2.2,

$$M_r = MOR \cdot \frac{I'}{\bar{y}'} \tag{2.2}$$

where M_r, is the maximum moment resistance of the cross-section, MOR is the modulus of rupture or flexural strength of the unreinforced wood, I' is the area moment of inertia of the transformed section, $\bar{y}'$ is the neutral axis of the transformed section measured from the bottom of the beam, given by Equation 2.3 and Equation 2.4, respectively:

$$I' = \sum\left(I_i' + A_i' d_i^2\right) \tag{2.3}$$

$$\bar{y}' = \frac{\sum A_i' y_i}{\sum A_i'} \tag{2.4}$$

where I_i' is the area moment of inertia of each transformed material component about its centroid, A_i' is the transformed area of each material component, d_i is the vertical distance from the centroid of each component to the neutral axis, and y_i is the centroid of each untransformed material component measured from the bottom of the beam.

The eponymous area transformation is achieved by factoring the cross-section areas of each material component by a factor equal to the ratio of their moduli of elasticity, as schematized in Figure 2.19, where A_w is the cross-sectional area of the wood portion; A_r and A_r' are the untransformed and transformed areas of the reinforcement; E_w is the modulus of elasticity of the wood; and n is the modular ratio.

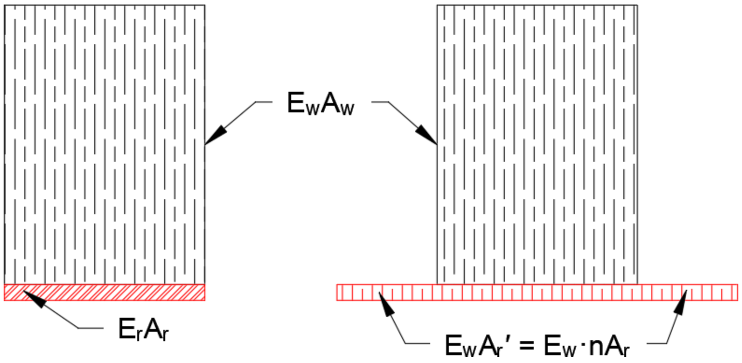

(a) Laminate reinforcement

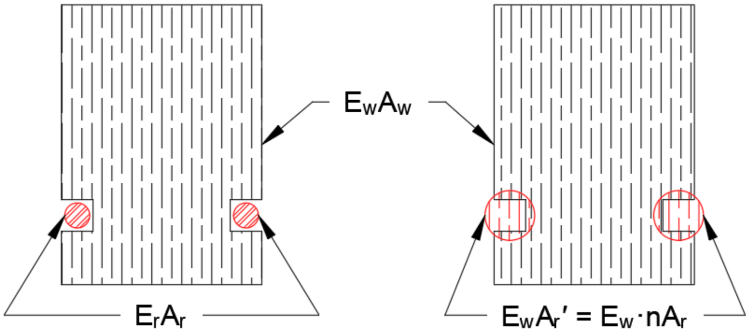

(b) Bar reinforcement

Figure 2.19: Area transformation of composite cross-sections

The elastic modulus of the epoxy resin used to bind FRP to wood is very small relative to the other materials and is thus neglected. The transformation can be executed using Equation 2.5 and Equation 2.6:

$$n = \frac{E_{FRP}}{E_{wood}} \tag{2.5}$$

$$A_f' = nA_f = nbh = (b')h \tag{2.6a}$$

$$A_b' = nA_b = n\pi r^2 = \pi(r')^2 \tag{2.6b}$$

where n is the modular ratio, E_{FRP} is the tensile elastic modulus of the GFRP fabric or bars, E_{wood} is the tensile elastic modulus of the sawn timber or glulam; A_f' and A_f are the transformed and actual areas of the fabric FRP portions, respectively; b and b' are the actual and transformed widths of the FRP fabric, respectively; h is the actual thickness of the FRP fabric; A_b' and A_b are the transformed and actual areas of the bar FRP portions, respectively; and r and r' are the actual and transformed radii of an FRP bar, respectively. The area moments of inertia are likewise transformed, based on their respective geometries, using Equation 2.7:

$$I_f' = \frac{(b')h^3}{12} = \frac{h^3}{12}(nb) \tag{2.7a}$$

$$I_b' = \frac{\pi (r')^4}{12} = \frac{\pi}{12}\left(\sqrt{n}\, r\right)^4 \tag{2.7b}$$

where I_f' and I_b' are the transformed area moments of inertia of an FRP fabric laminate and bar, respectively.

2.5.3 Force-equilibrium method

D'Ambrisi et al. (2014) presented the following approach for obtaining the bending resistance of an FRP-reinforced timber beam. Special attention is given to the compressive wood strain, ε_c, and whether it exceeds its elastic limit or compressive yield strain, ε_0, based on an elastoplastic model as described by Neely (1898) in Figure 2.7a, the result of which is reflected in Figure 2.20.

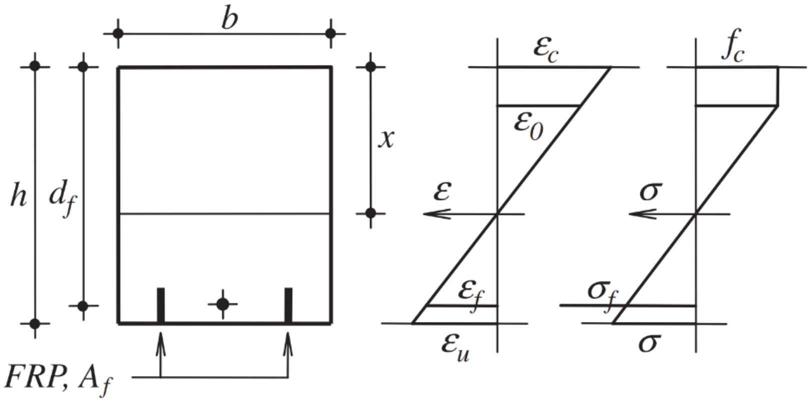

(a) Section (b) Strain (c) Stress

Reproduced from D'Ambrisi et al. (2014)

Figure 2.20: Force-equilibrium analysis using an elastoplastic wood model

When compressive wood strain does not exceed its elastic limit (*i.e.*, $\varepsilon_c \le \varepsilon_0$), the procedure may be presented as Equation 2.8 and Equation 2.9:

$$M_R = E\varepsilon_u \frac{I}{h-x} \tag{2.8}$$

$$x = \frac{1}{bh+nA_f}\left(\frac{bh^2}{2} + nA_f d_f\right) \tag{2.9}$$

where M_R is the maximum moment resistance about its neutral axis; E is the elastic tensile modulus of the wood; ε_u is the ultimate or failure tensile strain of the wood; I is the area moment of inertia described in Equation 2.3 and Equation 2.7 for small amounts of reinforcement relative to wood; h is the height of the beam; x is the neutral axis of the transformed section measured from the top of the beam; b is the width of the beam; n is the modular ratio described in Equation 2.5; A_f is the total area of the FRP reinforcement; and d_f is the vertical distance of the centroid of A_f measured from the top of the beam.

Conversely, if the compressive wood strain does exceed its elastic limit (*i.e.*, $\varepsilon_c > \varepsilon_0$), the maximum moment resistance is instead determined by the product sum of the stresses shown in Figure 2.20 and their corresponding moment arm distances to the centroidal axis, multiplied by the section width using Equation 2.10:

$$M_R = bE\left[\frac{\varepsilon_0 x^2}{2} + \frac{(h-x)^2}{6}\left(2\varepsilon_u - \frac{\varepsilon_0^3}{\varepsilon_u^2}\right) + \varepsilon_u \frac{nA_f}{b}(d_f - x)\right] \tag{2.10}$$

where the neutral axis is obtained by equating the compressive and tensile forces—which may be derived from the stress distribution shown in Figure 2.20b—and solving Equation 2.11 accordingly:

$$\varepsilon_0\left[x + \frac{(h-x)}{2}\frac{\varepsilon_0}{\varepsilon_u}\right] = \varepsilon_u\left[\frac{(h-x)}{2} + \frac{nA_f}{b(h-x)}(d_f - x)\right] \tag{2.11}$$

2.5.4 Moment-curvature method

Lacroix & Doudak (2018a) applied a moment-curvature approach to obtaining the bending resistance of an FRP-reinforced timber beam. This method improves upon the previously described approach by D'Ambrisi et al. (2014) by applying the bilinear compression model described by Glos (1978), Bazan (1980), and Buchanan (1984, 1990) as illustrated in Figure 2.7d. The result of this application is reflected in Figure 2.21 for a semi-confined FRP application (*i.e.*, U-shaped reinforcement over the tension half of the beam).

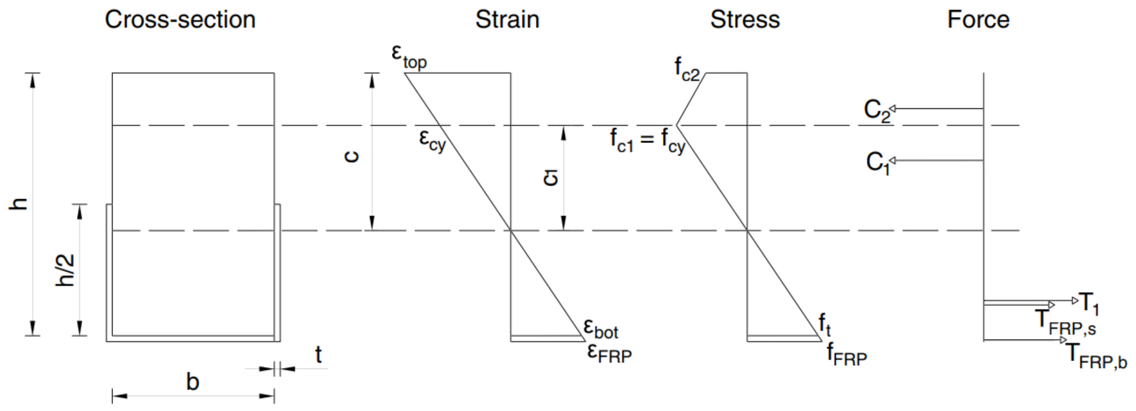

Reproduced from Lacroix & Doudak (2018a)

Figure 2.21: Force-equilibrium analysis using a moment-curvature model

Modifying this model for simple tension FRP reinforcement (*i.e.*, neglecting the FRP reinforcement on the sides of the beam) and when compressive wood strain does not exceed its yield strain (*i.e.*, $\varepsilon_{top} \leq \varepsilon_{cy}$), the bending moment at the neutral axis may be obtained using Equation 2.12 through Equation 2.15:

$$C_1 = \frac{1}{2} E_{Wc} \varepsilon_{top} cb \tag{2.12}$$

$$T_1 = \frac{1}{2} E_{wt} \varepsilon_{bot} (h - c) b \tag{2.13}$$

$$T_{FRP,b} = \frac{1}{2} E_{FRP} (\varepsilon_{bot} + \varepsilon_{FRP}) t_{FRP} b \tag{2.14}$$

$$M_R = C_1 \left(\frac{2c}{3}\right) + T_1 \left[\frac{2(h-c)}{3}\right] + T_{FRP,b} \left(h - c + \frac{t_{FRP}}{2}\right) \tag{2.15}$$

where C_1 and T_1 are the unyielded-compressive and tensile forces acting over the wood section, respectively; E_{Wc} and E_{Wt} are the moduli of elasticity of wood in compression and tension, respectively; ε_{top} and ε_{bot} are the wood strains at the top and bottom, respectively, of the beam; c is the position of the neutral axis measured from the top of the beam; b and h are the width and depth of the beam, respectively; $T_{FRP,b}$ is the tensile force acting over the bottom-laminate FRP; ε_{FRP} is the strain at the outermost layer of the FRP; t_{FRP} is the thickness of the FRP layer; and M_R is the bending moment at the neutral axis.

If compressive yield strain is exceeded before tensile failure (*i.e.*, $\varepsilon_{top} > \varepsilon_{cy}$), then the resultant compression forces must be adjusted to reflect the reduced post-yield capacity. The linear rate of decline is described by Equation 2.16:

$$-mE_{Wc} = \frac{f_{c2} - f_{cy}}{\varepsilon_{top} - \varepsilon_{cy}} \tag{2.16}$$

where m is a unitless term representing the declining slope of post-yield strength as a factor of E_{Wc}; $f_{cy} = f_{c1}$ and f_{c2} are the compressive stresses at yielding and at the top of the beam, respectively; and ε_{cy} and ε_{cy} are the compressive wood strains corresponding to f_{cy} and f_{c2}. The bending moment at the neutral axis for the yielded beam can be thus found using Equation 2.13 and Equation 2.14 along with Equation 2.17 through Equation 2.19:

$$C_1 = \frac{1}{2} E_{Wc} \varepsilon_{cy} c_1 b \tag{2.17}$$

$$C_2 = \left(1 - \frac{\varepsilon_{cy}}{\varepsilon_{top}}\right)\left(\frac{1}{m} - \frac{\varepsilon_{top}}{2\varepsilon_{cy}} + \frac{1}{2}\right) m f_c cb = \frac{1}{2}(f_{cy} + f_{c2})(c - c_1) b \tag{2.18}$$

$$M_R = C_1 \left(\frac{2c_1}{3}\right) + C_2 \left[c_1 + \frac{(c - c_1)(2f_{c2} + f_{cy})}{3(f_{c2} + f_{cy})}\right] + T_1 \left[\frac{2(h-c)}{3}\right] + T_{FRP,b} \left(h - c + \frac{t_{FRP}}{2}\right) \tag{2.19}$$

2.5.5 Size effect adjustments

Defects in wood are often observed on its surface but may also be hidden within its interior. As such, larger wood members present a greater probability of containing failure-causing defects than smaller members. This is particularly true for elements which undergo brittle (tension) failures, although compressive strength is also affected by this so-called "size effect" phenomenon to a smaller degree (Buchanan, 1984). Consequently, strength data obtained from small-scale coupon tests may not be directly translated to full-scale members. To compensate, strength values can be adjusted by applying Equation 2.20:

$$f_c = f_{sc} \left(\frac{L_{sc}}{L_e}\right)^{1/k_1} \left(\frac{d_{sc}}{d}\right)^{1/k_2} \tag{2.20a}$$

$$f_t = f_{st} \left(\frac{L_{st}}{L_e}\right)^{1/k_1} \left(\frac{d_{st}}{d}\right)^{1/k_2} \tag{2.20b}$$

where f_c and f_t are the adjusted compressive and tensile yield strengths to be applied in the material model; f_{sc} and f_{st} are average compressive and tensile yield strengths obtained from testing the coupon samples; L_{sc} and L_{st} are the average lengths of the compression and tension coupons; L_e is the effective length in compression; d_{sc} and d_{st} are the average depths (*i.e.*, the smallest of the cross-section dimensions or the depth of a glulam layer fully integrated in the coupon) of the compression and tension coupons samples; d is the depth of the sawn timber beam or the average depth of the glulam layers; and k_1 and k_2 are the length and depth effect parameters, respectively (Gentile, 2000; Lacroix, 2017a; Madsen & Buchanan, 1986). For bending, in which wood elements are neither in pure compression nor tension, the strength of the extreme tension fibre may be obtained by applying Equation 2.21:

$$f_m = f_t \left[\frac{h-c}{h(1+k_3)}\right]^{-1/k_3} \tag{2.21}$$

where f_m is the extreme tension fibre stress; f_t is the adjusted tensile yield strength obtained from Equation 2.20b; h is the height of the cross-section; c is the depth of the neutral axis from the compression face; and k_3 is a parameter which accounts for the variation of strength through the height of the cross-section (Lacroix, 2017b).

The parameters k_1, k_2, and k_3 can be obtained from published literature such as Barrett & Lau (1994), or they may be approximated by Equation 2.22 as determined by Madsen & Buchanan (1986):

$$coefficient\ of\ variation = k^{-0.922} \tag{2.22}$$

Load configuration also influences beam strength. The length of the beam under its loading pattern at testing is adjusted such that the total stress it undergoes is equivalent to that of a uniform stress distribution. For a simply-supported beam subject to two symmetrical point loads, the L_e term in Equation 2.20 can thus be determined from Equation 2.23:

$$L_e = \frac{1+\frac{a_1 k_1}{L}}{k_1+1} L \tag{2.23}$$

where L_e is the effective stressed length; L is the span of the beam; a_1 is the distance between the symmetrically-placed loads; and k_1 is the length effect parameter (Gentile, 2000; Lacroix, 2017a; Madsen & Buchanan, 1986).

2.6 Summary

As wood structures gain renewed attention in the construction industry, the need for a more thorough understanding of strengthening and retrofitting schemes for wooden members using advanced materials and technologies is crucial to the development of design guidelines and the advancement of codes. FRP composites have been established to be a suitable reinforcement material to use in combination with wood primarily due to their ease of application and the behavioural enhancements they provide. The structural performance of wood primarily depends on the distribution of random defects, growth conditions, and species; however, the addition of FRP can bridge such failure-causing defects, drastically lessening their detrimental impact, allowing greater resistance to loading, and reducing variability in performance. The additional strength provided by FRP can often transition failure modes in wood from being governed by brittle tension into a more ductile—thus more desirable—failure by engaging compression-yielding. While the bending strength of FRP-reinforced wood beams can be predicted using numerical methods and simplified resistance models, further improving design guidelines requires additional research investigating the effect of reinforcement medium (e.g., bars vs. fabric) on different types of wood beams (*e.g.*, sawn timber vs. glulam) in addition to verifying the accuracy of different modelling approaches.

Chapter 3

Experimental Program

3.1 General

This chapter describes the experimental program investigating the flexural response of unreinforced and FRP-reinforced wood beams under static loading. The effects of reinforcement type, namely glass FRP (GFRP) bars and fabric, are investigated on both sawn timber and glulam specimens. The experimental program can be divided into three distinct phases of tests on the following:

1. Components (*i.e.,* wood, FRP coupons) subjected to uniaxial loading to determine the material properties for input in the analytical models,
2. Sawn timber and glulam beams reinforced with GFRP fabric laminates as simple reinforcement subjected to four-point bending,
3. Sawn timber and glulam beams reinforced with GFRP bars as tension reinforcement subjected to four-point bending.

A total of eleven full-scale beams were tested statically under four-point bending. Of these, five beams were sawn timber and six beams were glulam. In addition, to determine the individual material properties, eighteen wood samples were obtained from the respective batches for uniaxial component tests: six tension coupons for sawn timber, six tension coupons for glulam, and six compression coupons for glulam. Data for the sawn timber under uniaxial compression, GFRP laminates, and GFRP bars were obtained from O'Callaghan (2021), Vetter (2022), and Lochan (2021), respectively.

The following sections describe the materials and their origin, reinforcement configurations, and experimental test setups and loading protocols.

3.2 Materials

3.2.1 Overview

The purpose of the current experimental program is to investigate the effects of GFRP reinforcement in the form of bars and fabric laminates on the flexural response of sawn timber and glulam members. Wooden members of similar cross-sectional dimensions were selected to provide a relative comparison. It should be noted that the materials used in this study are from other studies, thus some of the experimental properties required for the analysis have already been established. The following sections present the origin and details of the wood used for the specimens as well as for the GFRP reinforcement.

3.2.2 Sawn timber

The sawn timber specimens used in this study consist of 140 mm × 140 mm × 2,438 mm (5½″ × 5½″ × 96″ or nominal 6×6×8) Spruce-Pine-Fir (SPF) Grade No. 2 or higher, which were leftovers from a study by O’Callaghan (2021). Five of these specimens were reserved for testing under four-point bending, whereas a sixth specimen was cut up for uniaxial parallel-to-grain tension tests per ASTM D143, “Standard Test Methods for Small Clear Specimens of Timber” (ASTM, 2021a). Uniaxial parallel-to-grain compression tests were not conducted for the sawn timber because the compressive properties for this same batch were already characterized by O’Callaghan (2021) and will be presented as required inputs to the analytical model.

For several months before testing, the wood specimens were conditioned in a humidity chamber (Figure 3.1a) to maintain a constant moisture content. Moisture content was measured using a Tramex MRH3 non-destructive digital wood moisture meter. The average surface moisture content of the sawn timber at the time of testing was 7.9% with a coefficient of variation (CV) of 0.11. The average density of the sawn timber at the time of testing was determined to be 405.4 kg/m^3 with a CV of 0.08. Despite storing the sawn timber specimens in the humidity chamber to avoid severe seasoning and checking, some specimens had cracks on two or three faces that were approximately 1 cm in width as shown in Figure 3.1b and Figure 3.1c. In addition to checking and splitting, some specimens had experienced some warping along the length as shown in Figure 3.1d. While this is not representative of new construction, seasoning and/or checking may occur depending on environmental conditions or due to limited material availability. To compensate for the weaking in the specimens (*i.e.*, in which warping was induced by seasoning and checking), these beams were tested arched to leverage the camber.

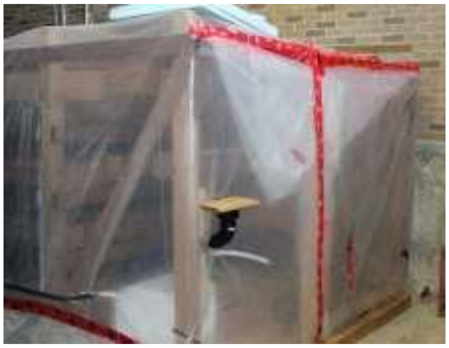

(a) Humidity chamber*

* Reproduced from O’Callaghan (2021)

(b) Representative seasoning detail across depth

(c) End view

(d) Overall warping before testing

Figure 3.1: Humidity environment and effects on timber specimens

3.2.3 Glulam

The six glulam specimens used in this study were obtained from three 6,280 mm (20′-7¼″) lengths of 5-ply 140 mm × 140 mm (5½″ × 5½″) SPF Grade 20f-EX. Due to a manufacturing error, the cross-sections of these specimens were skewed upon arrival. These were thus squared off using a table saw and an orbital sander, resulting in narrower, uniform cross-sections of 110 mm × 140 mm (4¼″ × 5½″). Figure 3.2 shows the cross-sections before and after this process. The specimens were cut to 2,200 mm (7′-2⅝″) lengths for testing under four-point bending, and the offcuts were used to conduct uniaxial parallel-to-grain tension and parallel-to-grain compression tests per ASTM D143, “Standard Test Methods for Small Clear Specimens of Timber” (ASTM, 2021a).

(a) As received (b) Cut and squared

Figure 3.2: Glulam cross-sections for flexural testing

Before testing, the specimens were stored in a humidity chamber, which allowed the specimens to maintain a constant moisture content. The moisture content was measured using a Tramex MRH3 non-destructive digital wood moisture meter. The average moisture content of the glulam at the time of testing was determined to be 9.2% with a CV of 0.06. The average density of the glulam at the time of testing was determined to be 467.7 kg/m^3 with a CV of 0.02.

3.2.4 FRP reinforcement

Two types of reinforcement were investigated in the current study: GFRP fabric and GFRP bars. Both forms of FRP were bound to the base wood material using CSS-ES epoxy primer and saturant manufactured by Simpson Strong-Tie®, a two-part thermoset epoxy resin designed to be used in conjunction with the company’s proprietary Composite Strengthening Systems™ fabrics. To prepare the epoxy for application, its Part A and B components were mixed at a volume ratio of 2:1 using a mixing drill for five minutes, per manufacturer instructions (Simpson Strong-Tie, 2019). After application, the epoxy was cured for at least 48 hours before beam testing. Material properties for the liquid and cured forms of the epoxy used are given in Table 3.1 and Table 3.2, respectively.

Table 3.1: Properties of Liquid Epoxy

Property	Part A	Part B	Mixed
Viscosity [Pa-s]	1040	8	90
Density [kg/L]	1.17	0.97	1.10

Values measured at 22°C.

Reproduced from Simpson Strong-Tie (2019).

Table 3.2: Properties of Cured Epoxy

Property	Test Value
Tensile Strength	36 MPa
Tensile Modulus	2,220 MPa
Rupture Strain	0.0173 mm/mm
Flexural Strength	63 MPa
Flexural Modulus	3,660 MPa
Compressive Strength	109 MPa
Compressive Modulus	2,990 MPa
T_g	62°C
Density	1.15 kg/L

Values measured after curing for 7 days at 22°C.

Reproduced from Simpson Strong-Tie (2019).

The fabrics used in this study were CSS-CUGF27 unidirectional GFRP fabrics manufactured by Simpson Strong-Tie®; their material properties are provided in Table 3.3. For the beams employing this reinforcement material, two layers of this fabric were each saturated with the CSS-ES epoxy and applied to cover the full width of the beam with the primary FRP fibres parallel to the length of the beams.

Table 3.3: Properties of Unidirectional GFRP Fabric

Property	Tensile Strength [MPa]	Tensile Modulus [GPa]	Rupture Strain [mm/mm]	Weight [g/m^2]	Density [g/mm^3]	Thickness per Layer [mm]
Dry Fibre	2,300	72	0.04	915	0.0025	0.36
Cured Laminate*	390	23	0.017	-	-	1.3

* Based on composite with CSS-ES resin cured for 48 hours at 60°C.

Reproduced from Simpson Strong-Tie (2020).

Ribbed GFRP rebar was chosen over smooth GFRP bars to take advantage of added mechanical interlock and slip resistance provided by its ridged geometry (Sólyom et al., 2015). The bars used in this study were straight ComBAR® ribbed GFRP bars manufactured by Fiberline Composites. To maintain a consistent area-reinforcement ratio across beams with different widths, different GFRP bar sizes were selected accordingly: M15 for the sawn timber beams and M13 for the glulam beams. The geometric and material properties of these bars are provided in Table 3.4 and Table 3.5, respectively.

Table 3.4: Geometric Properties of GFRP Bars

Designated Diameter (ACI/CSA)	Core Diameter [mm]	Exterior Diameter [mm]	Cross-section Area [mm^2]	Specific Weight [kg/m]
M13	13	14.5	132	0.34
M15	16	18	201	0.53

Reproduced from Fiberline Composites (2017).

Table 3.5: Material Properties of GFRP Bars

Property	Term	Value*
Ultimate Tensile Strength	f_u	> 1,000 MPa
1,000-hour tensile strength	F_{k1000h}	950 MPa
Logarithmic temporal slope	R_{10}	< 15%
Modulus of Elasticity	E_f	> 63.5 GPa
Ultimate Elongation	ε_{Fu}	1.67%
Bond Strength	τ_F	12.2 MPa
Bar Surface Profile Factor (bond)	$K5$	≤ 1.0
Bond Coefficient	k_b	0.6
Bar Surface Factor	k_4	≤ 0.8
Transverse Shear Strength	T	≥ 180 MPa
Fibre Content	-	> 75% (vol.)

* Based on M15 bars.

Reproduced from Fiberline Composites (2017).

3.3 Methodology

3.3.1 Overview

This section will introduce and discuss the retrofit schemes and the test matrix used to obtain the results used in the analysis portion of this study.

3.3.2 Reinforcement schemes

Two basic retrofit schemes were studied for each type of beam: GFRP fabric and GFRP bars. Reinforcement was applied over a length of 1,775 mm (5′-9⅞″) centred between supports as per Section 16.13 of CSA S6, the "Canadian Highway Bridge Design Code." Figure 3.3 shows the reinforcement schemes for both types of reinforcement.

Reinforcement ratios were chosen to be within the recommendations proposed by Plevris & Triantafillou (1992), who found an effective upper limit to the useful ratio of FRP reinforcement in wood to be approximately 3%; any greater proportion of GFRP would provide only diminishing returns to flexural strength. In the current study, reinforcement ratios of approximately 2% of the wood cross-section were targeted, with the actual reinforcement ratios achieved for each reinforcement type given in Table 3.6. These numbers correspond to two layers of GFRP fabric for the sawn timber and glulam specimens, two M15 bars for the sawn timber specimens, and two M13 bars for the glulam specimens.

Table 3.6: Reinforcement Ratios

Wood Base	**GFRP Reinforcement Ratios**	
	Fabric	**Bar**
Sawn Timber	1.86% (2-ply)	2.16% (2×M15)
Glulam	1.86% (2-ply)	1.81% (2×M13)

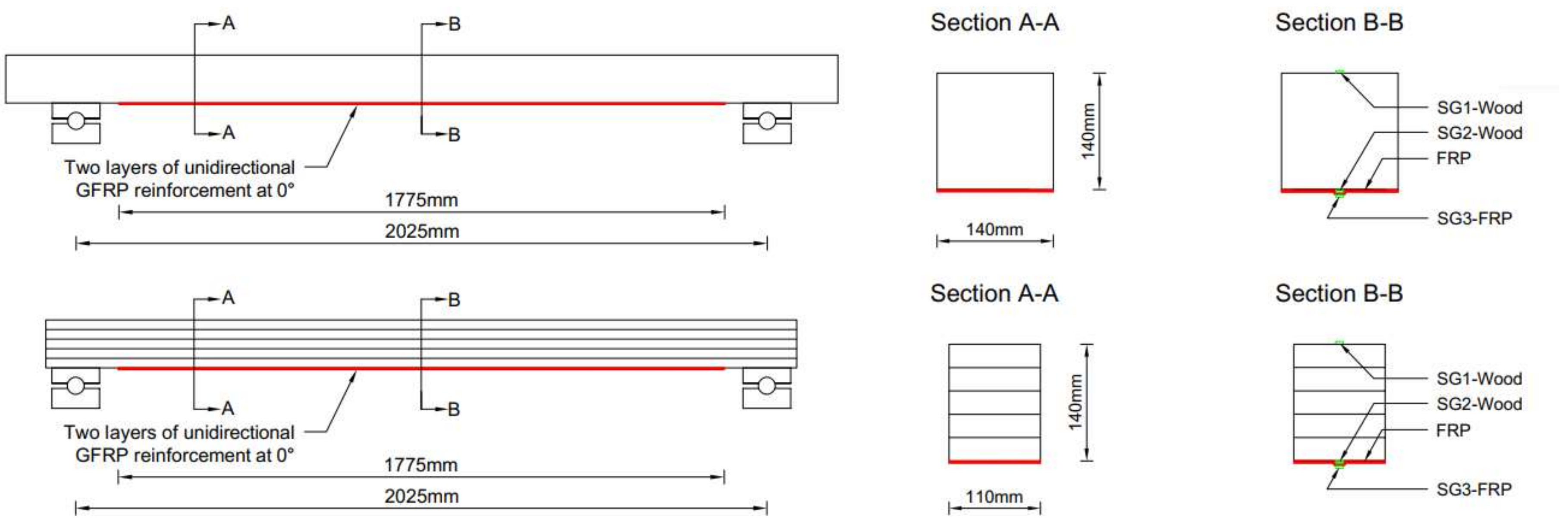

(a) Reinforcement with FRP fabric

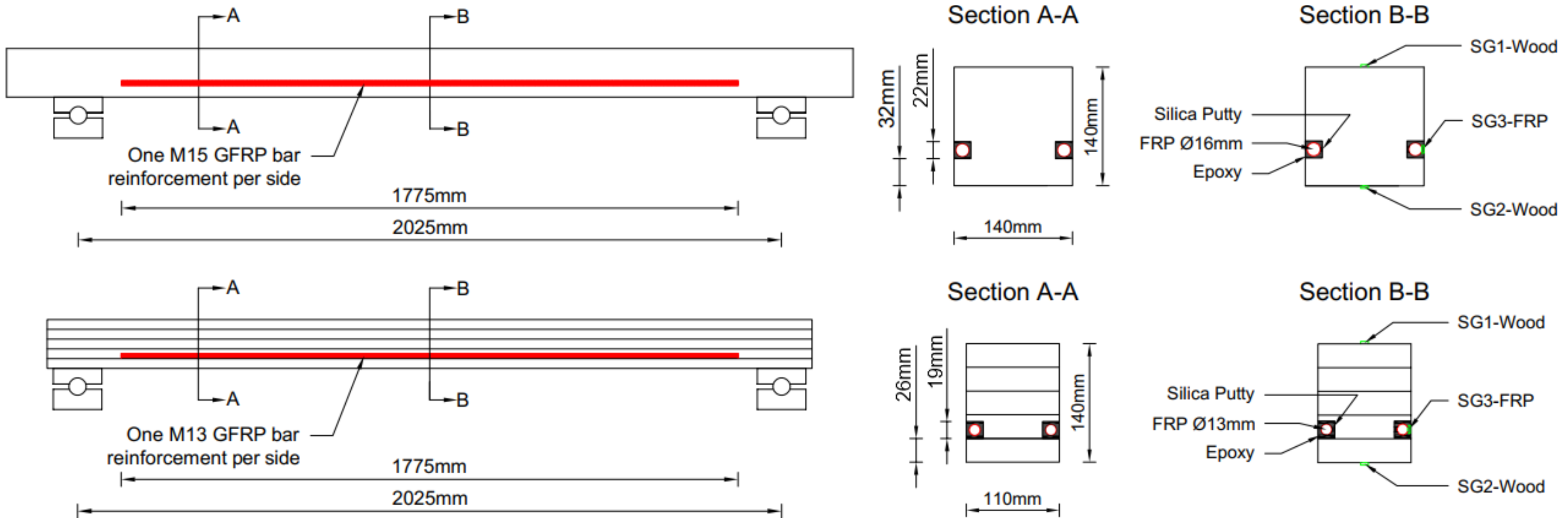

(b) Reinforcement with FRP bars

SG = strain gauge

Figure 3.3: GFRP reinforcement schemes

3.3.3 Test matrix

Of the five sawn lumber specimens, one beam was left unreinforced, two beams were reinforced with GFRP fabric, and two beams were reinforced with GFRP bars. Similarly, of the six glulam specimens, two beams were left unreinforced, two beams were reinforced with GFRP fabric, and two beams were reinforced with GFRP bars. The test matrix is summarized in Table 3.7. To label the test specimens, each beam was assigned a letter, either G for glulam or S for sawn timber, to represent the base material. This was followed by another letter, B for bar, F for fabric, or N for none, to represent the reinforcement scheme. Finally, a number was assigned to sequentially identify the wood-reinforcement combination. For example, the two glulam control specimens in the set were labelled as GN-1 and GN-2.

Table 3.7: Test Matrix

Wood Base	**GFRP Reinforcement Type**			**Specimen**
	None (N)	**Fabric (F)**	**Bar (B)**	**Total**
Sawn Timber (S)	1	2	2	5
Glulam (G)	2	2	2	6
Specimen Total	3	4	4	11

The sequence of beam testing followed a randomized block test. The purpose of the block sequence design was to address transient environmental factors (*e.g.*, humidity, temperature) over the full duration of testing all specimens, which spanned two weeks, thereby improving the comparability of the test results. Constraints in the availability of the test apparatus required that all bar-reinforced beams, which were the slowest to cure, needed to be tested in their block as shown in Table 3.8. The extended overall time required for the bars was because the bars could only be installed on one face at a time, and thus required separate days to cure.

Table 3.8: Test Order

Group	**Sequence**
Block 1	GN-1, SF-1, GF-1, SN-1
Block 2	GN-2, SF-2, GF-2
Block 3	SB-1, GB-1, SB-2, GB-2

3.4 Instrumentation and Specimen Preparation

3.4.1 Overview

To study reinforced beam behaviour relative to the unreinforced, strain gauges were applied to the wood compression and tension surfaces as well as the GFRP surfaces at mid-span (Figure 3.3). The following sub-sections describe the process of preparing the beams for flexural testing.

3.4.2 Application of strain gauges

Each beam was fitted with a minimum of two strain gauges: one located at midspan on the tension face and another at midspan on the compression face, both aligned longitudinally and parallel to the wood fibres. To promote adequate bonding and measurements, the points of application were sanded flat, and the resulting dust was blown out before gauge application. Strain gauges were adhered using a thin layer of cyanoacrylate superglue, then covered using a small amount of silica putty to protect the gauges from abrasion in transport and, if applicable, to isolate them from subsequent layers of GFRP.

Strain gauges were also applied directly to the GFRP reinforcement at midspan. Using a similar process to that described above for the wood surfaces, cured laminates were sanded locally to form a flush surface on the extreme tension face on which to apply the strain gauges longitudinally. This was done by using a rotary drum sander to work through the hardened fabric to the centre of the weave in the outermost layer; this small modification to the reinforcement has not been shown to affect the overall strength and mode of failure (Lacroix & Doudak, 2018a, 2020; O'Callaghan, 2021). Strain gauges were adhered using a thin layer of cyanoacrylate superglue, then covered using a small amount of silica putty to protect the gauges from abrasion in transport. Figure 3.4 shows the relative positioning of the midspan strain gauges on the wood surface (*i.e.*, under the GFRP) and on the outer GFRP surface.

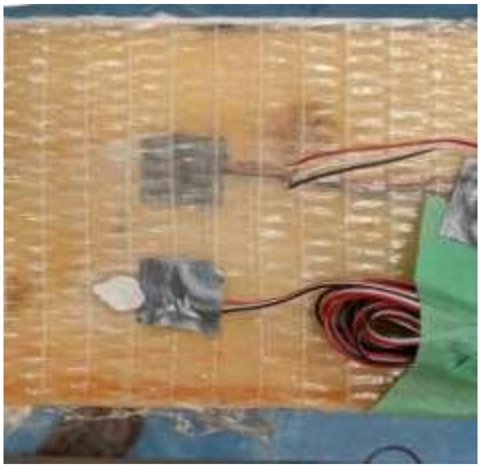

Figure 3.4: Strain gauge installation on GFRP laminates

On beams reinforced with GFRP bars, one of the two GFRP bars was instrumented with a strain gauge at midspan, oriented longitudinally, facing outward to obtain average strains experienced in the bars. A rotary drum sander was used to cut through the outer grooves to create a flush surface for the strain gauges, which can be seen in Figure 3.5a. The strain gauges were adhered using a thin layer of cyanoacrylate superglue, then covered using a small amount of silica putty to protect the gauges from abrasion in transport and from the epoxy fill, as shown in Figure 3.5b.

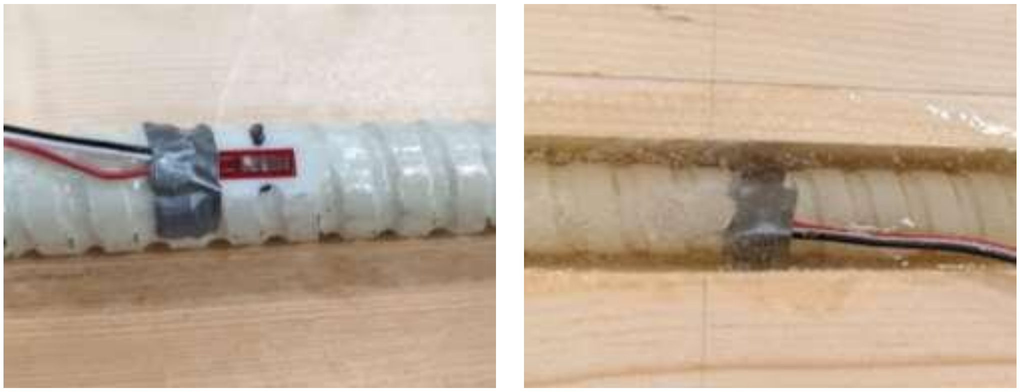

(a) Uncovered strain gauge (b) Covered, filled, and cured

Figure 3.5: Strain gauge installation on GFRP bar

3.4.3 Application of GFRP fabric

Surface preparation was required before the fabric application to promote an adequate bond of the epoxy between the wood and FRP. The surfaces of the two sawn lumber specimens were naturally rough and did not require specific treatment. The two glulam specimens, on the other hand, were roughened on the tension face using a wire brush. This was done to promote adequate adhesion of the epoxy with the wood and fabric. As described in the previous section, the strain gauge locations were sanded flat. Just before GFRP fabric application, the final step of the surface preparation procedure was to saturate the wood surface with a layer of epoxy resin (Figure 3.6a). For each beam reinforced with GFRP fabric, two layers of unidirectional (0°) GFRP fabric were cut (Figure 3.6b) and applied on the tension face such that the fibres ran parallel to the span length (Figure 3.6c) to achieve the reinforcement ratios given in Table 3.6. GFRP fabric strips were saturated with the epoxy and the excess was squeezed out using a window squeegee. The first layer of saturated fabric was applied to the tacky wood surface, and any resulting air pockets were eliminated along with further excess epoxy using a ribbed fibreglass roller. This procedure was repeated with the second and final layer of saturated fabric. Once hardened, another strain gauge was instrumented on the GFRP surface at midspan. The fabric-reinforced specimens were allowed to cure for at least 48 hours before testing (Figure 3.6d).

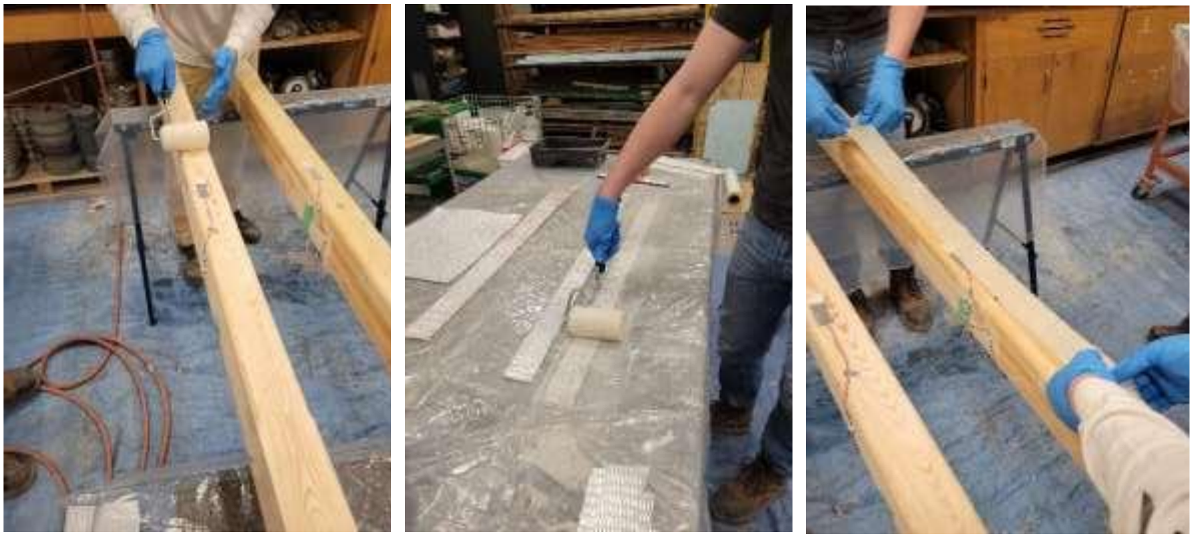

(a) Coating the glulam beam* (b) Saturating the FRP fabric* (c) Applying the wet FRP*

* Reproduced from Vetter (2022)

(d) Cured GFRP laminates on sawn timber (left) and glulam (right)

Figure 3.6: Application procedure for GFRP fabric

3.4.4 Application of GFRP bars

Two sawn and two glulam specimens were each reinforced with two ridged GFRP bars, one on either side of the tension face's width, to achieve the reinforcement ratios given in Table 3.6. Side access, as opposed to bottom access, permits easier installation and maintenance of timber beams reinforced *in situ*. Using a router, grooves were cut to 22 mm (⅞″) wide, 22 mm (⅞″) deep, and a minimum of 32 mm (1¼″) from the tension face of the sawn lumber specimens. On the glulam specimens, on account of the smaller bar diameters, groove widths and depths were reduced both to 19 mm (¾″) and the wood cover was reduced to 26 mm (1″). The edge distance from the tension face was chosen based on CSA S6 guidelines and to study the effect of placing the reinforcement higher in the beam. Debris was blown out using pressurized air, and any ridges left from the routing process were left to assist the epoxy bond. Dots of silica putty were inserted at three points in each groove for the GFRP bars to rest upon such that the bars would not rest directly on the wood surface. Working one side at a time, the bars were inserted, and the grooves were filled with the CSS-ES two-part epoxy resin (Figure 3.7a). The sides of the beam were tapped with a rubber mallet to help liquid epoxy settle through tighter crevices and to release large bubbles, which would negatively affect the bond and overall strength. The epoxy on each side was allowed to cure fully before further disturbance (Figure 3.7b). Given that not all sawn lumber specimens were perfectly straight or flat, some beams had low points in the resin which sat 1-2 mm below the surface (Figure 3.7c); however, care was taken to ensure bars remained fully engulfed in resin at all points.

(a) Before and after filling (b) After curing

(c) Overall side views

Figure 3.7: Application procedure for GFRP bars

3.5 Test Apparatus and Procedure

A total of eleven full-scale beams were tested statically under four-point bending. The tests were conducted in accordance with ASTM D198, "Standard Test Methods of Static Tests of Lumber in Structural Sizes" (ASTM, 2021b). All beams were loaded using a 500 kN hydraulic load frame with a load cell connected to an actuator. The loading was applied through a spreader beam and bearing blocks. The bearing blocks were constructed from hardwood to have a radius of over two times the beam depths per ASTM D198 (ASTM, 2021b). Simple-support boundary conditions were achieved using an anchored pin and roller system. These supports were braced laterally, although this was not explicitly required by the ASTM standard because the depth-to-width ratios did not exceed three. A load-span-to-depth (*a*/*d*) ratio of 4.8 was used.

Before applying GFRP reinforcement, the beams were pre-loaded to record the wood bending stiffness. The control and retrofitted beams were loaded in displacement control until failure, with loading protocols ranging from 3.5 mm/min to 10 mm/min to ensure ultimate failure within five and ten minutes, following the ASTM D198 standard (ASTM, 2021b). During the tests, a data acquisition system recorded the data at a sampling rate of 15 samples per second. The applied load, midspan deflection, and shear-free deflection were measured using, respectively, the frame load cell, a linear position transducer ("string potentiometer" or "string pot"), and a linear variable displacement transducer (LVDT) in the shear-free region. Additionally, the wood and FRP strains were recorded at midspan using strain gauges as described in Section 3.4.2. Before testing, weight and moisture readings were taken and documented along with the visual observation of the specimens. Documentation and photographs of the failed specimens were also recorded. Figure 3.8 shows a representation of the actual test set-up with its instrumentation.

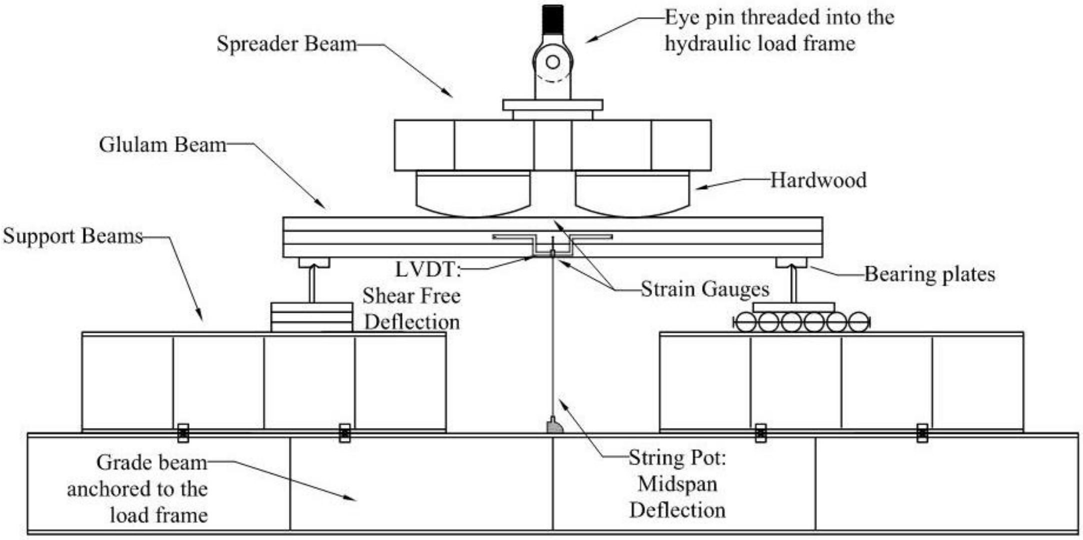

Reproduced from Vetter (2022)

Figure 3.8: Static bending test setup

3.6 Component Properties

3.6.1 Overview

Component tests were conducted on the wood and FRP materials to obtain pure-compression and pure-tension properties to input into the analytical models. Test methods and procedures for samples of clear-sawn timber and glulam, GFRP laminates, and GFRP bars were conducted following sections.

3.6.2 Wood coupons

Eighteen wood samples were obtained from the respective batches for uniaxial testing: six tension coupons for sawn timber, six tension coupons for glulam, and six compression coupons for glulam. These samples were cut to size and tested for pure compression and pure tension per ASTM D143, "Standard Test Methods for Small Clear Specimens of Timber" (ASTM, 2021a). Size effect adjustments will then be applied to the coupon data as described in Section 2.5.5 and 5.3.2. Data for the sawn timber under uniaxial compression was obtained previously at full scale by O'Callaghan (2021).

Compression coupons, shown in Figure 3.9a, with final dimensions of 50 mm × 50 mm × 200 mm (2″×2″×8″), were prepared from extra glulam material using a guided table saw. A 500 kN hydraulic test frame, shown in Figure 3.9b, loaded the coupons in compression and recorded the applied force. The displacement was recorded using an LVDT and was used to calculate the relative change in length (*i.e.*, strain).

(a) Test coupons (b) Test apparatus

Reproduced from Vetter (2022)

Figure 3.9: Wood compression coupons

Tension coupons, shown in Figure 3.10a, were prepared from extra sawn timber and glulam material. The general shape of the specimens was cut out using a bandsaw and finished on a belt sander to smoothen any irregularities. The final cross-section area was 5 mm × 10 mm (⅜″ × $^{3}/_{16}$″). A 10 kN electromechanical frame, shown in Figure 3.10b, pulled the coupons until failure and recorded the applied force. A 50.8 mm extensometer, placed at mid-height, was used to calculate the displacement and the relative change in length during the test.

(a) Test coupons (b) Test apparatus

Reproduced from Vetter (2022)

Figure 3.10: Wood tension coupons

3.6.3 GFRP coupons

Tensile properties for the GFRP materials used in this study were conducted previously by Vetter (2022) for the GFRP laminates (Figure 3.11) and by Lochan (2021) for the GFRP bars (Figure 3.12). The respective tests were conducted per ASTM D3039, “Standard Test Method for Tensile Properties of Polymer Matrix Composite Materials” (ASTM, 2017) and ASTM D7205, “Standard Test Method for Tensile Properties of Fiber Reinforced Polymer Matrix Composite Bars” (ASTM, 2011b).

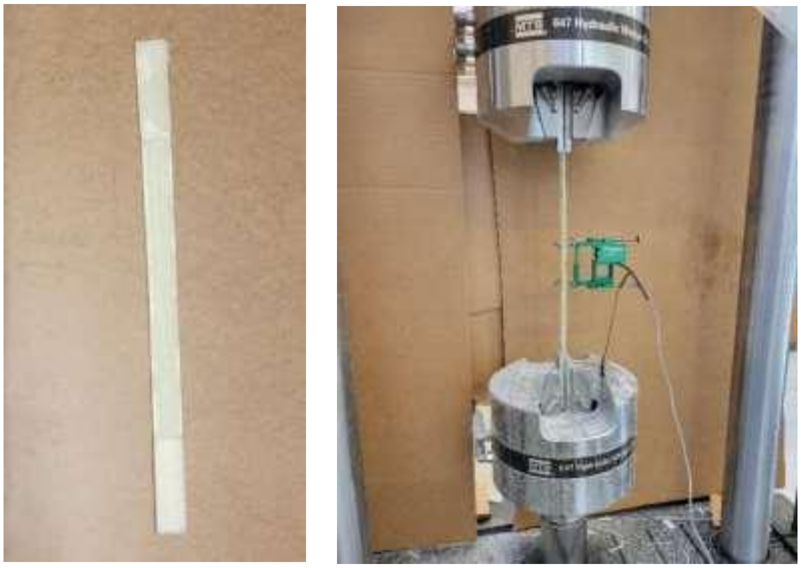

(a) Test coupon (b) Test apparatus

Reproduced from Vetter (2022)

Figure 3.11: GFRP-fabric coupons

(a) Test coupons (b) Test apparatus

Figure 3.12: GFRP-bar coupons

Chapter 4

Experimental Results

4.1 General

This chapter presents the findings from the experimental testing of the material components (*i.e.*, sawn timber, glulam, and GFRP materials) and the full-scale beams described in the previous chapter. The following sections provide the numerical data from each test conducted and describe observations of their failure mechanisms.

4.2 Component Test Results

4.2.1 Overview

This section presents the failure mechanisms and numerical findings of each material component in isolation. Figures and stress-strain data for each test sample can be found in Appendix A for the wood compression coupons and in Appendix B for the wood tension coupons.

4.2.2 Wood compression

Parallel-to-grain compression tests were conducted to provide inputs to the analytical model to predict the flexural response of unreinforced and FRP-reinforced wood beams. The sawn timber specimens tested in flexure in the current research program were obtained as remnants from full-scale compression tests by O'Callaghan (2021). The focus of O’Callaghan’s research was on the effects of GFRP reinforcement on the compressive behaviour of SPF members; as a result, a total of six 140 mm × 140 mm (nominal 6×6) × 685 mm SPF Grade No. 2 or better members were tested in compression parallel-to-grain. Figure 4.1 shows representative failure modes observed in the unreinforced specimens, including splitting, crushing, and wedge splitting. The stress-strain curves for the six timber specimens are shown in Figure 4.2 along with their average curve.

(a) Splitting (b) Crushing (c) Wedge splitting

Reproduced from O'Callaghan (2021)

Figure 4.1: Representative compressive failure modes of unreinforced full-scale timber

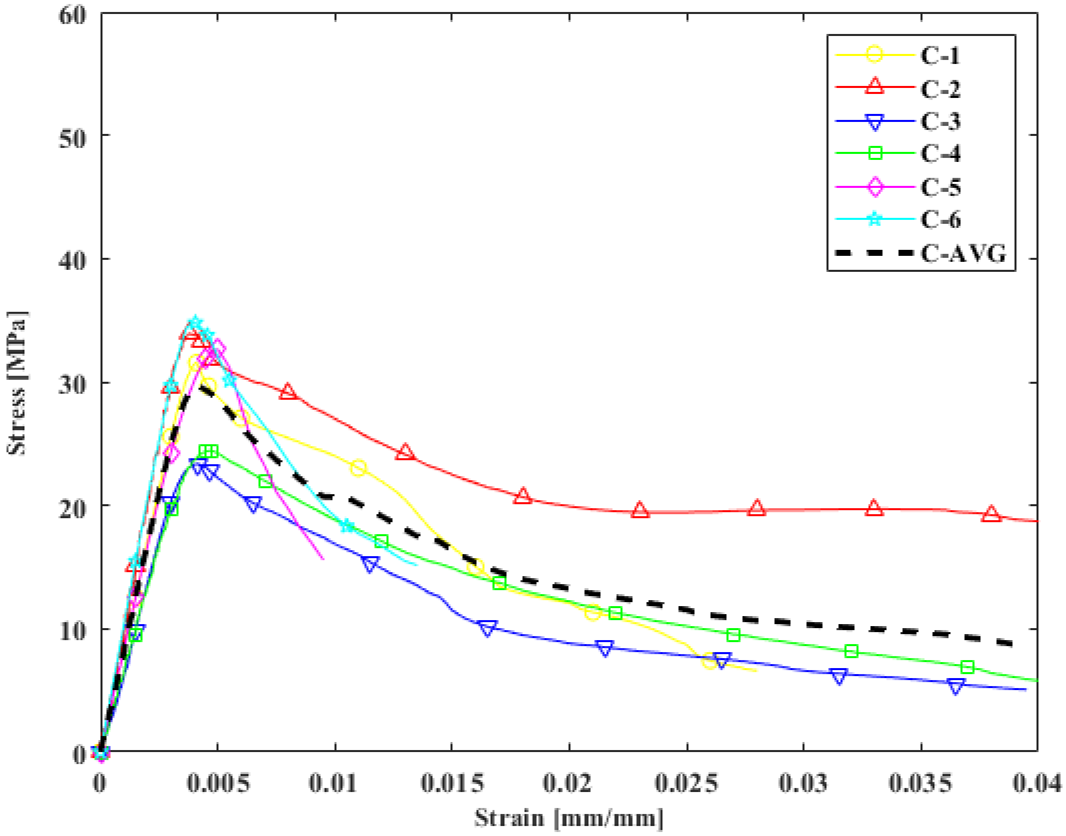

Reproduced from O'Callaghan (2021)

Figure 4.2: Experimental compressive stress-strain behaviour of full-scale timber

Table 4.2 summarizes key values from the sawn timber specimens tested in compression parallel-to-grain. The values presented are the compressive modulus of elasticity (MOE); compressive yield strength (f_{cy}), the maximum stress resisted by each specimen; compressive yield strain (ε_{cy}), the strain value corresponding to f_{cy}; compressive ultimate strength (f_{cu}), which is defined as the stress resisted before failure; and compressive ultimate strain (ε_{cu}), which is the strain value corresponding to f_{cu}.

Table 4.1: Results of Parallel-to-Grain Compression on Full-Scale Sawn Timber Specimens

ID	MOE $^{a)}$	f_{cy} $^{b)}$	ε_{cy} $^{c)}$ ×$10^{3)}$	f_{cu} $^{d)}$	ε_{cu} $^{e)}$ ×10^{3}
#	[GPa]	[MPa]	[mm/mm]	[MPa]	[mm/mm]
C-1	8.66	31.6	4.06	6.6	2.82
C-2	10.18	34.0	3.78	11.5	7.23
C-3	7.22	23.4	4.06	5.1	4.04
C-4	6.47	24.5	4.68	4.2	4.78
C-5	8.25	32.7	5.09	14.3	0.98
C-6	10.00	34.8	4.06	13.9	1.38
Average	8.47	30.2	4.29	9.3	3.54
Std. Dev.	1.36	4.5	0.45	4.1	2.1
CV	0.16	0.15	0.10	0.44	0.60

Reproduced from O'Callaghan (2021).

a) Compressive modulus of elasticity derived as 10-40% of the stress-strain slope

b) Compressive yield (maximum) strength

c) Compressive yield strain

d) Compressive ultimate (failure) strength

e) Compressive ultimate strain

Whereas full-scale data was available for the sawn timber, it was not economical to conduct full-scale tests for the glulam. Compression tests are usually conducted on small-scale specimens and then adjusted for size effects as described in Section 2.5.5 and 5.3.2 (Buchanan, 1990; Lacroix, 2017a; Vetter, 2022).

Representative failure modes—including splitting, crushing, and wedge splitting—of unreinforced glulam coupons subjected to axial compression parallel-to-grain are shown in Figure 4.3. Detailed failure modes of all glulam compression coupons at failure can be found in Appendix A. The stress-strain curves for the six specimens are shown in Figure 4.4 along with their average curve.

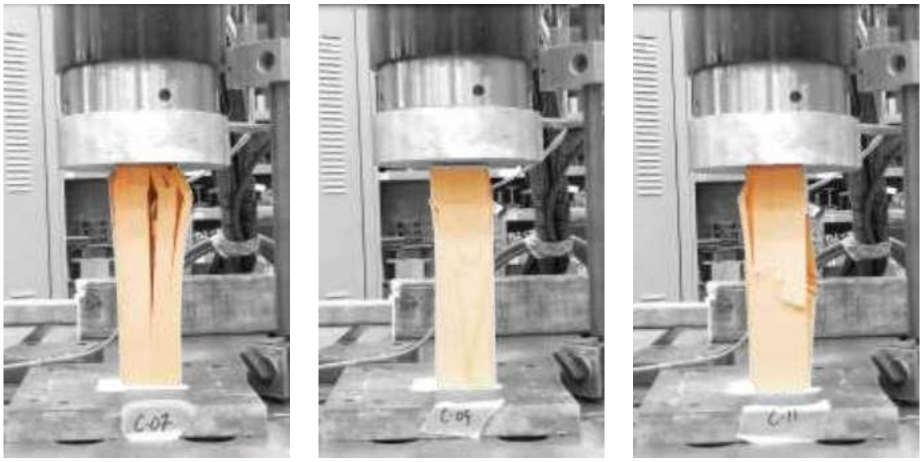

(a) Splitting (b) Crushing (c) Wedge splitting

Figure 4.3: Representative compressive failure modes of unreinforced glulam coupons

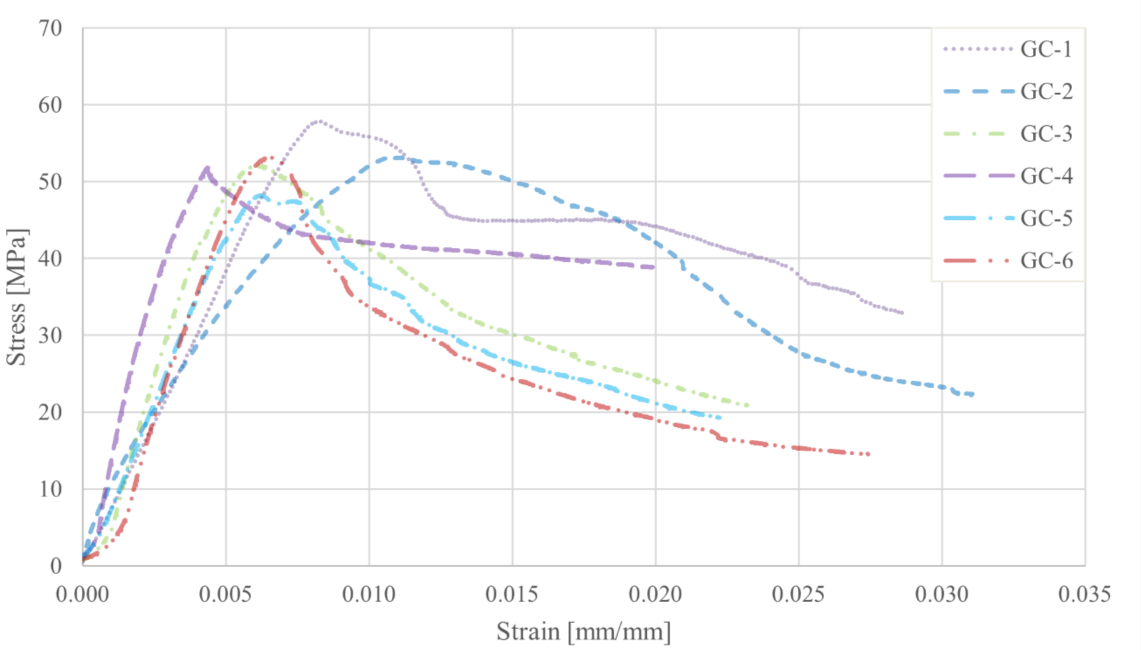

Figure 4.4: Experimental compressive stress-strain behaviour of small-scale glulam

Table 4.2 summarizes key values from the sawn timber and glulam compression specimens. Values of interest presented in this table are the compressive modulus of elasticity (MOE); compressive yield strength (f_{cy}), defined as the maximum stress resisted by each specimen; compressive yield strain (ε_{cy}), the strain value corresponding to f_{cy}; compressive ultimate strength (f_{cu}), the stress resisted before failure; and compressive ultimate strain (ε_{cu}), which is the strain value corresponding to f_{cu}.

Table 4.2: Results of Parallel-to-Grain Compression on Small-Scale Glulam Specimens

ID \#	MOE [a] [GPa]	f_{cy} [b] [MPa]	ε_{cy} [c] $\times 10^3$ [mm/mm]	f_{cu} [d] [MPa]	ε_{cu} [e] $\times 10^3$ [mm/mm]
GC-1	7.6	57.8	8.31	32.8	28.7
GC-2	5.5	53.2	10.86	22.3	31.3
GC-3	12.2	52.1	6.12	20.9	23.2
GC-4	14.7	51.8	4.35	38.9	19.9
GC-5	9.2	48.2	6.24	19.3	22.2
GC-6	11.3	53.1	6.48	14.5	27.4
Average	10.1	52.7	7.06	24.8	25.4
Std. Dev.	3.3	3.1	2.25	9.1	4.3
CV	0.33	0.06	0.32	0.37	0.17

a) Compressive modulus of elasticity
b) Compressive yield (maximum) strength
c) Compressive yield strain
d) Compressive ultimate (failure) strength
e) Compressive ultimate strain

4.2.3 Wood tension

A total of twelve tension tests were conducted on sawn timber and glulam coupons to provide inputs to the analytical models. Stresses were calculated as the ratio of applied load over the smallest perpendicular cross-section area; strains were calculated as the ratio between the measured elongation of the uniform section over its original length. Figure 4.5 shows the tensile failure of each material type in the test apparatus. Figures for all tension coupons at failure can be found in Appendix B. Stress-strain relationships for each sawn timber specimen are aggregated in Figure 4.6a along with their average, and similarly for each glulam specimen in Figure 4.6b. The sawn timber and glulam were observed to behave linearly up to failure, where they failed in a brittle fashion.

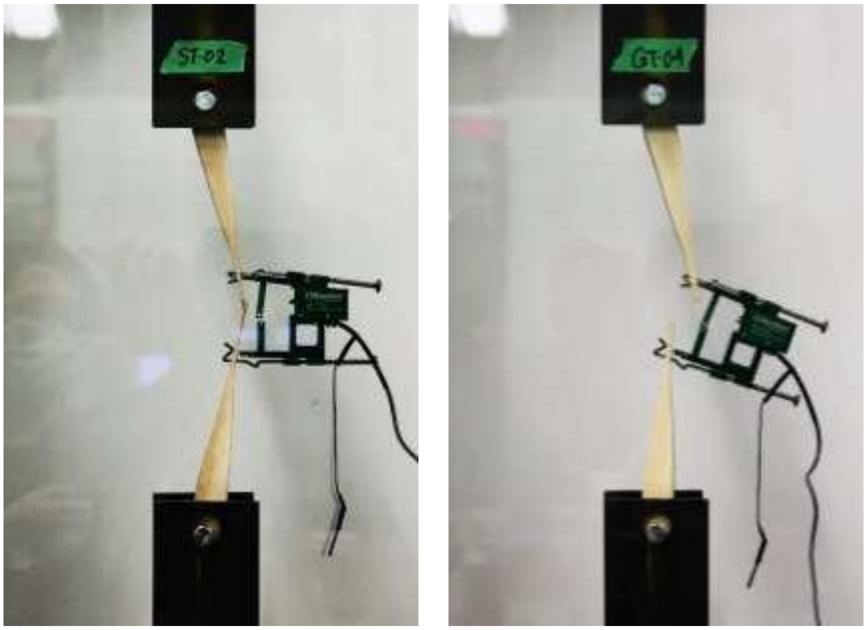

(a) Sawn timber (b) Glulam

Figure 4.5: Representative failure of tension coupons

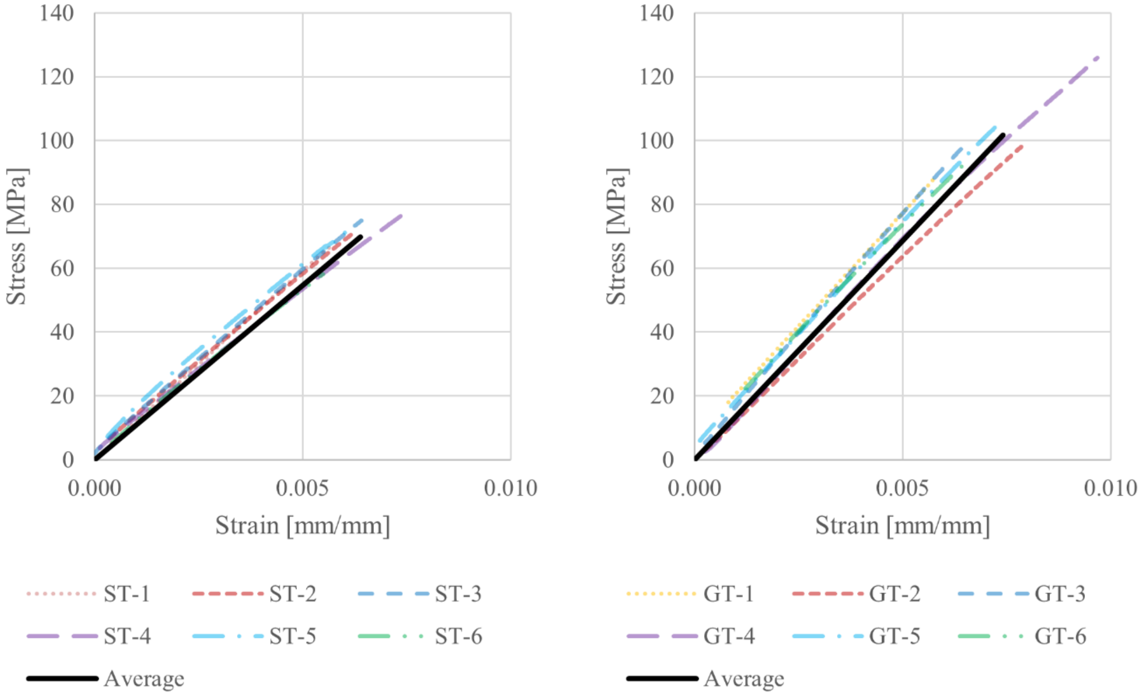

(a) Sawn timber (b) Glulam

Figure 4.6: Average experimental stress-strain behaviour of tension coupons

Table 4.3 summarizes key values from the sawn timber and glulam tension coupons. Values of interest presented are the tensile MOE, the tensile ultimate or failure strength (f_{tu}), and the corresponding tensile ultimate strain (ε_{tu}).

Table 4.3: Results of Static Tension Tests on Wood Coupons

Sawn timber				Glulam			
ID #	**MOE [a] [GPa]**	**f_{tu} [b] [MPa]**	**ε_{tu} [c] $\times 10^3$ [mm/mm]**	**ID #**	**MOE [a] [GPa]**	**f_{tu} [b] [MPa]**	**ε_{tu} [c] $\times 10^3$ [mm/mm]**
ST-1	11.8	67.5	5.73	GT-1	14.1	88.8	5.81
ST-2	11.0	70.6	6.17	GT-2	12.7	98.5	7.89
ST-3	11.3	75.0	6.41	GT-3	15.1	99.2	6.53
ST-4	10.0	76.3	7.35	GT-4	13.3	125.9	9.68
ST-5	11.2	71.6	6.06	GT-5	13.9	104.1	7.22
ST-6	10.4	58.2	5.49	GT-6	13.4	94.0	6.59
Average	11.0	69.9	6.20	**Average**	13.7	101.8	7.29
Std. Dev.	5.1	32.8	2.92	**Std. Dev.**	7.1	53.4	3.90
CV	0.47	0.47	0.47	**CV**	0.52	0.53	0.53

a) Tensile modulus of elasticity

b) Tensile ultimate (failure) strength

c) Tensile ultimate strain

4.2.4 FRP tension

The tensile properties of the 2-ply unidirectional FRP fabric-laminates used were determined by Vetter (2022) and the tensile properties of the 13-mm and 16-mm FRP bars used were determined by Lochan (2021). A representative sample of each FRP material before and upon tensile failure is shown in Figure 4.7. Despite being of different shapes and forms, both FRP materials exhibited sudden and severe splintering upon failure as the fibre components ruptured and the weaker polymer matrix could no longer bind them together. Brittle failure can also be observed in the stress-strain relationships shown in Figure 4.8 and Figure 4.9, respectively.

(a) 2-ply unidirectional laminate[1] (b) 13-mm bar[2]

Reproduced from 1. Vetter (2022) and 2. Lochan (2021)

Figure 4.7: GFRP specimens before and after tension testing

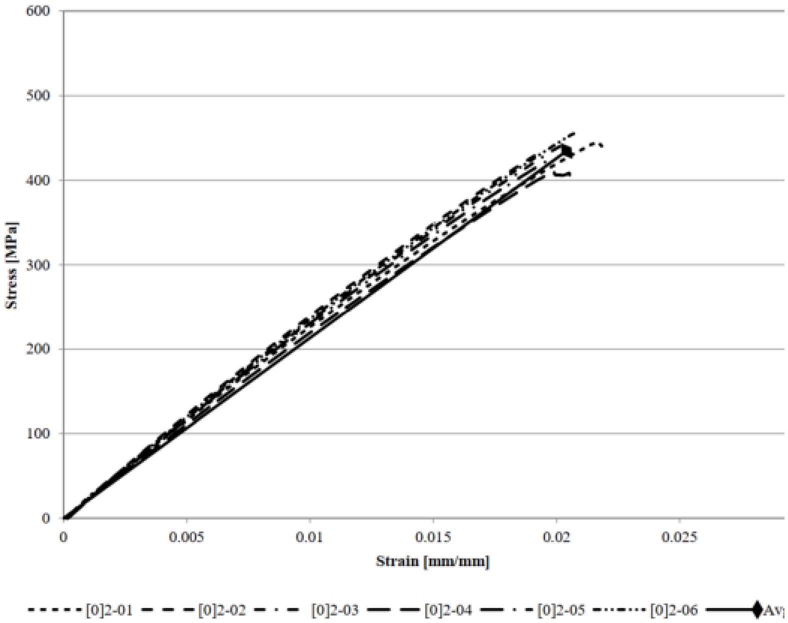

Reproduced from Vetter (2022)

Figure 4.8: Representative stress-strain curves for GFRP fabric-laminates in tension

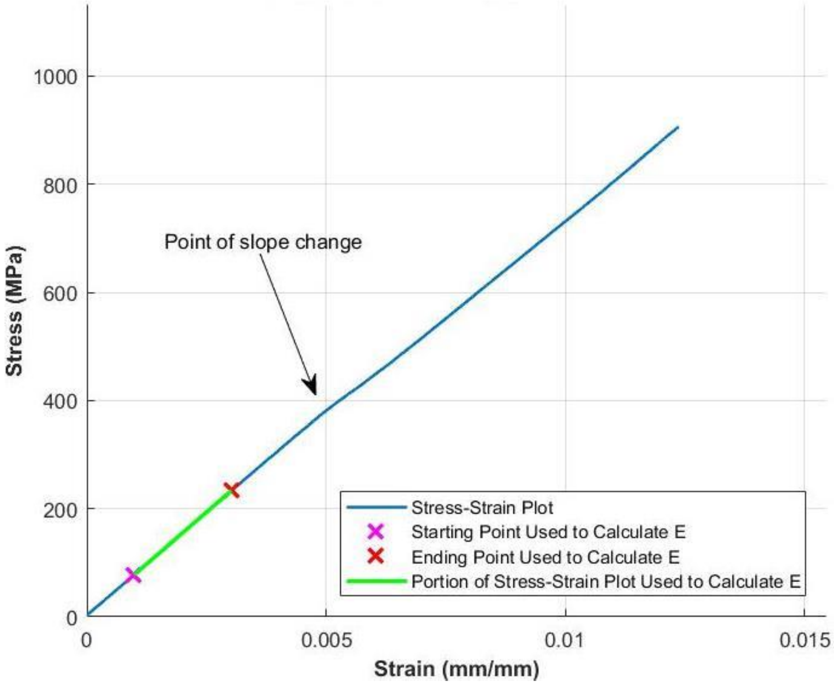

(a) M13 GFRP bar (13 mm diameter)

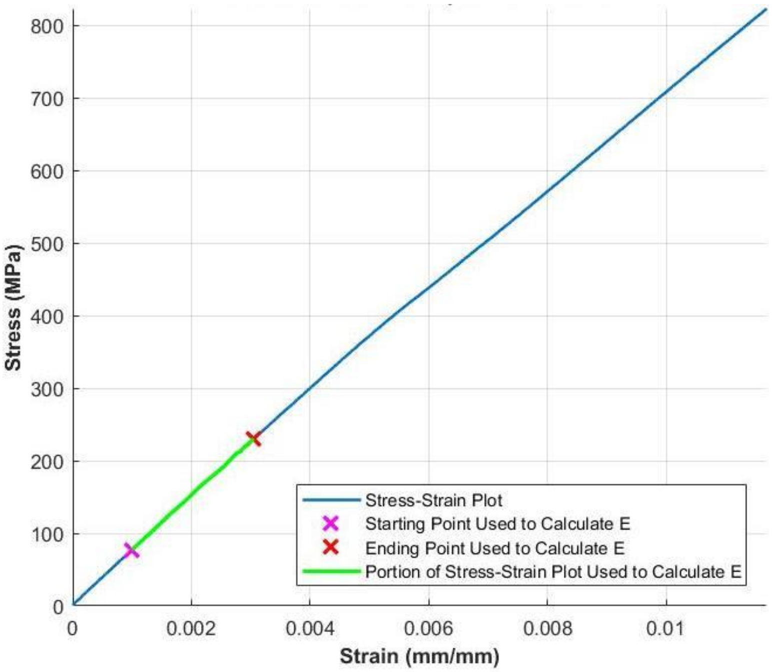

(b) M15 GFRP bar (16 mm diameter)

Reproduced from Lochan (2021)

Figure 4.9: Representative stress-strain curves for GFRP bars in tension

Table 4.4 summarizes key values from each of the FRP fabric and bar reinforcements. Values of interest presented are the tensile MOE, the tensile ultimate or failure strength (f_{FRP}), and the corresponding tensile ultimate strain (ε_{FRP}).

Table 4.4: Results of Static Tension Tests on GFRP

FRP Type		**MOE** [a] **[MPa]**	**f_{FRP}** [b] **[MPa]**	**ε_{FRP}**[c] **×10^3 [mm/mm]**
Fabric-Laminate [d]	Average	23.5	434.6	20.4
	Std. Dev.	0.7	14.8	0.8
	CV	0.03	0.03	0.04
Bar, 13 mm [e]	Average	76.8	1,231	16.0
	Std. Dev.	0.5	23.5	0.3
	CV	0.01	0.02	0.02
Bar, 16 mm [e]	Average	75.0	1209	16.1
	Std. Dev.	0.5	22.4	0.8
	CV	0.01	0.02	0.02

a) Tensile modulus of elasticity

b) Tensile yield (maximum) strength

c) Tensile yield (maximum) strain

d) Vetter (2022)

e) Lochan (2021)

4.3 Bending Test Results

4.3.1 Overview

This section presents the failure mechanisms and numerical findings of each beam and reinforcement group. Figures for the individual beam tests can be found in Appendix C. Load-, displacement-, and strain-time data can be found in Appendix D.

4.3.2 Control specimens

Wood beams loaded under four-point bending experience their maximum moment between the points at which the loads are applied, and thus failure is usually initiated at a knot or defect within this zone. This phenomenon is demonstrated in the sawn timber control specimen, SN-1 (Figure 4.10), whereupon failure can be traced to originate from a large knot on the tension face in the high-stress region.

(a) Start of test

(b) Initial failure

(c) Crack propagation

(d) Crack origin detail

Figure 4.10: Representative failure progression of unreinforced sawn timber

Cracks were formed similarly in the glulam control beams GN-1 and GN-2 (Figure 4.11). Notably, failure occurred sequentially, distinctly ply-by-ply; cracks would propagate through one layer at a time before being temporarily “reset” at each glued interface for which the crack pattern followed the path of least resistance.

(a) Peak loading (b) Initial failure

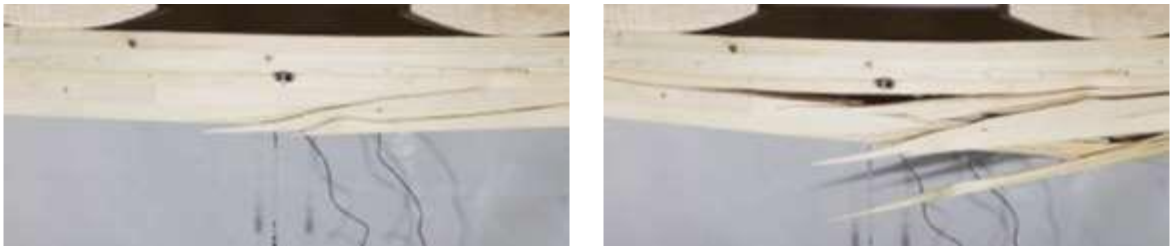

(c) Failure through second layer (d) Splitting at glue line

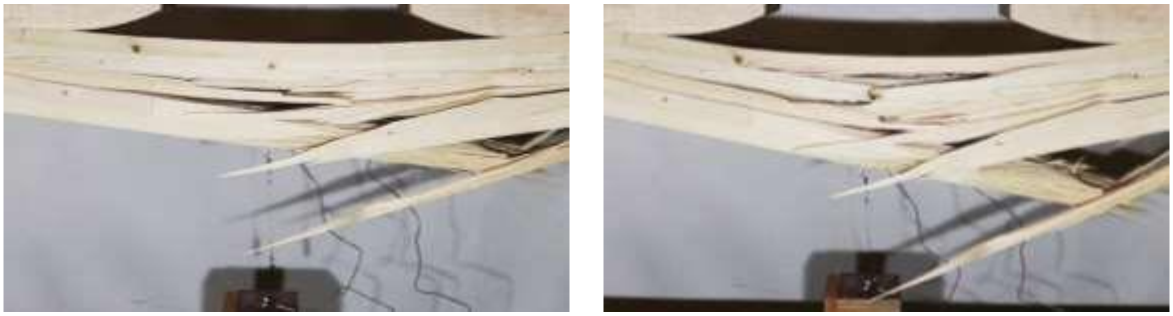

(e) Failure through third layer (f) Failure through fourth layer

Figure 4.11: Representative failure progression of unreinforced glulam

Figure 4.12 shows the load-displacement behaviour of the sawn timber and glulam control specimens. Whereas the sawn timber beam failed shortly after peak loading, both glulam beams exhibited some level of post-peak behaviour or residual capacity after initial failure. Furthermore, smaller peaks can be seen in the glulam plots, each corresponding with the failure of a wood layer.

Table 4.5 summarizes key values from the sawn timber and glulam control beams. Values of interest presented are the peak or maximum load resistance (P_{max}); its corresponding midspan displacement ($\Delta_{P,max}$) as measured by the string pot; the flexural modulus of rupture (MOR), equal to the maximum bending resistance divided by the beam's elastic section modulus; the bending stiffness (K), derived as the slope of the initial rising arm in the load-displacement plot of the unreinforced beam corresponding with the first 10–40% of the maximum load; tensile wood strain at rupture ($\varepsilon_{t,max}$), the maximum strain as viably measured by a strain gauge on the extreme tension wood fibre at midspan; and compressive wood strain ($\varepsilon_{c,max}$), which is the strain value corresponding to at P_{max} as measured by a strain gauge on the extreme compression wood fibre at midspan.

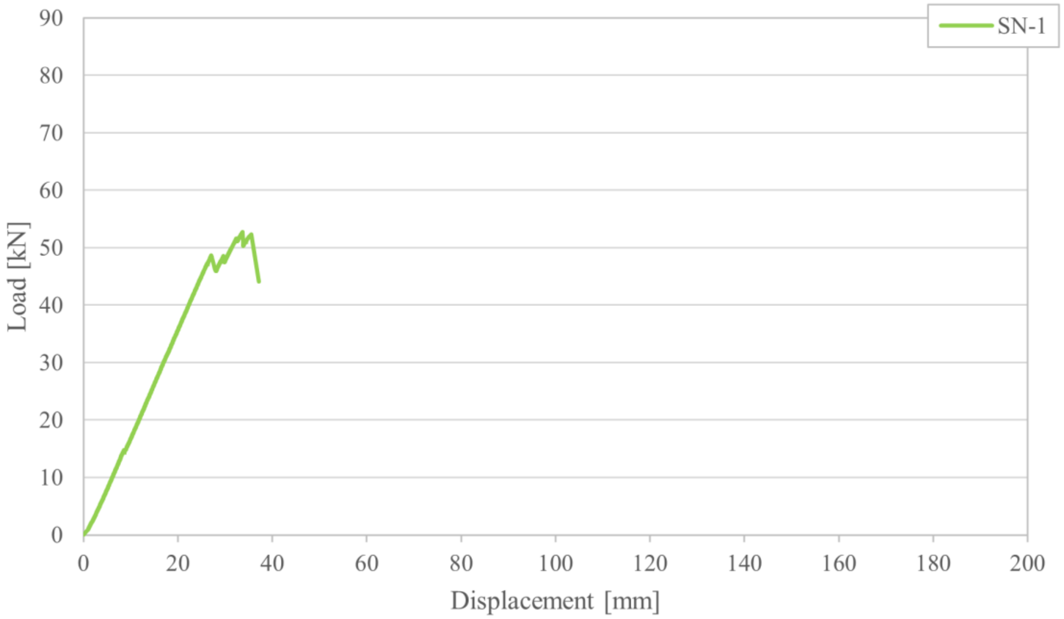

(a) Sawn timber

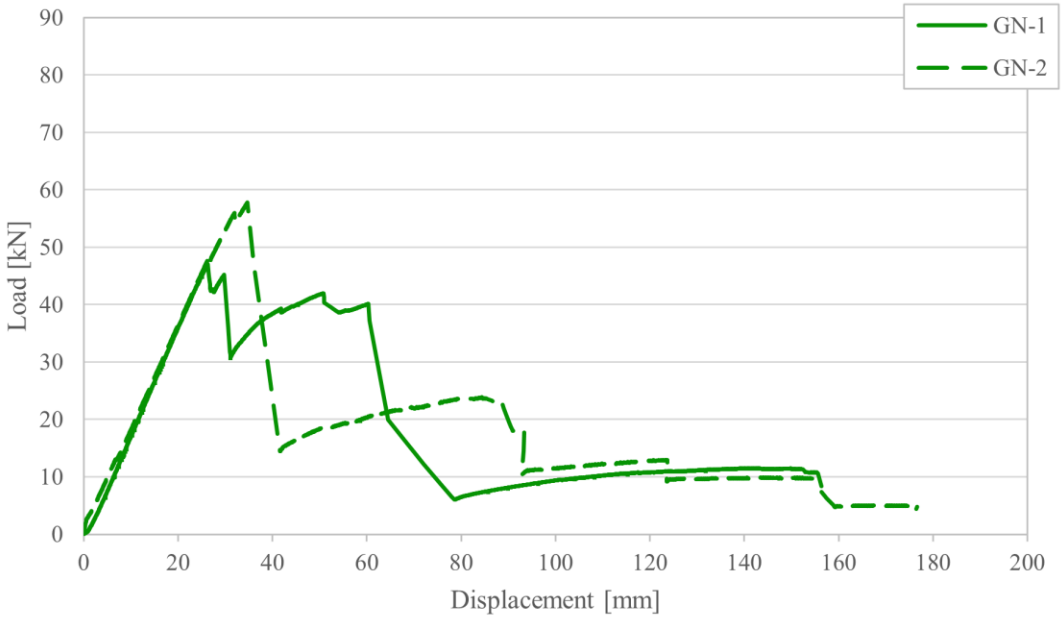

(b) Glulam

Figure 4.12: Resistance curves of unreinforced beams

Table 4.5: Results of 4-point Bending Tests on Unreinforced Beams

ID #	P_{max} a) [kN]	$\Delta_{P,max}$ b) [mm]	MOR c) [MPa]	K_w d) [N/mm]	$\varepsilon_{t,max}$ e) $\times 10^3$ [mm/mm]	$\varepsilon_{c,max}$ f) $\times 10^3$ [mm/mm]
SN-1	52.7	31.5	38.9	1773	3.99	3.00
GN-1	47.1	24.4	44.2	1849	2.82	4.30
GN-2	57.8	33.3	54.3	1853	4.86	5.70
Average	**52.5**	**28.8**	**49.3**	**1851**	**3.84**	**5.00**

a) Maximum load resistance
b) Displacement at maximum applied load
c) Modulus of rupture
d) Bending stiffness
e) Tensile strain at rupture
f) Compressive strain at maximum load

4.3.3 Specimens reinforced with GFRP fabric-laminates

The addition of GFRP fabric-laminate as external reinforcement caused a noticeable shift in the flexural behaviour of the beams. In the sawn timber specimens, the wood on the tension face was observed to fail first, as shown in Figure 4.13. In all cases, all specimens in this group demonstrated a sudden failure across the entire depth of the sawn timber specimens. This observation is in line with larger loads being applied and sustained through the added reinforcement.

(a) Wood-FRP debonding (b) Wood rupture

Figure 4.13: Representative failure of FRP-fabric-reinforced sawn timber specimens

Figure 4.14 shows specimen SF-1 immediately before and after failure where FRP debonding at failure was observed (*i.e.*, separation of the FRP layer due to the wood pushing outward). In Figure

4.14c, the close-up of the failed beam shows the initial tensile failure in the wood, which originated at a knot on the tension face at the approximate midspan. The reduced cross-section due to the pre-existing longitudinal splits at mid-depth formed a failure plane where the beam "popped" open as the FRP debonded.

(a) Maximum applied load

(b) Initial failure, FRP debonding

(c) Crack origin detail (back view, mirrored)

Figure 4.14: Failure progression of SF-1

Figure 4.15 shows specimen SF-2 immediately before and after failure, as well as a detailed view of the failed beam. The lower portion of the beam depth was mostly intact, but failure along the pre-existing longitudinal splits at mid-depth governed the failure mode. The failure propagated throughout the beam until it reached the compressive side. The GFRP reinforcement was not observed to debond; rather, the initial failure of the wood occurred outside the provided reinforcement and propagated throughout the sawn timber section without GFRP debonding.

(a) Maximum applied load

(b) Initial failure

(c) Crack origin detail (back view, mirrored)

Figure 4.15: Failure progression of SF-2

The observed failure modes for the glulam specimens GF-1 and GF-2 are shown in Figure 4.16 and Figure 4.17, respectively. The initial failure was observed to occur in the wood on the tensile face, with the failure across the depth occurring immediately after the initial failure.

In general, the two fabric-reinforced glulam beams performed comparably to each other. Similarly to their control counterparts, failure in both reinforced glulam beams followed the path of least resistance and propagated throughout the specimen, albeit occurring altogether in one instant at the maximum load without any significant sustained post-peak resistance. The initial failure of the wood occurred at the reinforcement termination point, thus no debonding of the GFRP and wood was observed.

(a) Peak loading

(b) Initial failure

(c) Crack detail (front view)

Figure 4.16: Failure progression of GF-1

(a) Peak loading

(b) Initial failure

(c) Crack detail (front view)

Figure 4.17: Failure progression of GF-2

The load-displacement curves of the four FRP fabric-reinforced beams are shown in Figure 4.18. Key values are summarized in Table 4.6 below. Values of interest presented are the peak or maximum load resistance (P_{max}); its corresponding midspan displacement ($\Delta_{P,max}$) as measured by the string pot; the bending stiffness (K), derived as the slope of the initial rising arm in the load-displacement plot of the unreinforced beam corresponding with the first 10–40% of the maximum load; tensile wood strain at rupture ($\varepsilon_{t,max}$), the maximum strain as viably measured by a strain gauge on the extreme tension wood fibre at midspan; compressive wood strain ($\varepsilon_{c,max}$), the strain value corresponding to at P_{max} as measured by a strain gauge on the extreme compression wood fibre at midspan; and the tensile FRP strain at rupture ($\varepsilon_{r,max}$).

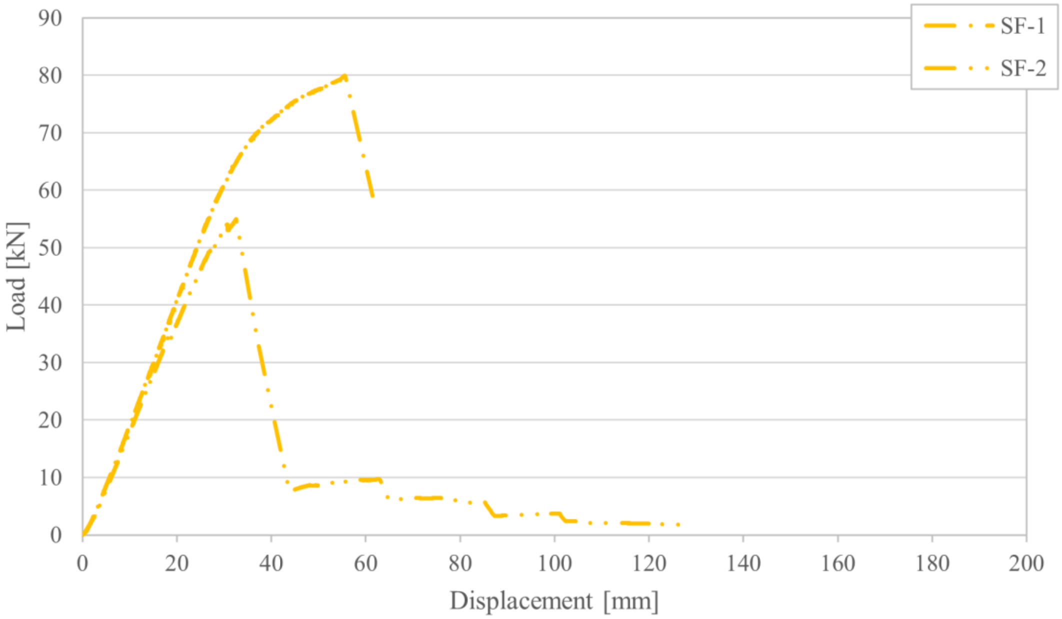

(a) Sawn timber

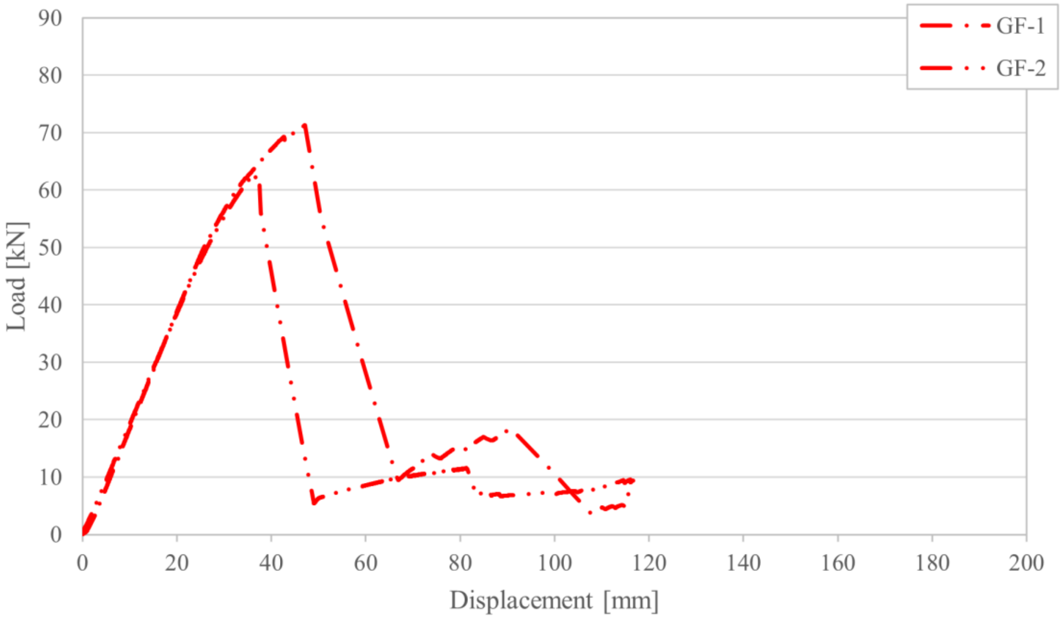

(b) Glulam

Figure 4.18: Resistance curves of beams reinforced with GFRP fabric

Table 4.6: Results of 4-point Bending Tests on Beams Reinforced with GFRP Fabric

ID	**P_{max} a)**	**$\Delta_{P,max}$ b)**	**K_w c)**	**K_r d)**	**$\varepsilon_{t,max}$ e) $\times 10^3$**	**$\varepsilon_{c,max}$ f) $\times 10^3$**	**$\varepsilon_{r,max}$ g) $\times 10^3$**
#	**[kN]**	**[mm]**	**[N/mm]**	**[N/mm]**	**[mm/mm]**	**[mm/mm]**	**[mm/mm]**
SF-1	80.0	55.7	1788	2014	6.26	4.78	8.92
SF-2	55.0	32.6	1641	1848	3.89	5.22	2.44
Average	**67.5**	**44.1**	**1715**	**1931**	**5.08**	**5.00**	**5.68**
GF-1	71.3	47.1	1799	1977	5.64	4.17	6.85
GF-2	62.7	37.3	1666	1901	5.02	4.53	5.59
Average	**67.0**	**42.2**	**1723**	**1939**	**5.33**	**4.35**	**6.22**

a) Maximum load resistance

b) Displacement at maximum applied load

c) Bending stiffness of pre-loaded wood

d) Bending stiffness of the reinforced beam

e) Wood tensile strain at failure

f) Compressive strain at maximum load

g) FRP tensile strain at failure

4.3.4 Specimens reinforced with GFRP bars

The addition of GFRP bars as tension reinforcement caused a noticeable shift in the flexural behaviour of the beams. In the sawn timber beams, failure was observed to first occur in the wood on the tension face (*i.e.*, below the bars) followed by the epoxy cracking and shattering. Figure 4.19 and Figure 4.20 show the failure progression of the two FRP rebar-reinforced sawn timber beams, SB-1 and SB-2, respectively. In both instances, the addition of GFRP bars contributed to the damage being localized across the cross-section depth rather than propagating throughout the beam. In both cases, the failure developed around knots (Figure 4.19e and Figure 4.20e).

Figure 4.21 and Figure 4.22 show the failure progression of the two FRP rebar-reinforced glulam beams, GB-1 and GB-2, respectively. The initial failure was observed to occur in the outermost wood laminate, followed by failure of the resin. The failure path in the glulam specimens was observed to follow the path of least resistance and propagated throughout the section. Compared to the other glulam beams with exposed wood at the extreme tension face, GB-1 did not have any large defects in the bottom layer, only small knots and one line of finger joints. Instead of large defects, the tensile rupture originated from this finger joint, as shown in Figure 4.23.

(a) Start of test

(b) Initial wood failure; string pot disconnected

(c) FRP resin failure

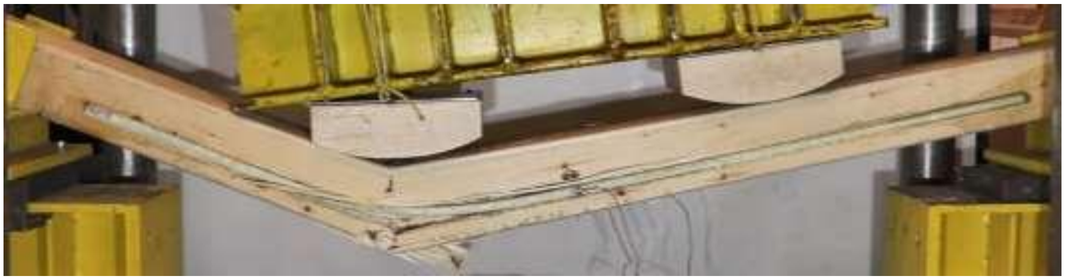

(d) Ultimate failure

(e) Crack detail (bottom view)

Figure 4.19: Failure progression of SB-1

(a) Start of test

(b) Initial wood failure

(c) FRP resin failure

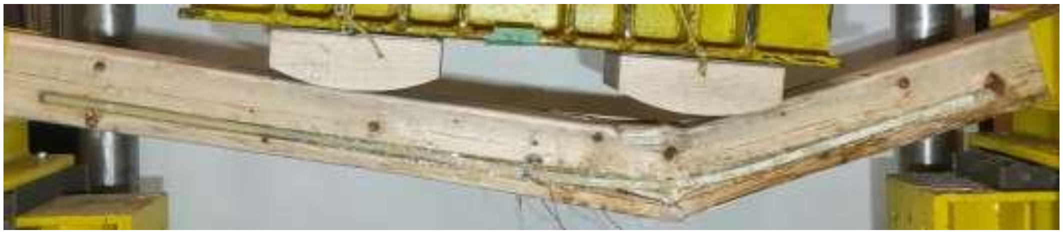

(d) Ultimate failure

(e) Crack and slip detail (front view)

Figure 4.20: Failure progression of SB-2

(a) Start of test

(b) Initial failure

(c) FRP resin failure

(d) Ultimate failure

(e) Crack detail (front view)

Figure 4.21: Failure progression of GB-1

(a) Start of test

(b) Initial failure

(c) FRP resin failure

(d) Ultimate failure

(e) Crack detail (front view)

Figure 4.22: Failure progression of GB-2

Figure 4.23: Ruptured finger joint in GB-1

The load-displacement curves for all four GFRP rebar-reinforced beams are shown in Figure 4.24, in which the displacement axis represents the string pot reading at midspan. Key values are summarized in Table 4.7, including the peak or maximum load resistance (P_{max}); its corresponding midspan displacement ($\Delta_{P,max}$) as measured by the string pot; the bending stiffness (K), derived as the slope of the initial rising arm in the load-displacement plot of the unreinforced beam corresponding with the first 10–40% of the maximum load; tensile wood strain at rupture ($\varepsilon_{t,max}$), the maximum strain as viably measured by a strain gauge on the extreme tension wood fibre at midspan; compressive wood strain ($\varepsilon_{c,max}$), the strain value corresponding to at P_{max} as measured by a strain gauge on the extreme compression wood fibre at midspan; and the tensile FRP strain at rupture obtained from a strain gauge at mid-height of the FRP bar at midspan ($\varepsilon_{r,max}$).

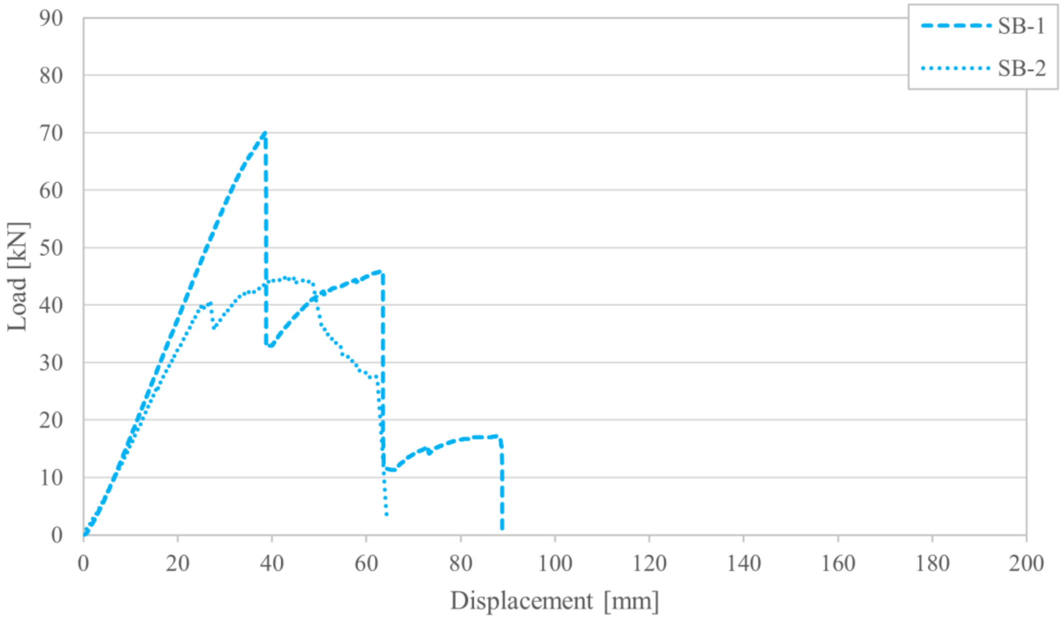

(a) Sawn timber

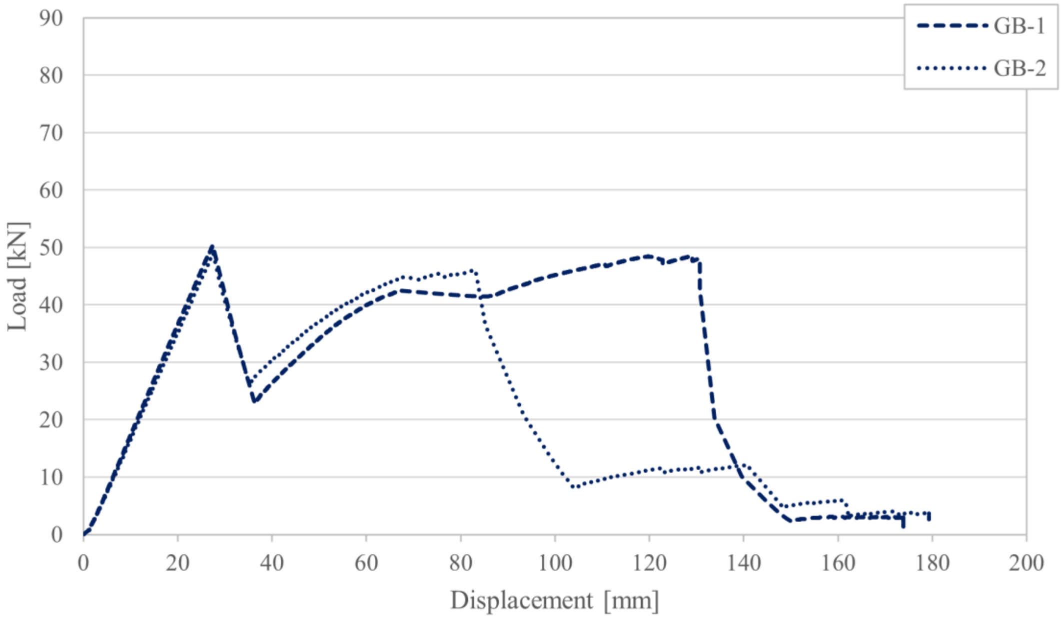

(b) Glulam

Figure 4.24: Resistance curves of beams reinforced with GFRP bars

Table 4.7: Results of 4-point Bending Tests on Beams Reinforced with GFRP Bars

ID #	P_{max} a) [kN]	$\Delta_{P,max}$ b) [mm]	K_w c) [N/mm]	K_r c) [N/mm]	$\varepsilon_{t,max}$ e) $\times 10^3$ [mm/mm]	$\varepsilon_{c,max}$ f) $\times 10^3$ [mm/mm]	$\varepsilon_{r,max}$ g) $\times 10^3$ [mm/mm]
SB-1	70.1	38.6	1666	1765	5.05	4.76	5.76
SB-2	45.1	43.4	1461	1548	2.53	4.27	4.79
Average	**57.6**	**41.0**	**1564**	**1656**	**3.79**	**4.52**	**5.27**
GB-1	50.4	27.4	1706	1873	4.13	3.29	2.39
GB-2	49.0	27.5	1758	1794	3.49	6.46	7.98
Average	**49.7**	**27.5**	**1732**	**1834**	**3.81**	**4.88**	**5.18**

a) Maximum load resistance
b) Displacement at maximum applied load
c) Bending stiffness of pre-loaded wood
d) Bending stiffness of the reinforced beam
e) Wood tensile strain at failure
f) Compressive strain at maximum load
g) FRP tensile strain at failure

It is to be noted that the string pot was disconnected from SB-1 upon the impulse of initial failure, as seen in Figure 4.19b. Consequently, the midspan displacement data beyond peak loading in this test was estimated using the crosshead displacement based on an assumption that the crosshead would remain in line with the string pot over the test duration (*i.e.*, failure is fully symmetrical). Because the crosshead is restricted to move along only the vertical axis whereas the string pot measures the three-dimensional displacement between two anchored points, the error between these two measurements is proportional to the magnitude of displacement and the longitudinal distance between the string pot's anchor point and the point of failure (Figure 4.25). In both SB-1 and SB-2, failure occurred under one of the loading blocks, thus the displacement ratios were assumed to be similar. A variable adjustment factor was therefore derived from the SB-2 test data by using the crosshead-to-string pot displacement ratio, starting from the point of initial failure where this ratio was equal between the two tests. At peak loading, the string pot displacement reading was 0.5% greater than the crosshead displacement; this error would increase to 19.4% by the end of the test.

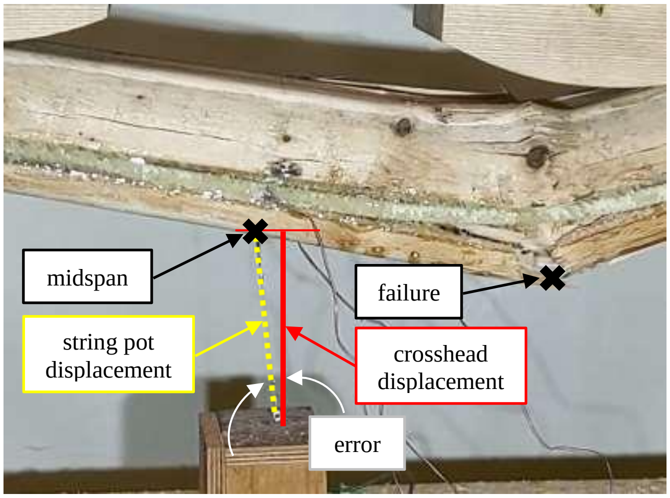

Figure 4.25: Adjustment method used for measuring large displacements beyond initial failure

Chapter 5

Discussion

5.1 General

This chapter discusses the observations and results presented in the previous chapter. Methods for determining the flexural strength of FRP-reinforced wood beams are investigated with the current test data.

5.2 Effects of GFRP Reinforcement Types on the Flexural Behaviour of Sawn Timber and Glulam Beams

5.2.1 Overview

The flexural behaviour of FRP-reinforced wood beams can be noticeably impacted by the types of reinforcement materials used in their composition and the form of reinforcement itself. This section discusses the roles in which solid-sawn timber, glulam, GFRP fabric-laminates, and GFRP bars each led to the beam-test observations found in the previous chapter. It is to be noted that due to small sample sizes, particularly in each specific category, the results and observations derived from the beam tests in the present study can only comment on the overall effects between sets. Further statistical significance may be achieved by replicating each test with enough specimens to attain the desired confidence interval and to confirm the observed trends.

5.2.2 Control specimens

Despite symmetrical loading, bending failure in the unreinforced sawn timber beam did not always originate at midspan, as shown in Figure 5.1a. Under ideal conditions, beams of uniform cross-sections subjected to symmetrical four-point loading experience maximum and pure bending (*i.e.,* without the presence of shear) in the longitudinal section between the two applied loads. However, the inherent variability of wood results in stress concentrations which may cause premature failure; members containing more defects have more potential locations at which failure-may occur. Consequently, flexural failure is more likely to originate from such defects and not necessarily at midspan, as was the case in specimen SN-1.

The unreinforced glulam specimens behaved similarly to their sawn timber counterparts only until cracking propagated through its first ply of wood. With glulam being composed of once-separate planks of lumber, the glued interface between the plies appeared to function as a “reset” point for crack propagation, failing sequentially one by one under flexure, as shown in Figure 5.1b. The arrangement of glulam provides several improvements over solid timber: (1) whereas defects present in solid timber can only be visually observed on the outer surface and not inside, significant defects on any ply of glulam can be removed from production to result in a more reliably “uniform” interior; (2) the glued interfaces between each ply provide a lamination effect; and (3) discontinuity between the wood grains arrest crack propagation such that they do not progress straight through the member.

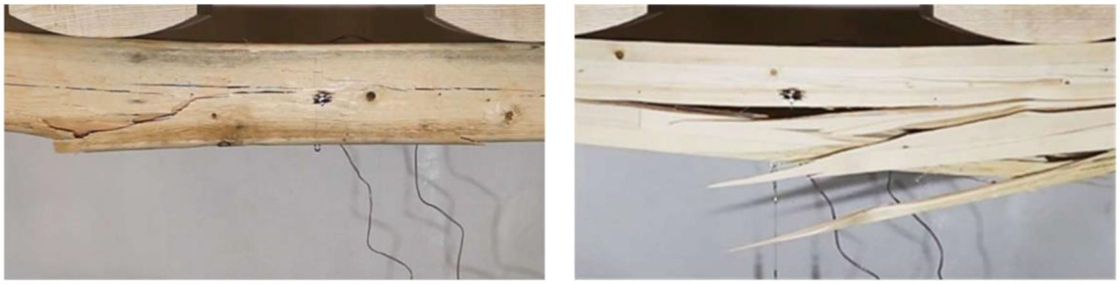

(a) Sawn timber (b) Glulam

Figure 5.1: Ultimate failure in control specimens

Figure 5.2 compares the load-displacement behaviour of the control specimens. Average key values—peak load, corresponding displacement, stiffness, and modulus of rupture (MOR)—are compared in Table 5.1. The raw data shows that the three beams had similar bending stiffnesses and resisted comparable peak loads; however, it should be noted that because the sawn timber beams (140 mm × 140 mm) are slightly wider than the glulam beams (110 mm × 140 mm), the sawn timber beams have a lower MOR than that of the glulam beams. In addition, glulam can be expected to have a higher MOR than a sawn timber beam of an equal dimensions due to its nature as an engineered wood product; despite both types being of the same species group, the selectivity of each individual layer of glulam results in greater rigidity. The combined effects of these factors can be observed in Table 5.1.

While all control beams failed in flexure with the failure originating on the tension side, noticeable differences in the overall behaviour were observed: whereas the solid lumber beam failed shortly after peak loading, both glulam beams exhibited some level of post-peak behaviour or residual capacity after the initial failure. Furthermore, secondary peaks can be seen in the glulam plots, each corresponding with the tensile failure of a wood layer, compensated by the next subsequent intact layer.

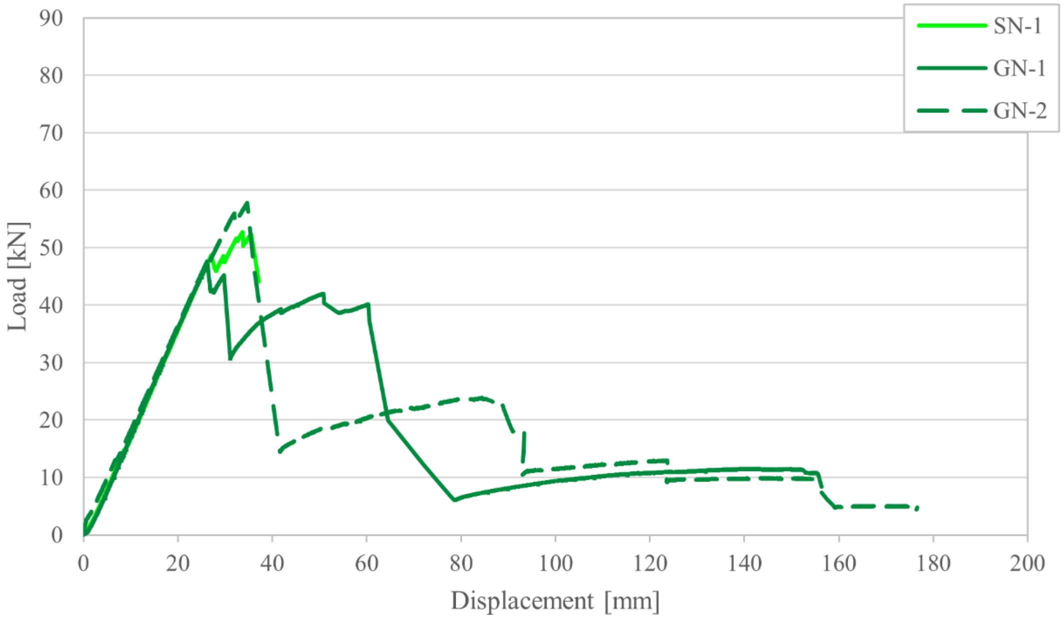

Figure 5.2: Comparison of resistance curves of unreinforced beams

Table 5.1: Effect of Wood Type on Unreinforced Beams

Beam Group(s)	**P_{max} a) [kN]**	**$\Delta_{P,max}$ b) [mm]**	**MOR c) [MPa]**	**K_w d) [N/mm]**	**$\varepsilon_{t,max}$ e) $\times 10^{-3}$**	**$\varepsilon_{c,max}$ f) $\times 10^{-3}$**
SN	52.7	31.5	38.9	1773	3.99	3.00
GN	52.5	28.8	49.3	1851	3.84	5.00

a) Average maximum load resistance(s)
b) Average displacement(s) at maximum load
c) Average modulus (or moduli) of rupture
d) Average bending stiffness(es)
e) Average tensile strain at rupture
f) Average compressive strain at maximum load

5.2.3 Specimens reinforced with GFRP fabric-laminates

The addition of GFRP fabric-laminates resulted in strength and stiffness enhancements among both sawn timber and glulam beams. This effect can be seen in Figure 5.3, which compares the load-displacement behaviour of these reinforced beams with their control counterparts. The ratios presented in Table 5.2 affirm substantial improvements to average peak load (28% increases), displacement at peak load (39-42%), and peak tensile strain (27-39%) when GFRP fabric-laminate reinforcement is added to either sawn timber or glulam. This reinforcement was not observed to improve the post-peak behaviour relative to the unreinforced specimens. This can be attributed to the wood failing in tension at the end of the provided reinforcement or—in one case, SF-1—pushing outward on the fabric, causing debonding and thus rendering the reinforcement ineffective following initial failure, as seen in Figure 5.4 and Appendix D.

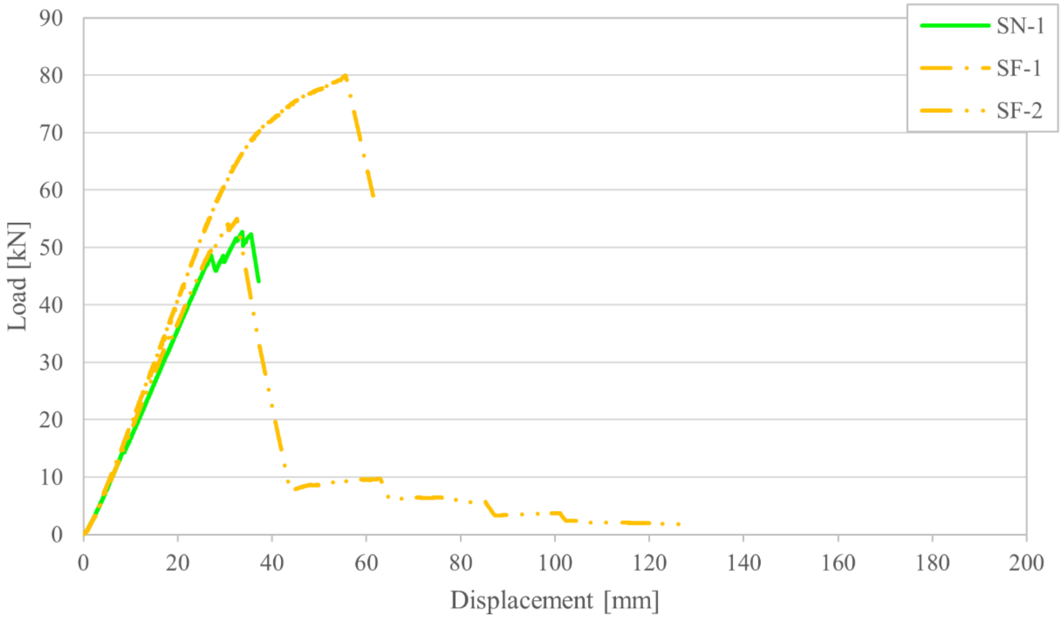

(a) Sawn timber

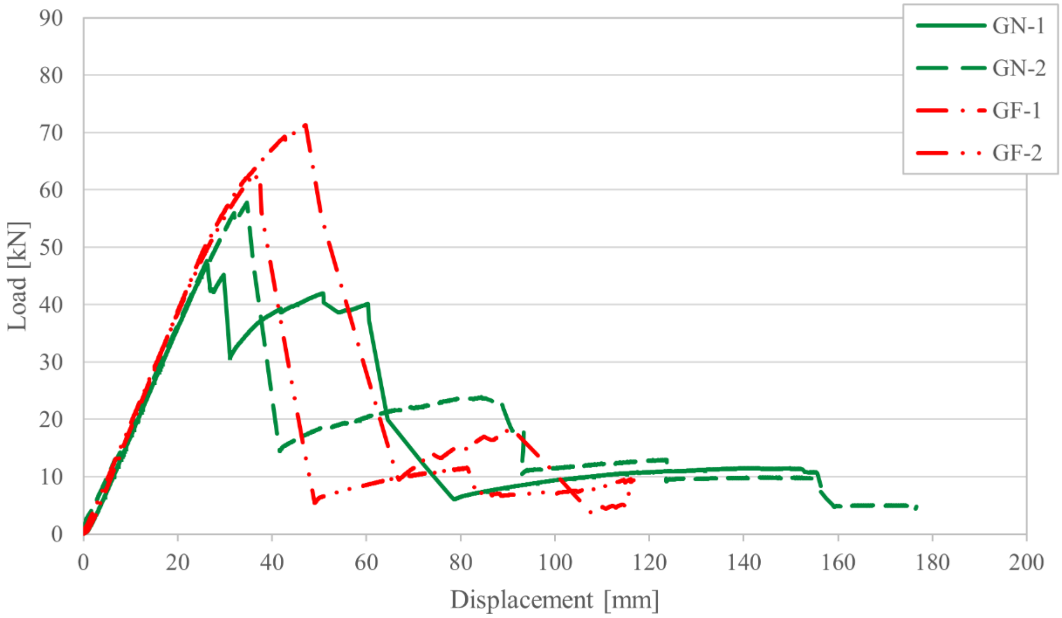

(b) Glulam

Figure 5.3: Behavioural comparison of beams with and without GFRP fabric

Table 5.2: Effect of Reinforcement with GFRP Fabric-Laminate

Beam Group(s)	**P_{max} a) [kN]**	**$\Delta_{P,max}$ b) [mm]**	**K_w c) [N/mm]**	**K_r d) [N/mm]**	**$\varepsilon_{t,max}$ e) $\times 10^{-3}$**	**$\varepsilon_{c,max}$ f) $\times 10^{-3}$**
SN	52.7	31.5	1773	–	3.99	3.00
SF	67.5	43.8	1715	1931	5.08	5.00
Ratio (F:N)	**1.28**	**1.39**	**0.97**	**1.09**	**1.27**	**1.67**
GN	52.5	28.8	1851	–	3.84	5.00
GF	67.0	41.0	1723	1939	5.33	4.35
Ratio (F:N)	**1.28**	**1.42**	**0.93**	**1.05**	**1.39**	**0.87**

a) Average maximum load resistance(s)

b) Average displacement(s) at maximum load

c) Average bending stiffness(es) of pre-loaded wood

d) Average bending stiffness(es) of reinforced beam

e) Average tensile strain(s) at failure

f) Average compressive strain(s) at maximum load

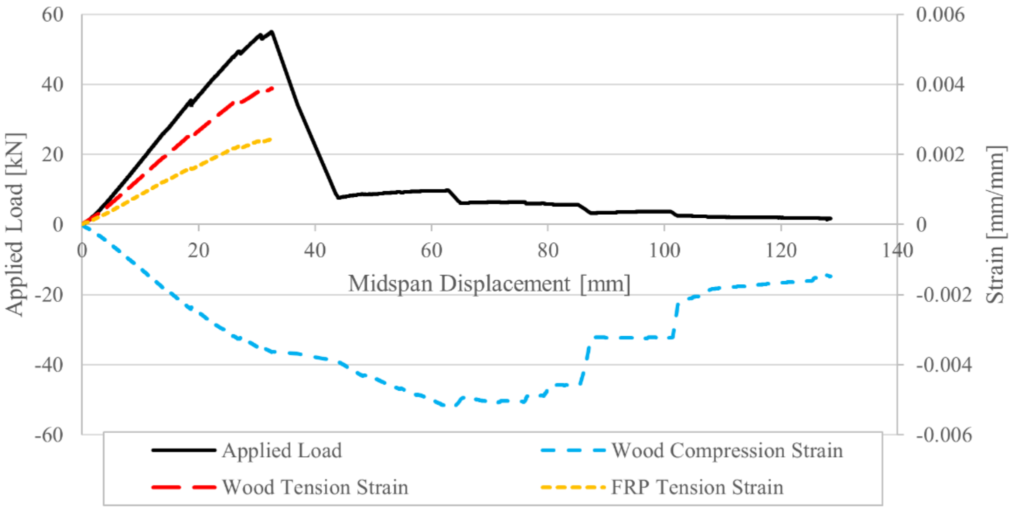

Figure 5.4: Simultaneous wood-FRP tension failure in SF-2

As seen in Figure 5.4 and similar figures in Appendix D, the maximum tensile strains in the wooden member and FRP fabric-laminate coincide with the maximum resistance, which abruptly decreases. Although the compression strain is observed to continue to increase, there is little post-peak resistance associated with the increased displacement after the initial failure.

The addition of GFRP as a fabric-laminate caused a noticeable shift in the flexural behaviour. In the control beams, failure occurred within the maximum moment region, whereas in all but one of the GFRP fabric-reinforced specimens, the initial failure occurred outside this region. The addition of GFRP fabric did contribute to the "bridging" of defects, as evidenced by wood tensile failure strain increases of 1.27 and 1.39 in the sawn timber and glulam beams, respectively. However, the failure mode observed in the current study (Figure 5.5a–c) differed significantly from that observed in Lacroix & Doudak (2018b) (Figure 5.5e) but was rather more akin to that observed in Vetter (2022) (Figure 5.5d) in that the initial failure occurred at the longitudinal interface at which the reinforcement terminated. This observation suggests that this reinforcement terminus plays an important role in the occurrence of failure. As established previously, variations found within the wood material (*e.g.*, knots) result in force concentrations which are responsible for many premature failures. If the tensile loads shift from the wood to the FRP, stress concentrations may be pushed along to develop at this point of discontinuity. In this sense, a retrofit scheme that applies fabric reinforcement beyond only the tension by also covering the sides in partial or even full confinement may reduce the effects of this perpendicular stress concentration (Lacroix et al., 2021; Vetter, 2022). The FRP fabric-laminate in the present study terminated 50 mm away from the edge of the supports, compared to 82.5 mm and 143 mm in Lacroix & Doudak (2018b) and Vetter (2022), respectively.

(a) FRP debonding in SF-1

(b) Failure at FRP termination point in SF-2

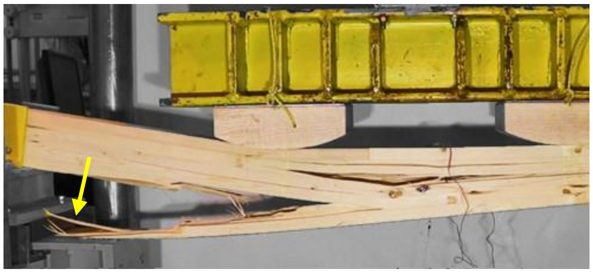

(c) Failure at FRP termination point in GF-2

(d) Failure at FRP termination point in Vetter (2022)

(e) FRP debonding in Lacroix & Doudak (2018b)

Figure 5.5: Representative failure modes

The strength contribution of FRP to reinforcing wood is more pronounced in specimens that are initially weaker than in stronger specimens; by bringing them close to clear-wood strength, FRP has a more pronounced effect on wood materials with more defects and variability. This increase in strength consistency is reflected in Figure 5.6, which compares the behaviour of reinforced glulam—which is of higher quality and hence fewer defects—with reinforced sawn timber. Lower overall variability in the glulam beams' behaviour can once again be observed in this figure.

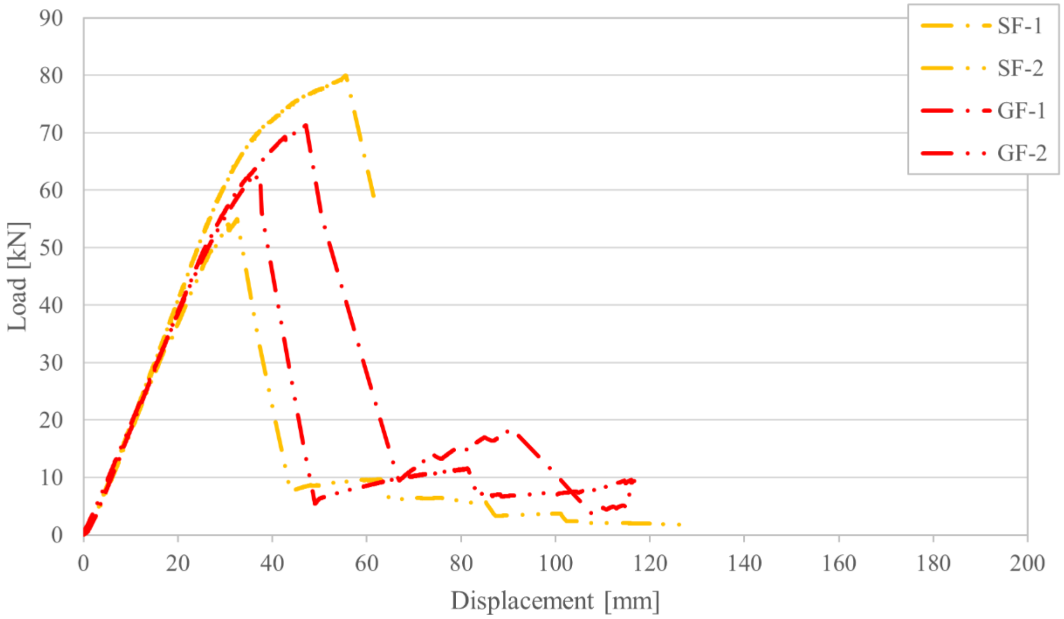

Figure 5.6: Behavioural comparison of beams reinforced with GFRP fabric-laminate

5.2.4 Specimens reinforced with GFRP bars

Failure in the GFRP bar-reinforced beams failed in a manner distinct from the previous categories. Initial failure originated in the wood cover in its unreinforced tension fibres, but the depth of crack propagation was arrested at the GFRP bars. The next component to fail would be the epoxy resin encasing and bonding the GFRP bars to the wood. The resin would shatter suddenly and explosively on each side, and shards remaining attached to the rebar allowed it to continue developing strength as part of the semi-composite beam. The consequence of this behaviour was the removal of much (but not all) of the load-transfer medium, as shown in the glulam specimen in Figure 5.7. What was left of the reinforcement continued to bridge defects in the beam, with a new path of least resistance resulting from the point at which the wood cover failed. Finally, cracks would continue to form and propagate continuously through the depth. In the sawn timber beams, shown in Figure 5.8, the cracks tended to develop locally, fully in line with the initial crack; in the glulam beams, as in Figure 5.7, cracks would often transfer along the glue lines, indicating weakness where the wood fibres were discontinuous. Meanwhile, wood fibres on the compression side wrinkled significantly as the reinforced tensile forces exceeded the forces in the compressed unreinforced wood.

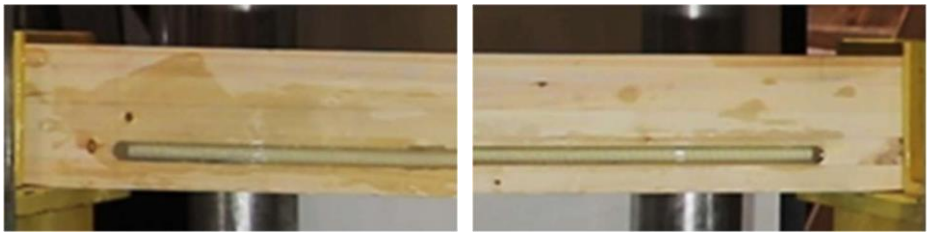

(a) Bar end positions at peak loading

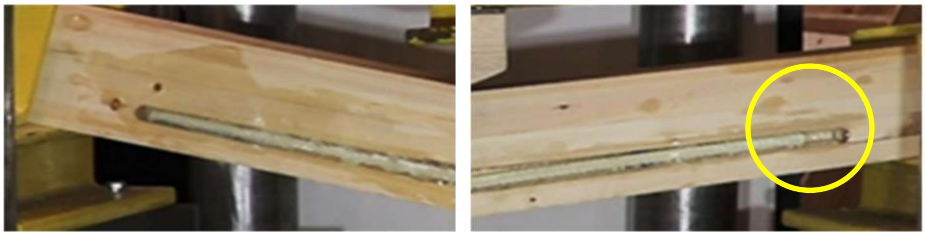

(b) Resin failure caused bar slippage at one end

(c) Little-to-no bonded resin at midspan

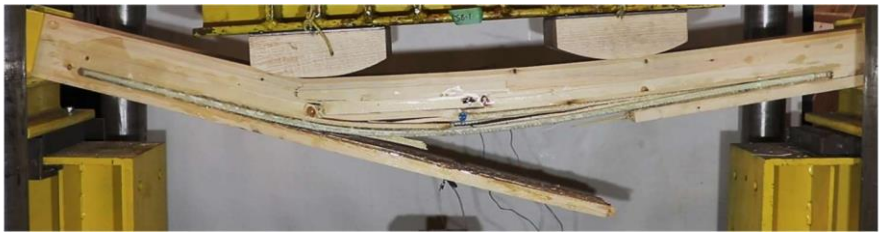

(d) Overall beam at ultimate failure

Figure 5.7: Resin failure in GB beam

(a) SB-1

(b) SB-2

Figure 5.8: Crack propagation in SB beams

Because the wood cover was unreinforced on the tension side, the reinforced beams demonstrated little difference on average—in terms of peak strength and stiffness—from the control sawn timber and glulam specimens. This behaviour can be observed in Figure 5.9, which compares the load-displacement behaviour of the GFRP bar-reinforced beams with their control counterparts. Furthermore, the explosive behaviour of the resin upon initial failure would need to be addressed in practical scenarios, particularly with few visible indicators of the cover's tensile failure. However, the GFRP bars contributed noticeably towards enhancing the post-peak performance and sustained deformation over the respective control beams. Figure 5.9a shows that the addition of reinforcing bars to sawn timber beams provided appreciable post-peak resistance where there initially was none. Figure 5.9b shows that, in addition to there being less overall variability in the glulam beams, the reinforcing bars added substantial load-carrying capacity to the post-peak resistance. The ratios presented in Table 5.3 highlight relatively unsubstantial changes in peak load resistance, stiffness, and peak tensile stress for the glulam, but the sawn timber beams observed, at maximum resistance, 24% and 51% increases in displacement and compressive strain, respectively, from that of the control specimens. The decision to mount the bars from the sides—rather than from the bottom—allowed the GFRP to rest upon the wood cover rather than a volume of only epoxy. Furthermore, given that CSA S6 does not permit mounting GFRP rebar on the bare exterior surface of wood beams, but rather, requires bars to be installed with some cover of unreinforced wood, it was expected that the initial wood tensile failure would be comparable to that of the control section; increasing the depth of wood cover—which implies increasing the effective area of wood above the reinforcement—would increase the overall capacity, ergo passive reinforcement with bars may not be the optimal solution to improve stiffness for serviceability.

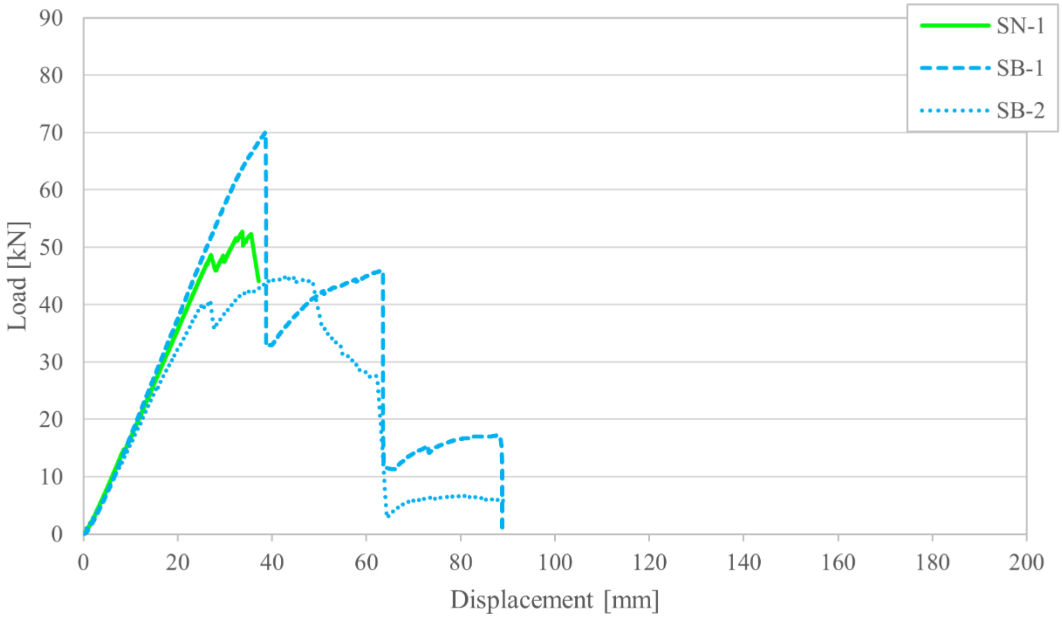

(a) Sawn timber

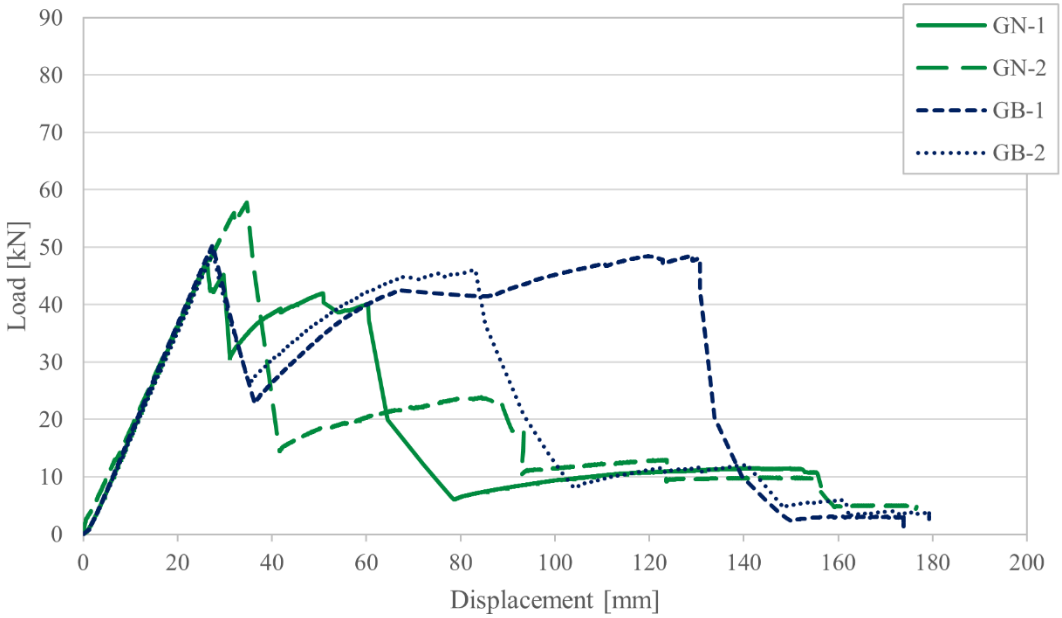

(b) Glulam

Figure 5.9: Behavioural comparison of beams with and without GFRP bars

Table 5.3: Effect of Reinforcement with GFRP Bars

Beam Group(s)	**P_{max} a) [kN]**	**$\Delta_{P,max}$ b) [mm]**	**K_w c) [N/mm]**	**K_r d) [N/mm]**	**$\varepsilon_{t,max}$ e) $\times 10^{-3}$**	**$\varepsilon_{c,max}$ f) $\times 10^{-3}$**
SN	52.7	31.5	1773	–	3.99	3.00
SB	57.6	39.1	1564	1656	3.79	4.52
Ratio (B:N)	**1.09**	**1.24**	**0.88**	**0.93**	**0.95**	**1.51**
GN	52.5	28.8	1851	–	3.84	5.00
GB	49.7	25.4	1732	1834	3.81	4.88
Ratio (B:N)	**0.95**	**0.88**	**0.94**	**0.99**	**0.99**	**0.97**

a) Average maximum load resistance(s)
b) Average displacement(s) at maximum load
c) Average bending stiffness(es) of pre-loaded wood
d) Average bending stiffness(es) of reinforced beam
e) Average tensile strain(s) at failure
f) Average compressive strain(s) at maximum load

Figure 5.10 shows that the bar reinforcement in sawn timber and glulam beams resulted in comparable increases in peak strength resistance and bending stiffness for the respective beam material. The caveat is that these results were only comparable in their averages, particularly with only two samples for each category: by inspection of Figure 5.10, the two bar-reinforced glulam beams had similar magnitudes of both peak and secondary peak load resistance, however peak loading in SB-2 was 9% lower than the GB average, whereas peak loading in SB-1 was 41% greater than the GB average. Figure 5.8 revealed that the wood grain structure was instrumental to this discrepancy: SB-1 was visibly clear in the upper portion of the beam above the point of initial failure, whereas SB-2 had a large knot directly above the point of its initial failure. Because crack propagation was linear and continuous from the extreme tension fibre, the chance that SB-1 was clear above this initial failure point contributed to its much greater peak load resistance.

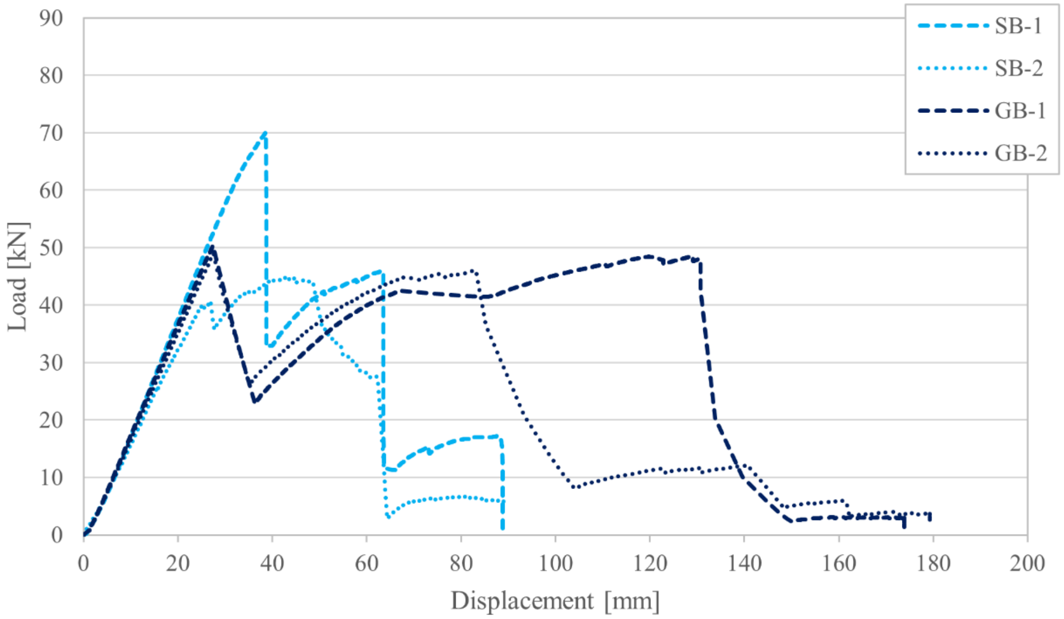

Figure 5.10: Behavioural comparison of beams reinforced with GFRP bars

5.2.5 Effects of GFRP reinforcement type

A side-by-side comparison of ultimate failure with the two different forms of GFRP reinforcement is shown in Figure 5.11 for the sawn timber beams and in Figure 5.12 for the glulam beams. These figures reveal patterns of how reinforcement types affect flexural behaviour and failure mode despite wood composition (*i.e.*, sawn timber or glulam). As with the control beams, wood failure almost always failed from high local stresses developed around knots or other defects. Adequate bonding with GFRP temporarily bridged these defects until this bond itself was compromised. Beams reinforced with GFRP fabric-laminate failed abruptly but resisted generally greater loads; conversely, beams reinforced with GFRP bars added comparatively little-to-no strength but contributed greatly to overall deformation. The latter is attributed to the remaining undamaged wood section bearing on the GFRP bars, which had superior strength given that no bars ruptured at large displacements.

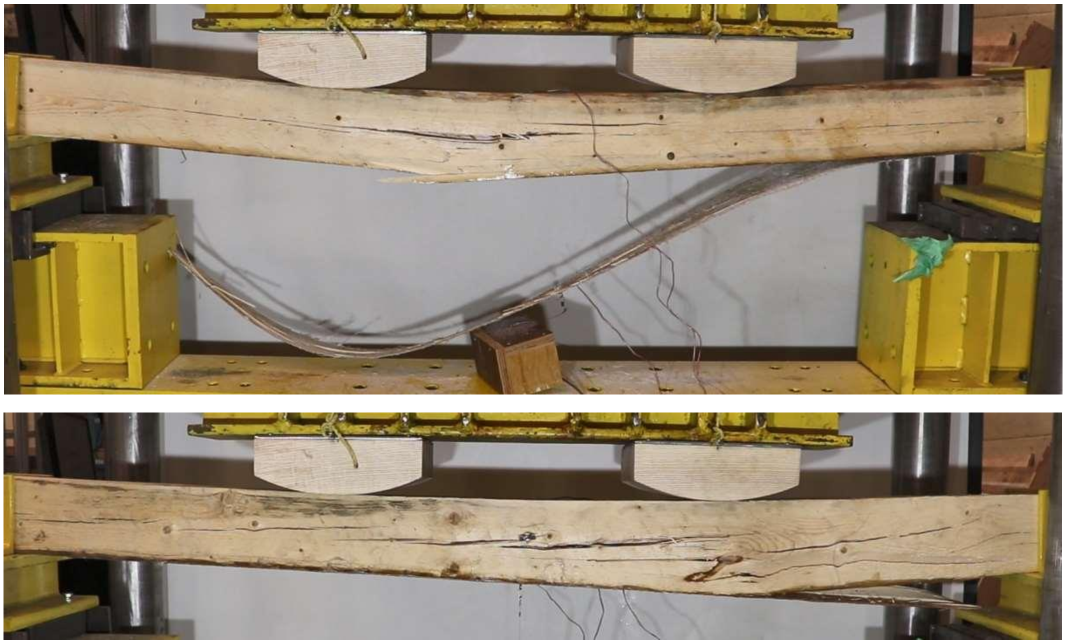

(a) FRP fabric-laminates, SF-1 (top) and -2 (bottom)

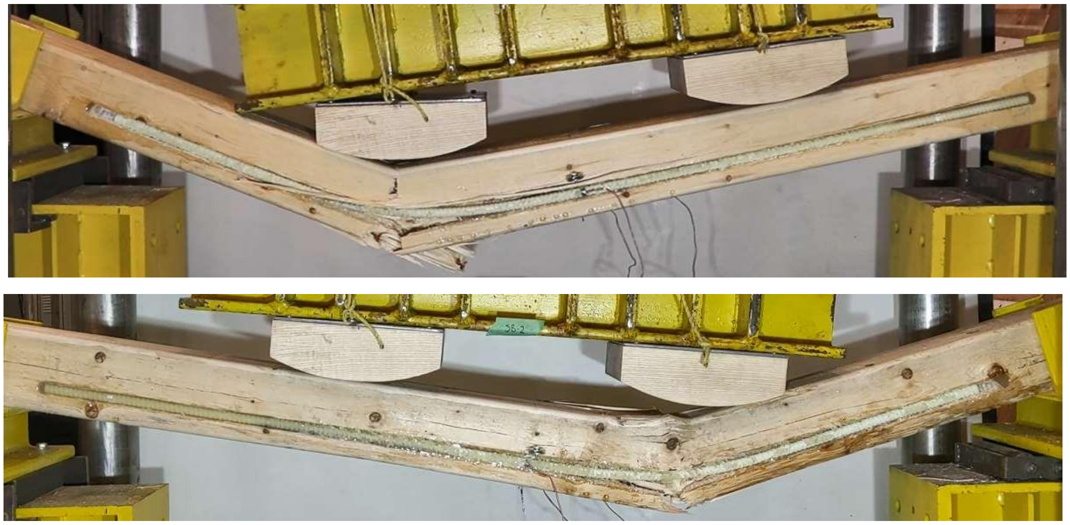

(b) FRP bars, SB-1 (top) and -2 (bottom)

Figure 5.11: Failure in reinforced sawn timber beams

(a) FRP fabric-laminate, GF-1 (top) and -2 (bottom)

(b) FRP bars, SB-1 (top) and -2 (bottom)

Figure 5.12: Failure in reinforced glulam beams

The GFRP fabric-laminate reinforcement brought substantial behavioural improvements over the control counterparts. On the other hand, the GFRP bar reinforcement was comparatively similar to that of the control counterparts in terms of peak strength due to the unreinforced cover, causing the damage propagation to remain more localized. Where the bar-reinforced specimens stood out was the greatly enhanced, sustained post-peak performance of each member, as shown in Figure 5.13 (*e.g.*, GF-1 peaks at 71 kN then loses most of its strength, whereas GB-1 peaks at 50 kN, but continues to sustain more than half its peak capacity until its midspan displaces by 130 mm). A contributor to this phenomenon is that much of the tensile wood strain was shifted to be carried by the FRP rebar upon failure, as seen in Figure 5.14 and similar figures in Appendix D. The overall beams were then able to re-develop load resistance up to 60% and 95% of the peak load in the sawn timber and glulam beams, respectively.

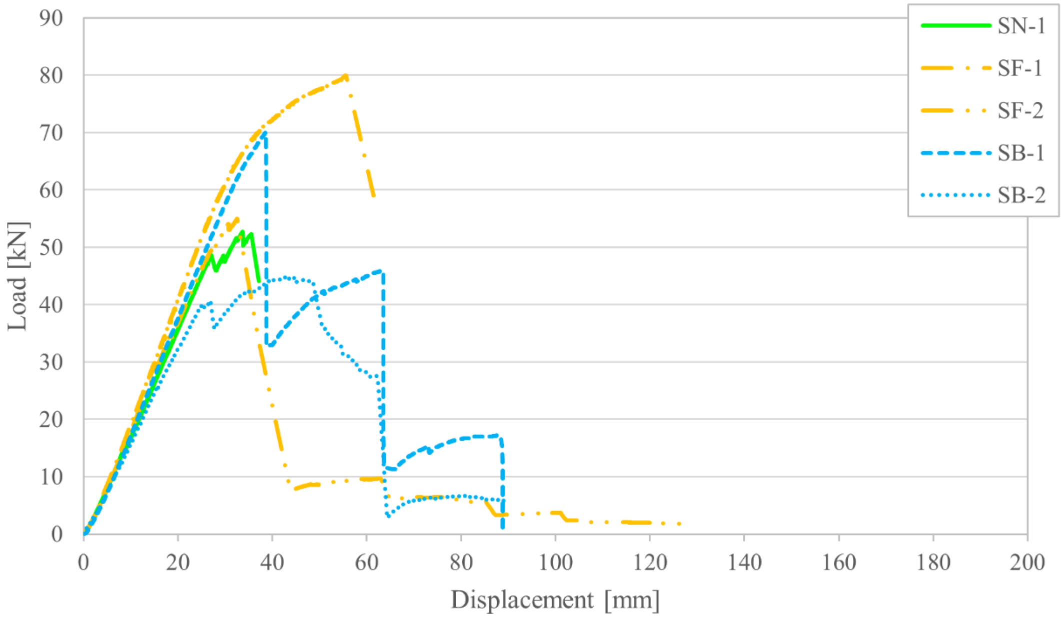

(a) Sawn timber

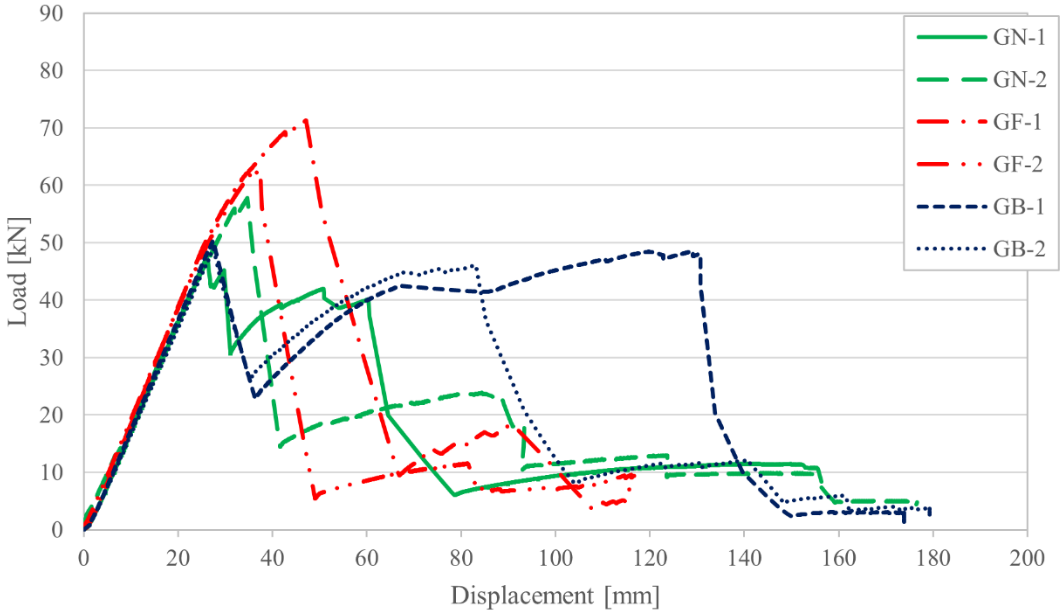

(b) Glulam

Figure 5.13: Behavioural comparison of GFRP reinforcement methods

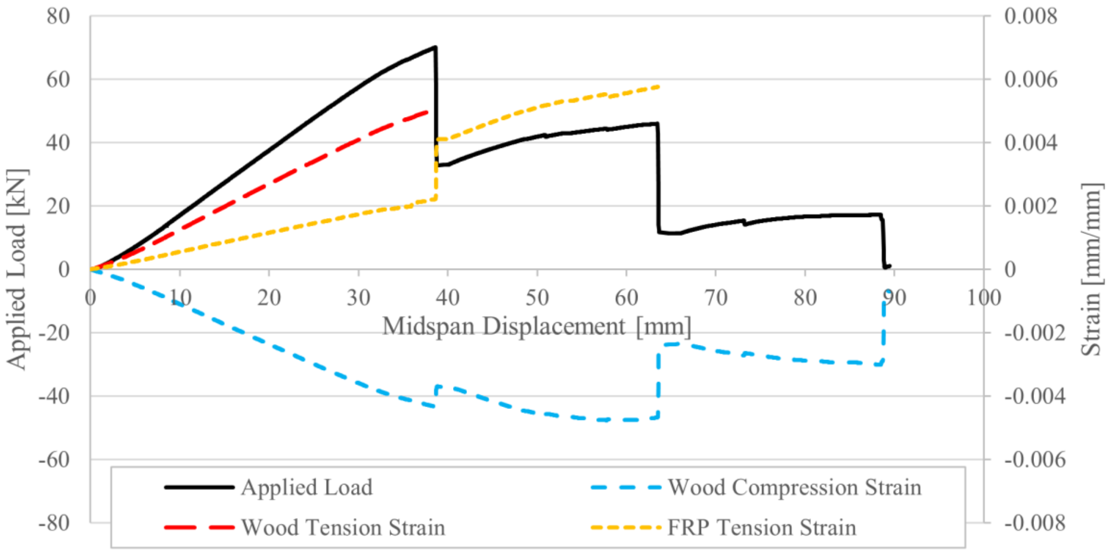

Figure 5.14: Tension strain takeover behaviour in SB-1

Table 5.4 provides a direct comparison of selected data between the reinforcement types for both types of beams. The effect of reinforcement type is most visible in the glulam beams, whereupon GFRP fabric-laminate resulted in notably greater peak load resistance, displacement, and tensile strains than that of the GFRP bar reinforcement. This pattern of gains was also present in the sawn timber beams, particularly in terms of wood tensile strain, albeit less sizeably than that of the glulam beams. A logical conclusion can be drawn that GFRP fabric-laminate reinforcement generally outperforms GFRP bar reinforcement when used in passive reinforcement. Furthermore, the GFRP bars were not mounted directly on the tensile surface of the wood, but rather, with clearance above the tensile surface, effectively contributing to a smaller effective wood section; with the reinforcement placed higher towards the neutral axis, the tension strains experienced by the GFRP bars were unable to develop fully before the exterior wood reached tensile yielding. Future studies should therefore investigate the effects of using side-mounted versus near-surface-mounted reinforcement with GFRP bars. Despite these disadvantages, side-mounted GFRP bars contributed to eliminating any delamination or debonding.

Table 5.4: Effect of GFRP Reinforcement Type

Beam Group(s)	P_{max}a) [kN]	$\Delta_{P,max}$b) [mm]	K_wc) [N/mm]	K_rd) [N/mm]	$\varepsilon_{t,max}$d) $\times 10^{-3}$	$\varepsilon_{c,max}$e) $\times 10^{-3}$	$\varepsilon_{r,max}$f) $\times 10^{-3}$
SF	67.5	44.1	1715	1931	5.08	5.00	5.68
SB	57.6	41.0	1564	1656	3.79	4.52	5.27
Ratio (B:F)	**0.85**	**0.89**	**0.91**	**0.86**	**0.75**	**0.90**	**0.93**
GF	67.0	42.2	1723	1939	5.33	4.35	6.22
GB	49.7	27.5	1732	1834	3.81	4.88	5.18
Ratio (B:F)	**0.74**	**0.62**	**1.01**	**0.95**	**0.71**	**1.12**	**0.83**

a) Average maximum load resistance(s)
b) Average displacement(s) at maximum load
c) Average bending stiffness(es)
d) Average tensile strain(s) at failure
e) Average compressive strain(s) at maximum load
f) Average FRP tensile strain(s) at failure

5.3 Predicting Flexural Behaviour

5.3.1 Overview

Three methods for predicting the flexural resistance in FRP-reinforced timber beams were applied and compared to their corresponding beam test results. In the transformed-area method, the predictions are based on the materials' moduli of elasticity—obtained from coupon tests—and the physical geometry only. The force-equilibrium method and its modified variant presented here use a more detailed look with regards to both the tensile and compressive behaviour of wood, thus its inputs require information on the stress-strain relationships of the wood in both tension and compression, particularly the yield strengths in addition to moduli of elasticity and geometry. Because the size and distribution of failure-causing defects do not scale directly in wood, accounting for this size effect required that the strength data from the coupon samples be adjusted for the force-balance methods.

5.3.2 Model inputs

To validate prediction models for the bending strength of FRP-reinforced wood, a set of strain data from various locations of the beam was obtained for each specimen. These values were selected to occur at or near the peak tensile yield strength of the wood portion, which was typically the first component to fail; the values used for analysis in this section are presented in Table 5.5 and their positions are shown in the load-strain-displacement graphs in Appendix D.

Table 5.5: Beam data at wood tensile failure

Beam ID	$P^{\,a)}$ [kN]	$\Delta^{\,b)}$ [mm]	$\varepsilon_c^{\,d)}\times 10^3$ [mm/mm]	$\varepsilon_t^{\,c)}\times 10^3$ [mm/mm]	$\varepsilon_r^{\,e)}\times 10^3$ [mm/mm]
SN-1	48.4	27.2	2.75	3.99	N/A
SF-1	77.0	48.4	3.35	6.22	7.32
SF-2	54.8	32.6	3.63	3.88	2.43
SB-1	70.1	38.6	4.34	5.05	2.22
SB-2	39.9	25.2	2.54	2.53	1.58
GN-1	47.1	26.3	3.26	2.82	N/A
GN-2	57.7	34.6	4.08	4.85	N/A
GF-1	55.4	50.5	3.95	5.64	6.82
GF-2	56.1	37.8	3.99	5.02	5.59
GB-1	50.4	27.4	2.66	4.13	2.39
GB-2	43.5	29.0	3.41	3.49	2.66

a) Load resistance

b) Midspan displacement

c) Compressive wood strain at midspan

d) Tensile wood strain at midspan

e) FRP tensile strain at midspan

To predict the behaviour of wood beams without relying on experimental test data (*e.g.*, with the moment-curvature approach used by Lacroix & Doudak (2018a)), strength input values may be drawn from coupon tests. However, due to the randomized presence of defects, data obtained from small wood samples must be modified to compensate for the size effects of wood to become better representative of the full-sized elements. Length and depth parameters for the current analysis were obtained from Barrett & Lau (1994) where applicable. On the other hand, depth parameters for both types of compression coupons were found to be unnecessary: for the sawn timber, full-scale properties were already obtained by O’Callaghan (2021); as for glulam, the depth effect is taken based on the smallest dimension of each comprising element—which, in this case, is the width of a full wood lamination in both the coupon and the full-sized beam. The coupon properties were adjusted (where applicable) using the methods described in Section 2.5.5. The resulting values are summarized in Table 5.6 and Figure 5.15.

Table 5.6: Size Effect Adjustments

Property		Sawn Timber		Glulam	
		Compression	Tension	Compression	Tension
Coupon strength [MPa]	f_s	–30.2	+72.0	–52.7	+98.7
Coupon length [mm]	L_s	685	50	195	50
Coupon depth [mm]	d_s	140	2.87	38 a)	3.38
Length effect parameter b)	k_1	10.0	5.88	10.0	5.88
Depth effect parameter b)	k_2	N/A c)	4.76	N/A c)	4.76
Effective beam length [mm]	L_e	798	871	798	871
Effective beam depth [mm]	d	140	140	38	38
Modulus of elasticity [GPa]	E	8.47	10.9	10.1	13.1
Adjusted yield strength [MPa]	f_y	–29.7	+19.6	–45.8	+36.5
Adjusted failure strength [MPa]	f_u	–23.8	+19.6	–30.3	+36.5
Adjusted yield strain $[10^{-3}]$	ε_y	–3.51	+1.80	–4.54	+2.78
Adjusted failure strain $[10^{-3}]$	ε_u	–4.25	+1.80	–36.6	+2.78

a) Actual glulam compression coupon depth was 50 mm, containing one full 38 mm wood lamination.

b) Barrett & Lau (1994)

c) Where no size adjustment was required, the parameter is taken at unity.

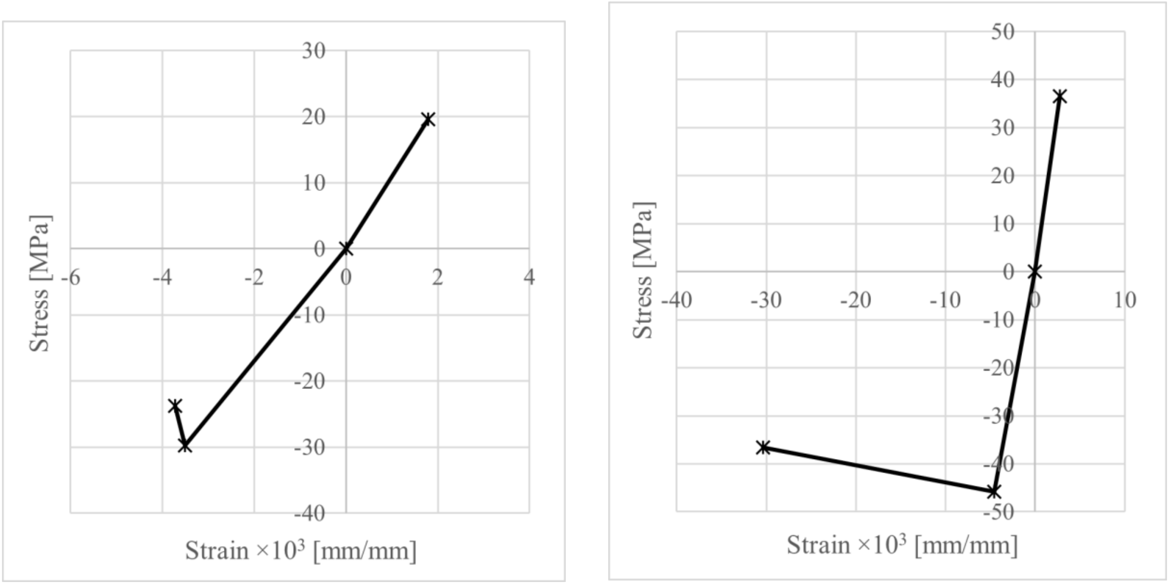

(a) Sawn timber (b) Glulam

Figure 5.15: Adjusted wood stress-strain relationship

5.3.3 Transformed-area method

Predictions for the maximum load resistance of each beam were made by applying the transformed area analysis method as described in Section 2.5.2 using geometric inputs from Figure 3.3 and coupon data from Table 4.4 and Section 5.3.2. In this method, the components are assumed to fail in tension, therefore only tensile moduli of elasticity are applied. The results from this analysis are presented and compared to the actual test results at peak loading in Table 5.7 and Figure 5.16.

Table 5.7: Prediction Accuracy of Transformed-Area Method at Peak Loading

Beam	$P_{r,calc}^{a)}$	$P_{r,test}^{b)}$	**Beam**	$P_{r,calc}^{a)}$	$P_{r,test}^{b)}$
SN-1	52.7	52.7	GN-1	47.1	47.1
			GN-2	57.8	57.8
SF-1	58.0	80.0	GF-1	56.7	71.3
SF-2	58.4	55.0	GF-2	57.0	62.7
SB-1	56.2	70.1	GB-1	55.0	50.4
SB-2	57.0	45.1	GB-2	54.9	49.0

a) Predicted maximum load resistance(s) in kN

b) Actual maximum load resistance in kN

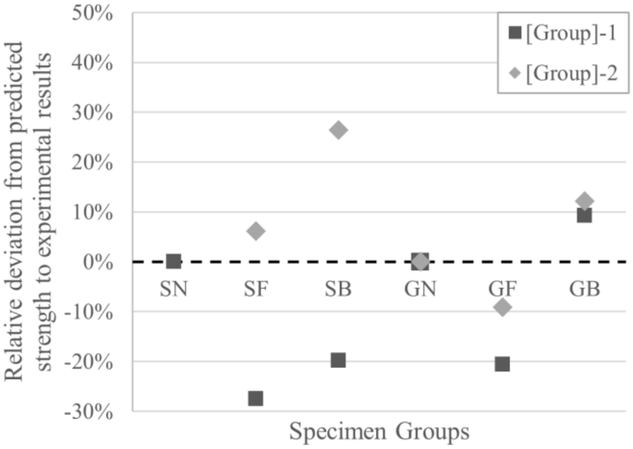

Figure 5.16: Prediction accuracy of transformed-area method at peak loading

The predictions using this method proved to be accurate when applied to the unreinforced beams, but the results for the FRP-reinforced beams of either type gave comparatively scattered outputs. Because of its simplistic assumption of fully linear-elastic behaviour, the transformed-area model failed to address the ductile nature of compressive wood failure should the tensile failure be delayed (*e.g.*, from external reinforcement), confirmed by both the wrinkling fibres observed on the top surface of the beam and the enhanced tensile strength. Additionally, no distinction is made between the compressive and tensile moduli of elasticity for either material, which could affect results should they differ noticeably. This method is thus insufficient for predicting the behaviour of FRP-reinforced timber beams, necessitating a more nuanced approach with the non-linear behaviour of the compression portion post-yielding.

5.3.4 Force-equilibrium analysis

Estimations for the instantaneous load resistance of each beam were made by applying the force-balance analysis method by D’Ambrisi et al. (2014) as described in Section 2.5.3 using material and data inputs from Section 3.2 and Section 5.3.2, respectively. In this scenario, the compression strains on the top edge are assumed to have yielded (*i.e.*, $\varepsilon_c > \varepsilon_0$). The results from this analysis are presented and compared to the actual test results in Table 5.8 and Figure 5.17.

Table 5.8: Estimation Accuracy of Force Equilibrium Method

Beam	**$P_{r,calc}$ a) [kN]**	**$P_{r,test}$ b) [kN]**	**Beam**	**$P_{r,calc}$ a) [kN]**	**$P_{r,test}$ b) [kN]**
SN-1	55.8	48.4	GN-1	39.0	47.1
			GN-2	66.9	57.7
SF-1	84.7	77.0	GF-1	79.1	55.4
SF-2	61.9	54.8	GF-2	72.8	56.1
SB-1	87.7	70.1	GB-1	60.3	50.4
SB-2	45.1	39.9	GB-2	57.1	43.5

a) Predicted maximum load resistance(s) at initial failure

b) Actual maximum load resistance at initial failure

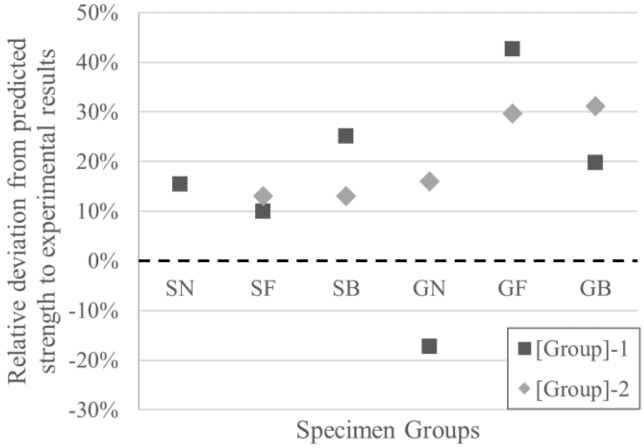

Figure 5.17: Estimation accuracy of force equilibrium method

Although the FRP-reinforced beams are slightly better represented overall with this method compared to the previous area transformation, the outputs still differed noticeably. This method relies on the existence of recorded strain data at the top and bottom of the wood portion of the beam, and as such, it may not be well-suited to predictive modelling without iterative knowledge of the bending curvature. Another primary issue with this approach is the simplistic assumption of elastic-perfectly plastic behaviour of wood subject to compression, whereas more nuanced models (Bazan, 1980; Buchanan, 1984, 1990; Glos, 1978) indicate that the compressive strength of wood declines when its elastic limit is exceeded, thus requiring a more conservative approach.

Rather than using an averaged stiffness value, a slight modification to the above method is to incorporate the compressive and tensile stiffnesses of wood separately, presented in Equation 5.1:

$$M_R = E_{wc}\left[\frac{(h-x)^2}{6}\left(2\varepsilon_u - \frac{\varepsilon_0^3}{\varepsilon_u^2}\right)b\right] + E_{wt}\left[\frac{\varepsilon_0 x^2}{2}b + \varepsilon_u n A_f (d_f - x)\right] \tag{5.1}$$

where M_R is the maximum moment resistance about its neutral axis; b is the width of the beam*;* E_{wc} is the elastic modulus of the wood in compression; h is the height of the beam; x is the neutral axis of the transformed section measured from the top of the beam determined by Equation 2.11; ε_0 is the compressive strain at the top of the beam; ε_u is the tensile strain at the bottom of the wood; E_{wc} is the elastic modulus of the wood in tension; n is the ratio between the tensile moduli of elasticity of the FRP reinforcement and the wood; A_f is the area of the FRP reinforcement; and A_f is the total area of the FRP reinforcement; and d_f is the vertical distance of the centroid of A_f measured from the top of the beam. It should be noted that an assumption remains in this model that the depth of peak compressive yielding can be determined by using approximately-similar triangles above and below the neutral axis in the stress distribution diagram. The results from this analysis are presented and compared to the actual test results in Table 5.9 and Figure 5.18.

Table 5.9: Estimation Accuracy of Modified Force Equilibrium Method

Beam	$P_{r,calc}$ a) [kN]	$P_{r,test}$ b) [kN]	Beam	$P_{r,calc}$ a) [kN]	$P_{r,test}$ b) [kN]
SN-1	50.6	48.4	GN-1	37.9	47.1
			GN-2	61.4	57.7
SF-1	77.3	77.0	GF-1	72.3	55.4
SF-2	58.3	54.8	GF-2	67.1	56.1
SB-1	82.6	70.1	GB-1	55.6	50.4
SB-2	43.2	39.9	GB-2	54.3	43.5

a) Predicted maximum load resistance(s) at initial failure

b) Actual maximum load resistance at initial failure

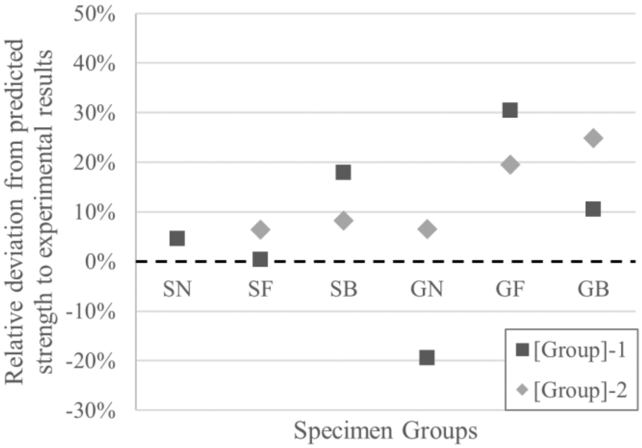

Figure 5.18: Estimation accuracy of modified force equilibrium method

5.3.5 Summary

Simplified methods to evaluate the maximum resistance of sawn timber and glulam beams reinforced with GFRP fabric and bars are not adequate. The observed discrepancy can in part be attributed to (1) the limited sample size, and (2) the failure mode in the test experiment differing from that assumed in the model, which assumes a pure-flexural failure mode. More research is required to develop accurate tools to predict the maximum resistance of FRP-reinforced sawn timber and glulam beams.

Chapter 6
Conclusions

6.1 General

This chapter summarizes the research described in the previous chapters and provides commentary on which further investigation may be recommended.

6.2 Conclusions

Eleven SPF No. 2 wood beams—five 140 mm × 140 mm sawn timber and six 110 mm × 140 mm glulam, all with span lengths of 2,025 mm—were tested for flexure under four-point bending. Of these, two of each type were reinforced with GFRP fabric, two of each type were reinforced with GFRP bars, and the remaining were left unreinforced. Experimental results, including mechanical properties and failure modes, and numerical methods were presented and discussed.

The following conclusions can be drawn from the current study:

- The composite makeup of glulam, compared to sawn timber, interrupts crack propagation through wood beams and allows for secondary peaks to occur; whereas the sawn timber beam failed shortly after peak loading, both glulam beams exhibited some level of post-peak behaviour or residual capacity after initial failure.
- The addition of approximately 2% GFRP fabric-laminate reinforcement strengthened the sawn timber and glulam beams both by averages of 28%, respectively. The defect-bridging effect of the GFRP allowed the effective transfer of stresses, allowing failure modes to transition from brittle tension to ductile compression. The failure occurred generally at the terminus point of the laminate.
- The addition of approximately 2% GFRP rebar reinforcement did not provide significant strength enhancement (+9/-5% for sawn timber and glulam, respectively) due to its positioning before the extreme tension fibre of the wood. However, upon failure of the extreme tension fibre, tension stresses were largely transferred to the FRP bars, allowing for noticeable post-peak resistance and introducing more sustained deformation to the overall beam.
- The enhancements from GFRP fabric-laminates resulted in the most consistent peak strengths without post-peak behaviour. This suggests the limiting factor to failure in fabric-reinforced beams is the wood itself; once it fails, the reinforcement becomes ineffective.

- Due to the variable nature of wood and the consequential size effects when translating data from small wood samples to larger specimens, analysis methods for predicting the peak flexural strength of FRP-reinforced wood may yield imprecise results.

6.3 Recommendations for Future Work

The following identifies topics, based on the research in the present thesis, in which further investigation is recommended:

- Increased sample size for all configurations investigated in the present study to improve upon the observations and analysis methods presented herein;
- Analysis methods based on more precise wood-compression models alternative to those applied in Section 5.3, such as the one proposed by Glos (1978), to verify if and to what degree simplified methods may be permissible;
- Variation of specimen geometry and/or materials—beam cross-section sizes, span-to-depth ratios, species (*e.g.*, Douglas fir), and composition (*e.g.*, laminated veneer lumber); reinforcement types (*e.g.*, CFRP), configurations (*e.g.*, confinement), cover depth, and ratios— to validate or improve upon the analysis methods presented herein;
- Influence of boundary conditions, load patterning, and load duration; varied and/or cycled environmental conditions known to affect wood or FRP performance (*e.g.*, moisture content, exposure to ultraviolet radiation, salts, and temperatures).

References

ACI. (2008). *Guide for the Design and Construction of Externally Bonded FRP Systems for Strengthening Concrete Structures (ACI 440.2R-08)*. American Concrete Institute.

Al-Hayek, H., & Svecova, D. (2014). Flexural strength of posttensioned timber beams. *Journal of Composites for Construction*, *18*(2). https://doi.org/10.1061/(ASCE)CC.1943-5614.0000431

André, A., Kliger, R., & Asp, L. E. (2014). Compression failure mechanism in small scale timber specimens. *Construction and Building Materials*, *50*, 130–139. https://doi.org/10.1016/j.conbuildmat.2013.09.018

André, A., Kliger, R., & Olsson, R. (2013). Compression failure mechanism in small-scale wood specimens reinforced with CFRP: An experimental study. *Construction and Building Materials*, *41*, 790–800. https://doi.org/10.1016/j.conbuildmat.2012.12.038

ASTM. (2011a). *Standard Practice for Establishing Clear Wood Strength Values (ASTM D2555-06)*. American Society for Testing and Materials. https://doi.org/10.1520/D2555-06R11

ASTM. (2011b). *Standard Test Method for Tensile Properties of Fiber Reinforced Polymer Matrix Composite Bars (ASTM D7205/D7205M-06)*. American Society for Testing and Materials. https://doi.org/10.1520/D7205_D7205M-06

ASTM. (2017). *Standard Test Method for Tensile Properties of Polymer Matrix Composite Materials (ASTM D3039/D3039M-14)*. American Society for Testing and Materials. https://doi.org/10.1520/D3039_D3039M-14

ASTM. (2021a). *Standard Test Methods for Small Clear Specimens of Timber (ASTM D143-14)*. American Society for Testing and Materials. https://doi.org/10.1520/D0143-14

ASTM. (2021b). *Standard Test Methods of Static Tests of Lumber in Structural Sizes (ASTM D198-21)*. American Society for Testing and Materials. https://doi.org/10.1520/D0198-21

Balázs, G. L., & Borosnyói, A. (2001). Long-term behavior of FRP. *Composites in Construction: A Reality*, 84–91. https://doi.org/10.1061/40596(264)10

Barrett, D. L., & Lau, W. (1994). *Canadian Lumber Properties* (E. D. Jones (ed.)). Canadian Wood Council. https://webstore.cwc.ca/product/canadian-lumber-properties/

Bazan, I. M. M. (1980). *Ultimate bending strength of timber beams* [Nova Scotia Technical College]. http://hdl.handle.net/10222/80627

Beer, F. P., Johnston Jr., E. R., DeWolf, J. T., & Mazurek, D. F. (2012). Pure Bending. In M. Lange (Ed.), *Mechanics of Materials* (6th ed., pp. 220–313). McGraw Hill.

Bénichou, N., Kodur, V. K. R., & Sultan, M. A. (2002). Experimental study and numerical modelling of the fire resistance of wood-stud wall assemblies. *Canadian Society for Civil Engineering, 2002*, 1587–1596.

Breyer, D. E., Cobeen, K. E., Fridley, K. J., & Pollock, D. G. (2015). *Design of Wood Structures—ASD/LRFD* (7th ed.). McGraw-Hill.

Brown, L., & Woeste, F. (2022). *Machine Graded Lumber: Technologies, Quality, and Benefits*. Southern Pine Inspection Bureau. https://blog.spib.org/machine-graded-lumber-technologies-quality-and-benefits/

BSI. (2007). *Structural use of timber - Part 4: Fire resistance of timber structures (BS 5268-4)*. British Standards Institution.

Buchan, P. A., & Chen, J. F. (2007). Blast resistance of FRP composites and polymer strengthened concrete and masonry structures–A state-of-the-art review. *Composites Part B: Engineering, 38*(5–6), 509–522. https://doi.org/10.1016/j.compositesb.2006.07.009

Buchanan, A. H. (1984). *Strength model and design methods for bending and axial load interaction in timber members* [University of British Columbia]. https://doi.org/10.14288/1.0062943

Buchanan, A. H. (1990). Bending strength of lumber. *Journal of Structural Engineering*, *116*(5), 1213–1229. https://doi.org/10.1061/(ASCE)0733-9445(1990)116:5(1213)

Buchanan, A. H., & Levine, S. B. (1999). Wood-based building materials and atmospheric carbon emissions. *Environmental Science & Policy*, *2*(6), 427–437. https://doi.org/10.1016/S1462-9011(99)00038-6

Buell, T. W., & Saadatmanesh, H. (2005). Strengthening timber bridge beams using carbon fiber. *Journal of Structural Engineering*, *131*(1), 173–187. https://doi.org/10.1061/(ASCE)0733-9445(2005)131:1(173)

Bulleit, W. M., Sandberg, L. B., & Woods, G. J. (1989). Steel-reinforced glued laminated timber. *Journal of Structural Engineering*, *115*(2), 433–444. https://doi.org/10.1061/(ASCE)0733-9445(1989)115:2(433)

Caiza, P., Shin, M., & Andrawes, B. (2012). Flexure-compression testing of bridge timber piles retrofitted with fiber reinforced polymers. *Open Journal of Civil Engineering*, *2*(3), 115–124. https://doi.org/10.4236/ojce.2012.23017

Callister Jr., W. D., & Rethwisch, D. G. (2003). Composites. In *Materials Science and Engineering: An Introduction* (10th ed.). Wiley.

Canadian Wood Council. (2017). *Wood Design Manual*. Canadian Wood Council.

Canadian Wood Council. (2022). *Mass Timber*. https://cwc.ca/en/how-to-build-with-wood/wood-products/mass-timber/

Chidiaq, R. (2003). *Axial strength of rounded wood poles reinforced with carbon fibers*. State University of New Jersey.

CISC. (2021). *Handbook of Steel Construction* (12th ed.). Canadian Institute of Steel Construction.

CSA. (2019a). *Canadian Highway Bridge Design Code (CSA S6:19)*. Canadian Standards Association.

CSA. (2019b). *Engineering design in wood (CSA O86:14)*. Canadian Standards Association.

Custódio, J., Broughton, J., & Cruz, H. (2009). A review of factors influencing the durability of structural bonded timber joints. *International Journal of Adhesion and Adhesives*, *29*(2), 173–185. https://doi.org/10.1016/j.ijadhadh.2008.03.002

D'Ambrisi, A., Focacci, F., & Luciano, R. (2014). Experimental investigation on flexural behavior of timber beams repaired with CFRP plates. *Composite Structures*, *108*(1), 720–728. https://doi.org/10.1016/j.compstruct.2013.10.005

Davids, W. G., Nagy, E., & Richie, M. C. (2008). Fatigue behavior of composite-reinforced glulam bridge girders. *Journal of Bridge Engineering*, *13*(2), 183–191. https://doi.org/10.1061/(ASCE)1084-0702(2008)13:2(183)

de la Rosa García, P., Escamilla, A. C., & García, M. N. G. (2013). Bending reinforcement of timber beams with composite carbon fiber and basalt fiber materials. *Composites Part B: Engineering*, *55*, 528–536. https://doi.org/10.1016/j.compositesb.2013.07.016

De Luca, V., & Marano, C. (2012). Prestressed glulam timbers reinforced with steel bars. *Construction and Building Materials*, *30*, 206–217. https://doi.org/10.1016/j.conbuildmat.2011.11.016

Demattè, M. L., Zucco, G. M., Roncanto, S., Gatto, P., Paulon, E., Cavalli, R., & Zanetti, M. (2018). New insights into the psychological dimension of wood–human interaction. *European Journal of Wood and Wood Products2*, *76*, 1093–1100. https://doi.org/10.1007/s00107-018-1315-y

Demers, M., & Neale, K. W. (1999). Confinement of reinforced concrete columns with fibre-reinforced composite sheets - an experimental study. *Canadian Journal of Civil Engineering*, *26*(2), 226–241. https://doi.org/10.1139/cjce-26-2-226

Dong, J. F., Jia, P., Yuan, S. C., & Wang, Q. Y. (2015). Compressive behaviours of square timber columns reinforced by partial wrapping of FRP sheets. *Materials Research Innovations*, *19*, S1465–S1468. https://doi.org/10.1179/1432891715Z.0000000001593

Dorey, A. B., & Cheng, J. J. R. (1996a). *Glass fiber reinforced glued laminated wood beams*. Canadian Forest Service.

Dorey, A. B., & Cheng, J. J. R. (1996b). The behavior of GFRP glued laminated timber beams. In M. M. El-Badry (Ed.), *Advanced Composite Materials in Bridges and Structures II*. Canadian Society for Civil Engineering.

Egbo, M. K. (2021). A fundamental review on composite materials and some of their applications in biomedical engineering. *Journal of King Saud University - Engineering Sciences*, *33*(8), 557–568. https://doi.org/10.1016/j.jksues.2020.07.007

Emerson, R. N. (2004). In situ repair technique for decayed timber piles. *Structures Congress 2004 - Building on the Past: Securing the Future*, *405*, 593–601. https://doi.org/10.1061/40700(2004)65

Estrada, H., & Lee, L. S. (2014). FRP Composite Constituent Materials. In M. Zoghi (Ed.), *The International Handbook of FRP Composites in Civil Engineering* (pp. 31–50). Taylor & Francis.

Fiberline Composites. (2017). *ComBAR® by Fiberline: Technical Information*. https://1stdirectory.co.uk/_assets/files_comp/c9cb3ce6-9b2e-4ad7-b3aa-5b29c178489d.pdf

Fitzer, E., Kleinholz, R., Tiesler, H., Stacey, M. H., De Bruyne, R., Lefever, I., & Heine, M. (2000). Fibers, 5. Synthetic Inorganic. In *Ullmann's Encyclopedia of Industrial Chemistry* (7th ed.). Wiley-VCH Verlag GmbH & Co. KGaA. https://doi.org/10.1002/14356007.a11_001

Forest Products Laboratory. (2010). *Wood Handbook: Wood as an Engineering Material (General Technical Report FPL-GTR-190)* (R. J. Ross (ed.); Centennial). United States Department of Agriculture.

Fox, S. P. (1978). *Bending strength of a proposed Douglas-fir 20f glulam stress grade* (Issue VP-X-175). Environment Canada, Canadian Forestry Service, Western Forest Products Laboratory.

Fu, S. Y., & Lauke, B. (1996). Effects of fiber length and fiber orientation distributions on the tensile strength of short-fiber-reinforced polymers. *Composites Science and Technology*, *56*(10), 1179–1190. https://doi.org/10.1016/S0266-3538(96)00072-3

Gentile, C. (2000). *Flexural strengthening of timber bridge beams using FRP* [University of Manitoba]. http://hdl.handle.net/1993/19514

Gentile, C., Svecova, D., & Rizkalla, S. H. (2002). Timber beams strengthened with GFRP bars: Development and applications. *Journal of Composites for Construction*, *6*(1), 11–20. https://doi.org/10.1061/(ASCE)1090-0268(2002)6:1(11)

Glos, P. (1978). *Zur Bestimmung des Festigkeitsverhaltens von Brettschichtholz bei Druckbeanspruchung aus Werkstoff-und Einwirkungskenngrößen*. Technische Universität München.

Green, M. (2017). *The Case for Tall Wood Buildings* (2nd ed.). Michael Green Architecture. http://thecasefortallwood.com/wp-content/uploads/2017/02/2017-01-24-THE-CASE-FOR-TALL-WOOD-SECOND-EDITION.pdf

Gustavsson, L., & Sathre, R. (2006). Variability in energy and carbon dioxide balances of wood and concrete building materials. *Building and Environment*, *41*(7), 940–951. https://doi.org/10.1016/j.buildenv.2005.04.008

Hadi, M. N. S. (2005). Behaviour of FRP strengthened concrete columns under eccentric compression loading. *Composite Structures*, *77*(1), 92–96. https://doi.org/10.1016/j.compstruct.2005.06.007

Hay, S., Thiessen, K., Svecova, D., & Bakht, B. (2006). Effectiveness of GFRP sheets for shear strengthening of timber. *Journal of Composites for Construction*, *10*(6), 483–491. https://doi.org/10.1061/(ASCE)1090-0268(2006)10:6(483)

Heiduschke, A., & Haller, P. (2010). Fiber-reinforced plastic-confined wood profiles under axial compression. *Structural Engineering International: Journal of the International Association for Bridge and Structural Engineering (IABSE)*, *20*(3), 246–253. https://doi.org/10.2749/101686610792016772

Hernandez, R., Davalos F., J., Sonti, S. S., Kim, Y., & Moody C., R. (1997). *Strength and stiffness of reinforced yellow-poplar glued laminated beams* (Issue FPL-RP-554). U.S. Department of Agriculture, Forest Service, Forest Products Laboratory.

Hollaway, L. C. (2010). A review of the present and future utilisation of FRP composites in the civil infrastructure with reference to their importance in-service properties. *Construction and Building Materials2*, *24*(12), 2419–2445. https://doi.org/10.1016/j.conbuildmat.2010.04.062

Hoyle Jr., R. J. (1975). Steel-reinforced wood beam design. *Forest Products Journal*.

Iacobucci, R. D., Sheikh, S. A., & Bayrak, O. (2003). Retrofit of square concrete columns with carbon fiber-reinforced polymer for seismic resistance. *ACI Structural Journal*, *100*(6), 785–794. https://doi.org/10.14359/12845

IEA. (2018). *2018 Global Status Report: Towards a zero-emission, efficient and resilient buildings and construction sector*. https://www.iea.org/reports/2018-global-status-report

IPCC. (2018). *Global Warming of 1.5°C*. Intergovernmental Panel on Climate Change. https://www.ipcc.ch/sr15/download/

Jacques, E., Lloyd, A., Imbeau, P., Palermo, D., & Quek, J. (2015). GFRP-retrofitted reinforced concrete columns subjected to simulated blast loading. *Journal of Structural Engineering*, *141*(11). https://doi.org/10.1061/(ASCE)ST.1943-541X.0001251

Ji, G., Li, G., & Alaywan, W. (2013). A new fire resistant FRP for externally bonded concrete repair. *Construction and Building Materials*, *42*, 87–96. https://doi.org/10.1016/j.conbuildmat.2013.01.008

Johns, K. C., & Lacroix, S. (2000). Composite reinforcement of timber in bending. *Canadian Journal of Civil Engineering*, *27*(5), 899–906. https://doi.org/10.1139/l00-017

Jones, C. (2019). *Inventory of Carbon and Energy (ICE Database)* (3.0). https://circularecology.com/embodied-carbon-footprint-database.html

Kim, K.-H. E., & Andrawes, B. (2016). Compression behavior of FRP strengthened bridge timber piles subjected to accelerated aging. *Construction and Building Materials*, *124*, 177–185. https://doi.org/10.1016/j.conbuildmat.2016.07.020

Kodur, V. K. R., & Naser, M. Z. (2020). *Structural Fire Engineering*. McGraw Hill.

Kodur, V. K. R., & Yu, B. (2016). Rational approach for evaluating fire resistance of FRP-strengthened concrete beams. *Journal of Composites for Construction*, *20*(6). https://doi.org/10.1061/(ASCE)CC.1943-5614.0000697

Lacroix, D. (2017a). *Investigating the behaviour of glulam beams and columns subjected to simulated blast loading* [University of Ottawa]. https://doi.org/10.20381/ruor-21031

Lacroix, D. (2017b). Investigating the Behaviour of Glulam Beams and Columns Subjected to Simulated Blast Loading. *Civil Engineering*, *Ph.D.*, 294.

Lacroix, D., & Doudak, G. (2018a). Experimental and analytical investigation of FRP retrofitted glued-laminated beams subjected to simulated blast loading. *Journal of Structural Engineering*, *144*(7). https://doi.org/10.1061/(ASCE)ST.1943-541X.0002084

Lacroix, D., & Doudak, G. (2018b). FRP reinforced glulam beams under high strain-rates. *CSCE 2018 Annual Conference*.

Lacroix, D., & Doudak, G. (2020). Towards enhancing the post-peak performance of glued-laminated timber beams using multi-directional fibre reinforced polymers. *Engineering Structures, 215*(April), 110680. https://doi.org/10.1016/j.engstruct.2020.110680

Lacroix, D., Viau, C., Battelli, E. M., & Doudak, G. (2021). Enhancing the performance of light-frame wood studs using glass fibre-reinforced polymers. *Engineering Structures*, *245*. https://doi.org/10.1016/J.ENGSTRUCT.2021.112973

Larasatie, P., Guerrero, J. E., Conroy, K., Hall, T. E., Hansen, E., & Needham, M. D. (2018). What does the public believe about tall wood buildings? An exploratory study in the US Pacific Northwest. *Journal of Forestry*, *116*(5), 429–436. https://doi.org/10.1093/jofore/fvy025

Lee, J.-J., & Kim, G.-C. (2000). Study on the estimation of the strength properties of structural glued laminated timber I: determination of optimum MOE as input variable. *Journal of Wood Science, 46*, 115–121.

Legg, C., & Tingley, D. (2020). *Timber Bridge Best Practices and the State of the Industry in Atlantic Canada*. https://wood-works.ca/wp-content/uploads/2020/12/Timber-Bridge-Industry.pdf

Lindyberg, R. F., & Dagher, H. J. (2012). ReLAM: Nonlinear probabilistic model for the analysis of reinforced glulam beams in bending. *Journal of Structural Engineering*, *138*(6), 777–788. https://doi.org/10.1061/(asce)st.1943-541x.0000496

Lochan, P. (2021). *Correlation of Tensile Strength to Flexural Rupture Modulus of GFRP Bars* [University of Waterloo]. http://hdl.handle.net/10012/16943

Madsen, B., & Buchanan, A. H. (1986). Size effects in timber explained by a modified weakest link theory. *Canadian Journal of Civil Engineering1*, *13*(2), 218–232. https://doi.org/10.1139/l86-030

Malhotra, S. K., & Mazur, S. J. (1970). Buckling strength of solid timber columns. *Engineering Journal*, *13*(A-4), 1–7.

Mallick, P. K. (2007). *Fiber-Reinforced Composites: Materials, Manufacturing, and Design* (3rd ed.). Taylor & Francis. https://doi.org/10.1201/9781420005981

Mark, R. (1961). Wood-aluminum beams within and beyond the elastic range. *Forest Products Journal*, *11*(10), 477–484.

Martin, J. A., & Lamanna, A. J. (2008). Performance of mechanically fastened FRP strengthened concrete beams in flexure. *Journal of Composites for Construction, 12*(3). https://doi.org/10.1061/(ASCE)1090-0268(2008)12:3(257)

Martin, Z. A., & Tingley, D. A. (2000). Fire resistance of FRP reinforced glulam beams. *World Conference on Timber Engineering*.

McDaniel, G., & Knight, C. (2014). Fiber Reinforced Polymer (FRP) Composites. *Florida Department of Transportation Design Training Expo*. https://www.fdot.gov/docs/default-source/design/training/designexpo/2014/presentations/GevinMcDaniel-FRP-Composites.pdf

Memon, M. S., & Sheikh, S. A. (2005). Seismic resistance of concrete columns retrofitted with glass fiber-reinforced polymer. *ACI Structural Journal*, *102*(5).

Micelli, F., Myers, J. J., & Murthy, S. (2001). Effect of environmental cycles on concrete cylinders confined with FRP. *CCC2001 International Conference on Composites in Construction*.

Moody, R. C., Hernandez, R., Davalos, J. F., & Sonti, S. S. (1983). *Yellow Poplar Glulam Timber Beam Performance*. United States Department of Agriculture, Forest Service, Forest Products Laboratory.

Najm, H., Secaras, J., & Balaguru, P. (2007). Compression tests of circular timber column confined with carbon fibers using inorganic matrix. *Journal of Materials in Civil Engineering*, *19*(2), 198–204. https://doi.org/10.1061/(asce)0899-1561(2007)19:2(198)

Nanni, A., & Norris, M. S. (1995). FRP jacketed concrete under flexure and combined flexure-compression. *Construction and Building Materials, 9*(5), 273–281. https://doi.org/10.1016/0950-0618(95)00021-7

Natural Resources Canada. (2022). *The State of Canada's Forests: Annual Report 2022*. cfs.nrcan.gc.ca/stateoftheforests

Neely, S. T. (1898). Relation of compression-endwise to breaking load of beam. *Progress in Timber Physics*, 13–17.

O'Callaghan, R. B. (2021). *Effects of GFRP reinforcement on the compressive behaviour of square SPF timber columns* [University of Waterloo]. http://hdl.handle.net/10012/17479

O'Callaghan, R. B., Lacroix, D., & Kim, K. E. (2021). *Experimental investigation of the compressive behaviour of GFRP wrapped spruce-pine-fir square timber columns*.

Pauly, J. J. (1984). The Great Chicago Fire as a national event. *American Quarterly*, *36*(5), 668–683.

Plevris, N., & Triantafillou, T. C. (1992). FRP-reinforced wood as structural material. *Journal of Materials in Civil Engineering*, *4*(3), 300–317. https://doi.org/10.1061/(ASCE)0899-1561(1992)4:3(300)

Plevris, N., & Triantafillou, T. C. (1995). Creep behavior of FRP-reinforced wood members. *Journal of Structural Engineering*, *121*(2), 174–186. https://doi.org/10.1061/(asce)0733-9445(1995)121:2(174)

Raftery, G. M., & Harte, A. M. (2013). Nonlinear numerical modelling of FRP reinforced glued laminated timber. *Composites Part B: Engineering*, *52*, 40–50. https://doi.org/10.1016/j.compositesb.2013.03.038

Ramage, M. H., Burridge, H., Busse-Wicher, M., Fereday, G., Reynolds, T., Shah, D. U., Wu, G., Yu, L., Fleming, P., Densley-Tingley, D., Allwood, J., Dupree, P., Linden, P. F., & Scherman, O. (2017). The wood from the trees: The use of timber in construction. *Renewable and Sustainable Energy Reviews*, *68*(September 2016), 333–359. https://doi.org/10.1016/j.rser.2016.09.107

Shen, J., Zhang, X., & Lian, Z. (2020). Impact of wooden versus nonwooden interior designs on office workers' cognitive performance. *Perceptual and Motor Skills*, *127*(1), 36–51. https://doi.org/10.1177/0031512519876395

Simpson Strong-Tie. (2019). *Technical Data Sheet for CSS-ES*. https://ssttoolbox.widen.net/view/pdf/7xpfqt7hgx/T-R-CSSES.pdf?t.download=true&u=cjmyin

Simpson Strong-Tie. (2020). *Technical Data Sheet for CSS-CUGF27*. https://ssttoolbox.widen.net/view/pdf/krv9sbxynh/T-R-CSSCUGF27.pdf?t.download=true&u=cjmyin

Singh, T. (1987). Wood density variations in thirteen Canadian tree species. *Wood and Fiber Science*, 362–369.

Sólyom, S., Balázs, G. L., & Borosnyói, A. (2015). Bond behaviour of FRP rebars – parameter study. *Conference on Smart Monitoring, Assessment and Rehabilitation of Civil Structures*. https://data.smar-conferences.org/SMAR_2015_Proceedings/papers/290.pdf

Song, J., Kim, S., & Oh, S. (2007). The compressive stress-strain relationship of timber. *International Conference on Sustainable Building Asia*, 977–982. https://www.irbnet.de/daten/iconda/CIB8227.pdf

Song, X., Tang, H., Zhang, W., & Gu, X. (2010). Compressive stress strain relationship of wood confined with fiber composite sheets. *Advanced Materials Research*, *133–134*, 1207–1211.

https://doi.org/10.4028/www.scientific.net/AMR.133-134.1207

Sulaiman, A., Almansour, H., & Aoude, H. (2016). Effect of fiber orientation on the behavior of CFRP confined concrete cylinders. *Canadian Society for Civil Engineering*, *2*, 1251–1263.

Šulc, S., Šmilauer, V., & Wald, F. (2021). Thermal model for timber fire exposure with moving boundary. *Materials*, *14*(3), 1–10. https://doi.org/10.3390/ma14030574

Syed, M. T. (2020). *Identifying mass timber research priorities, barriers to adoption and engineering, procurement and construction challenges in Canada* [University of Toronto]. https://hdl.handle.net/1807/99460

Tomlinson, D., & Fam, A. (2015). Performance of concrete beams reinforced with basalt FRP for flexure and shear. *Journal of Composites for Construction*, *19*(2). https://doi.org/10.1061/(ASCE)CC.1943-5614.0000491

Triantafillou, T. C., & Antonopoulos, C. P. (2000). Design of concrete flexural members strengthened in shear with FRP. *Journal of Composites for Construction*, *4*(4), 198–205. https://doi.org/10.1061/(ASCE)1090-0268(2000)4:4(198)

Vetter, Y. (2022). *Effects of transverse GFRP reinforcement on the flexural behaviour of glulam beams* [University of Waterloo]. http://hdl.handle.net/10012/18457

Xiong, P. (1991). *Modelling strength and stiffness of glued-laminated timber using machine stress rated lumber* [University of British Columbia]. https://doi.org/10.14288/1.0098523

Yan, L., Chouw, N., & Yuan, X. (2012). Improving the mechanical properties of natural fibre fabric reinforced epoxy composites by alkali treatment. *Journal of Reinforced Plastics and Composites*, *31*(6), 425–437. https://doi.org/10.1177/0731684412439494

Yang, H., Liu, W., Lu, W., Zhu, S., & Geng, Q. (2016). Flexural behavior of FRP and steel reinforced glulam beams: Experimental and theoretical evaluation. *Construction and Building Materials*, *106*, 550–563. https://doi.org/10.1016/j.conbuildmat.2015.12.135

Yost, J. R., Goodspeed, C. H., & Schmeckpeper, E. R. (2001). Flexural performance of concrete beams reinforced with FRP grids. *Journal of Composites for Construction*, *5*(1), 18–25. https://doi.org/10.1061/(ASCE)1090-0268(2001)5:1(18)

Zhang, S. S., Yu, T., & Chen, G. M. (2017). Reinforced concrete beams strengthened in flexure with near-surface mounted (NSM) CFRP strips: Current status and research needs. *Composites Part B: Engineering*, *131*(15), 30–42. https://doi.org/10.1016/j.compositesb.2017.07.072

Zhang, W., Song, X., Gu, X., & Tang, H. (2012). Compressive behavior of longitudinally cracked timber columns retrofitted using FRP sheets. *Journal of Structural Engineering*, *138*(1), 90–98. https://doi.org/10.1061/(asce)st.1943-541x.0000423

Zhang, Y., Wei, Y., Bai, J., Wu, G., & Dong, Z. (2020). A novel seawater and sea sand concrete filled FRP-carbon steel composite tube column: Concept and behaviour. *Composite Structures*, *246*. https://doi.org/10.1016/j.compstruct.2020.112421

Zhou, A., Qin, R., Chow, C. L., & Lau, D. (2019). Structural performance of FRP confined seawater concrete columns under chloride environment. *Composite Structures*, *216*, 12–19. https://doi.org/10.1016/j.compstruct.2019.02.058

Zigler, R., & Pokorný, M. (2015). Fire protection of timber structures strengthened with FRP materials. *Stavební Obzor - Civil Engineering Journal*, *24*(4), 1–8. https://doi.org/10.14311/cej.2015.04.0022

Appendix A

Test Results of Wood Compression Coupons

[No image available]

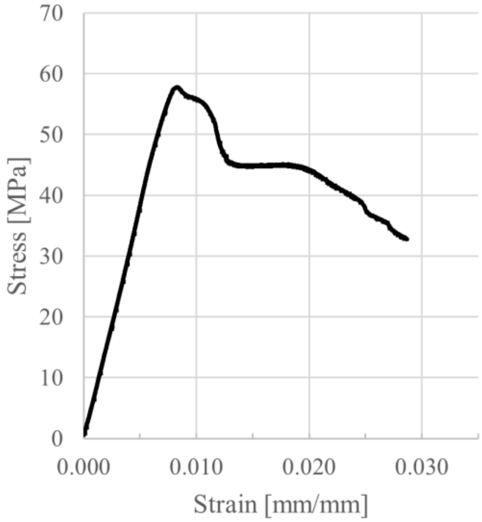

(a) Ultimate failure (b) Stress-strain behaviour

Figure A.1: Compression coupon test of GC-1

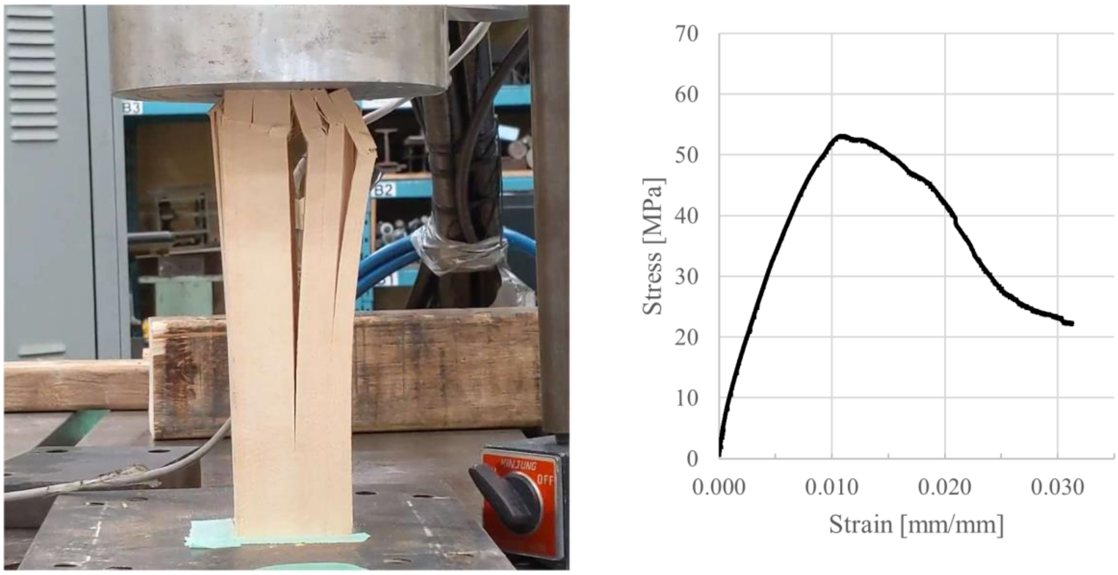

(a) Ultimate failure (b) Stress-strain behaviour

Figure A.2: Compression coupon test of GC-2

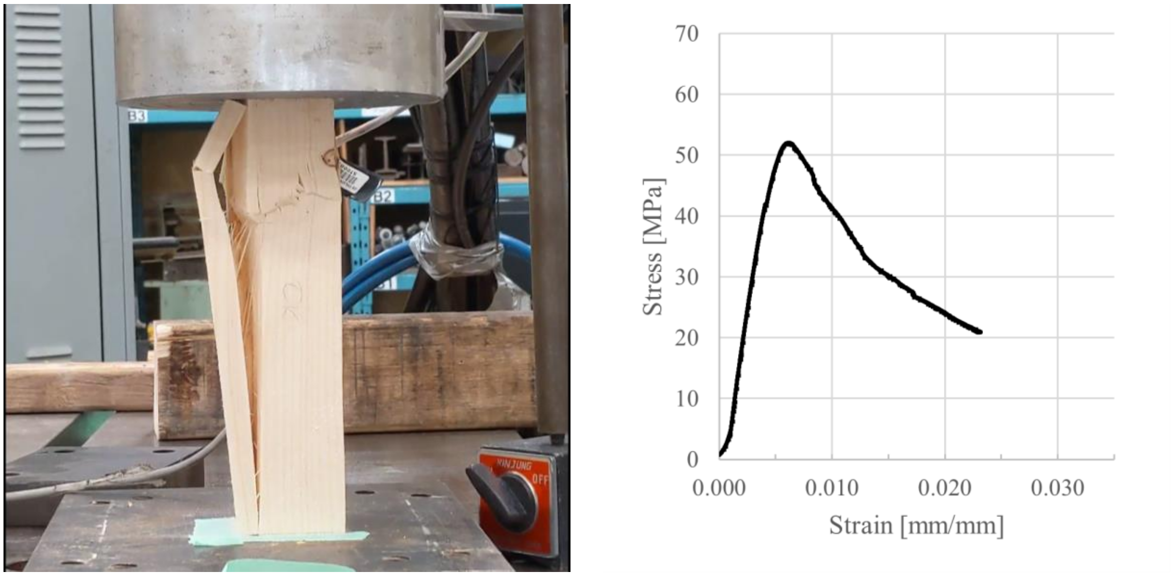

(a) Ultimate failure (b) Stress-strain behaviour

Figure A.3: Compression coupon test of GC-3

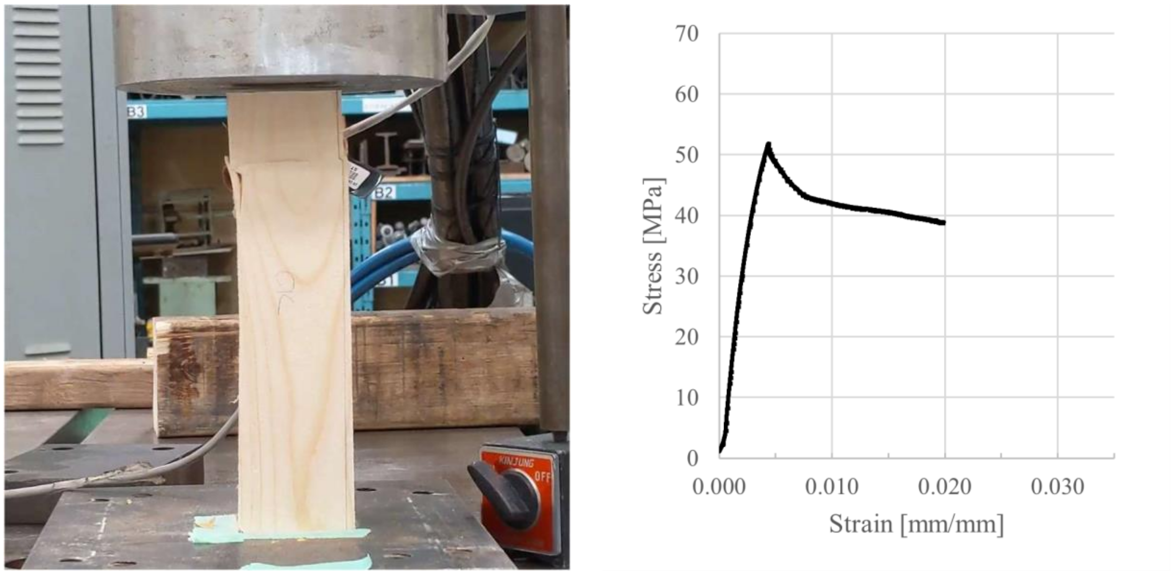

(a) Ultimate failure (b) Stress-strain behaviour

Figure A.4: Compression coupon test of GC-4

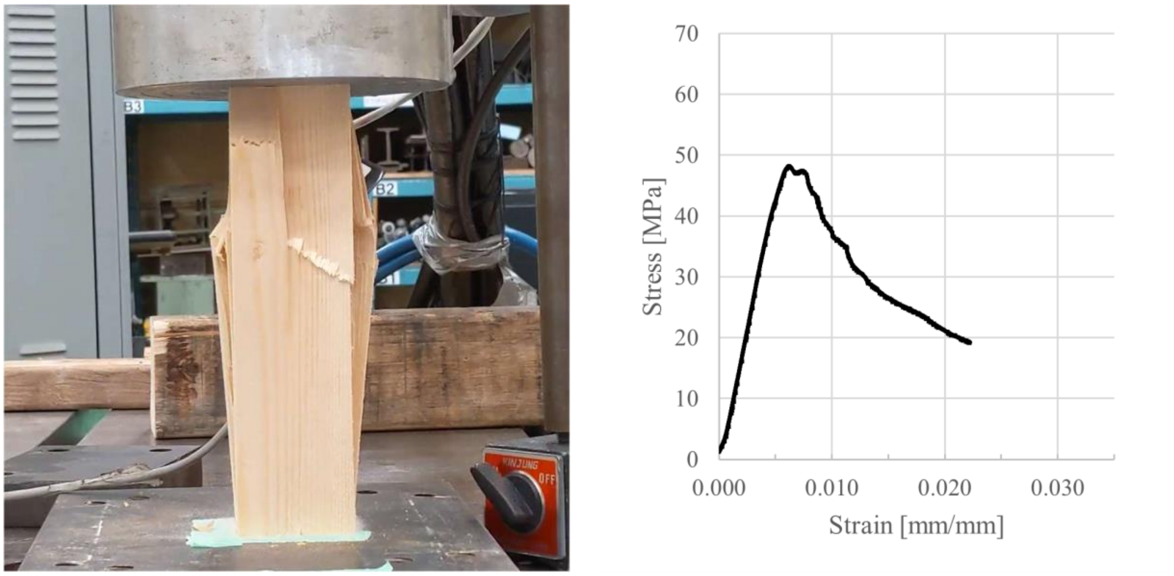

(a) Ultimate failure (b) Stress-strain behaviour

Figure A.5: Compression coupon test of GC-5

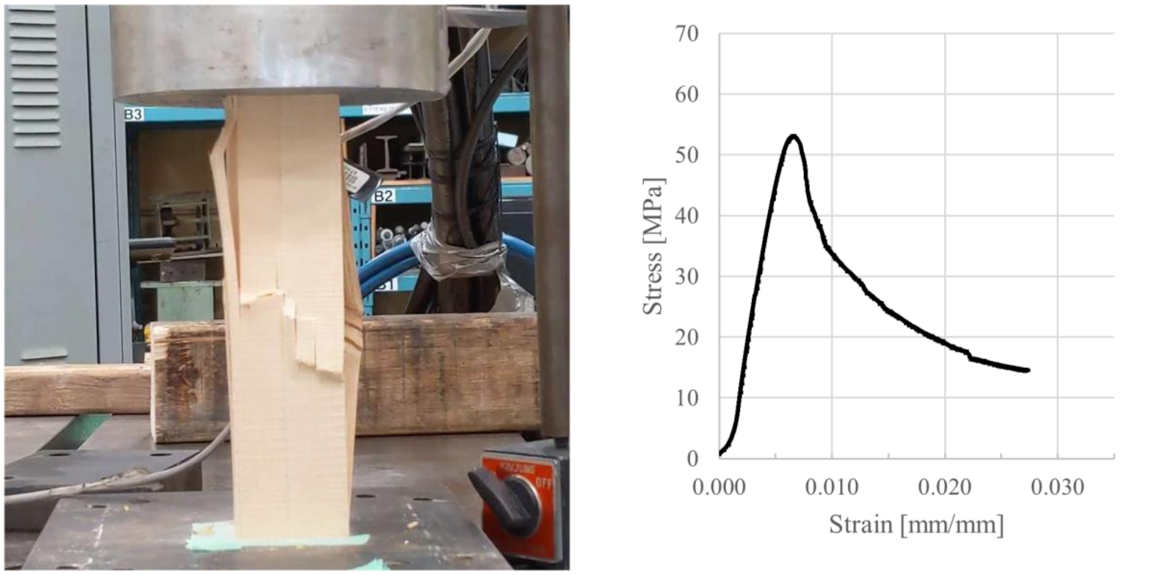

(a) Ultimate failure (b) Stress-strain behaviour

Figure A.6: Compression coupon test of GC-6

Appendix B

Test Results of Wood Tension Coupons

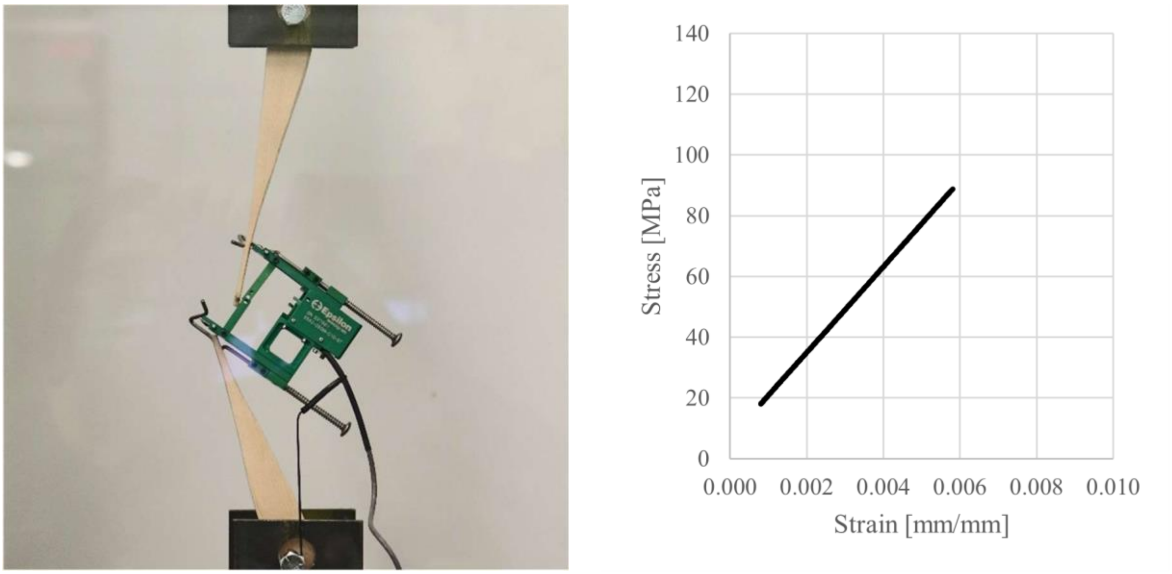

(a) Ultimate failure (b) Stress-strain behaviour

Figure B.1: Tension coupon test of GT-1

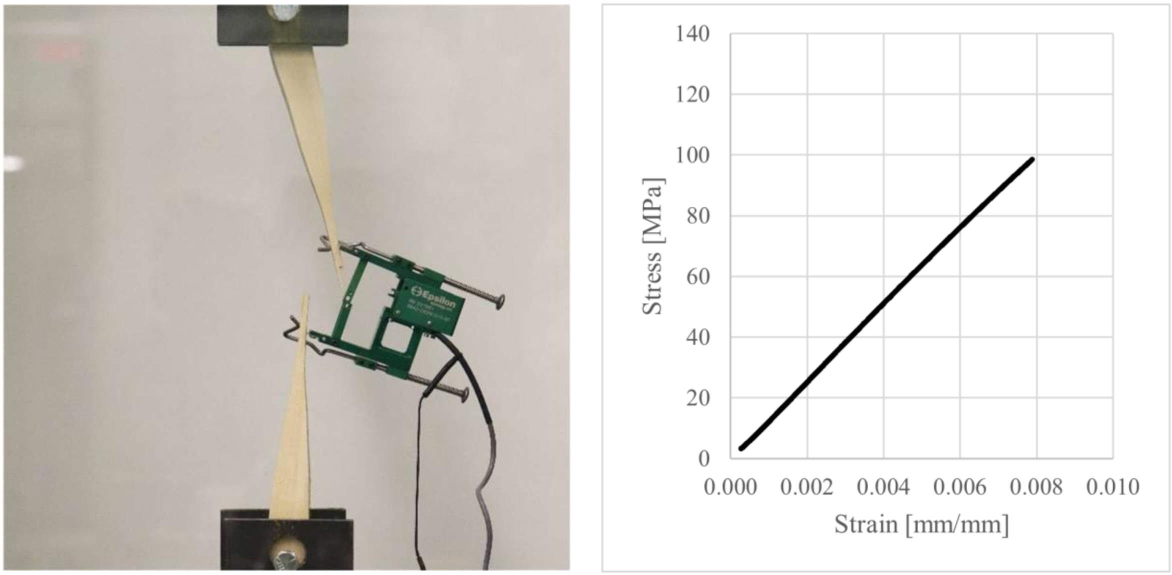

(a) Ultimate failure (b) Stress-strain behaviour

Figure B.2: Tension coupon test of GT-2

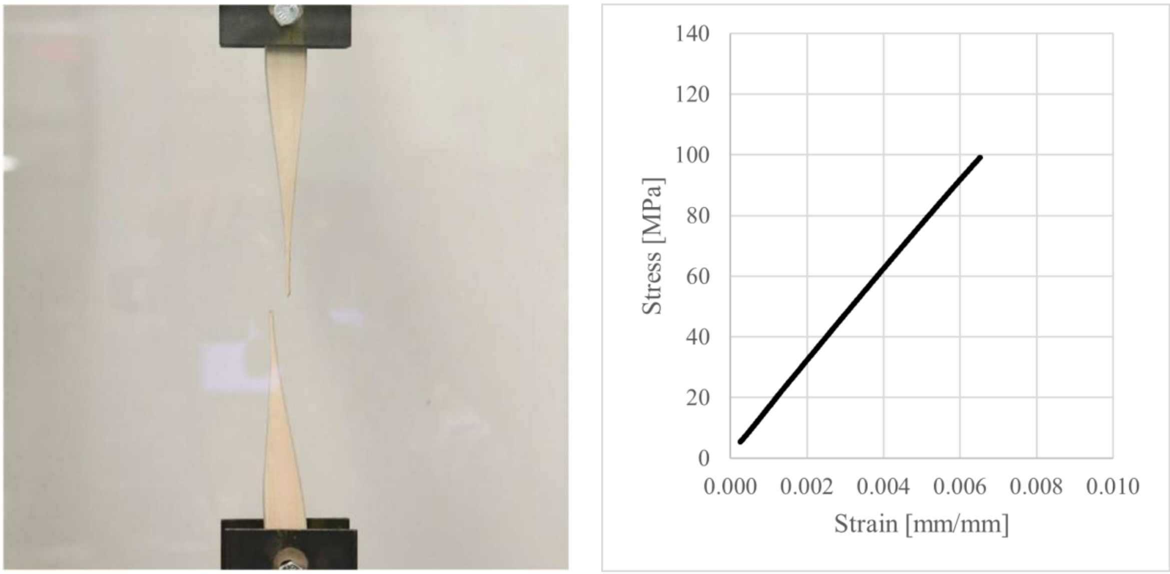

(a) Ultimate failure (b) Stress-strain behaviour

Figure B.3: Tension coupon test of GT-3

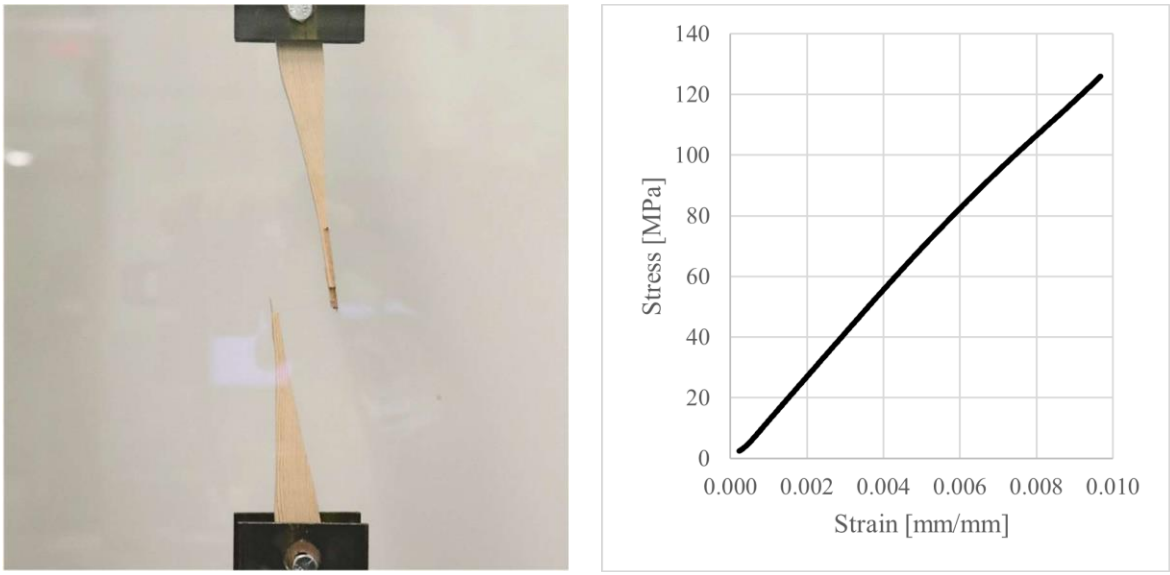

(a) Ultimate failure (b) Stress-strain behaviour

Figure B.4: Tension coupon test of GT-4

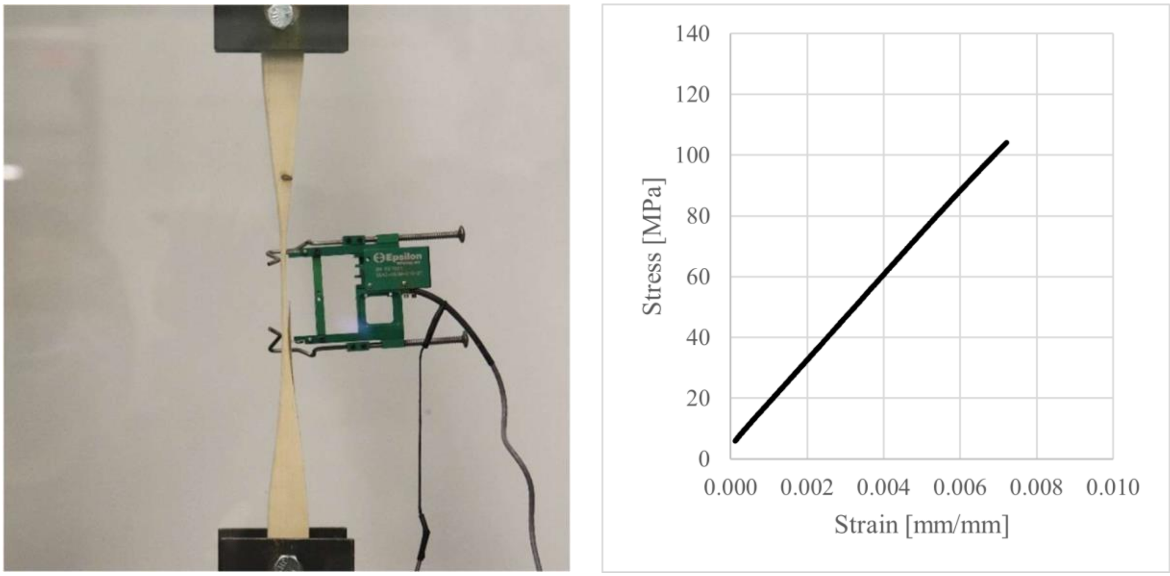

(a) Ultimate failure (b) Stress-strain behaviour

Figure B.5: Tension coupon test of GT-5

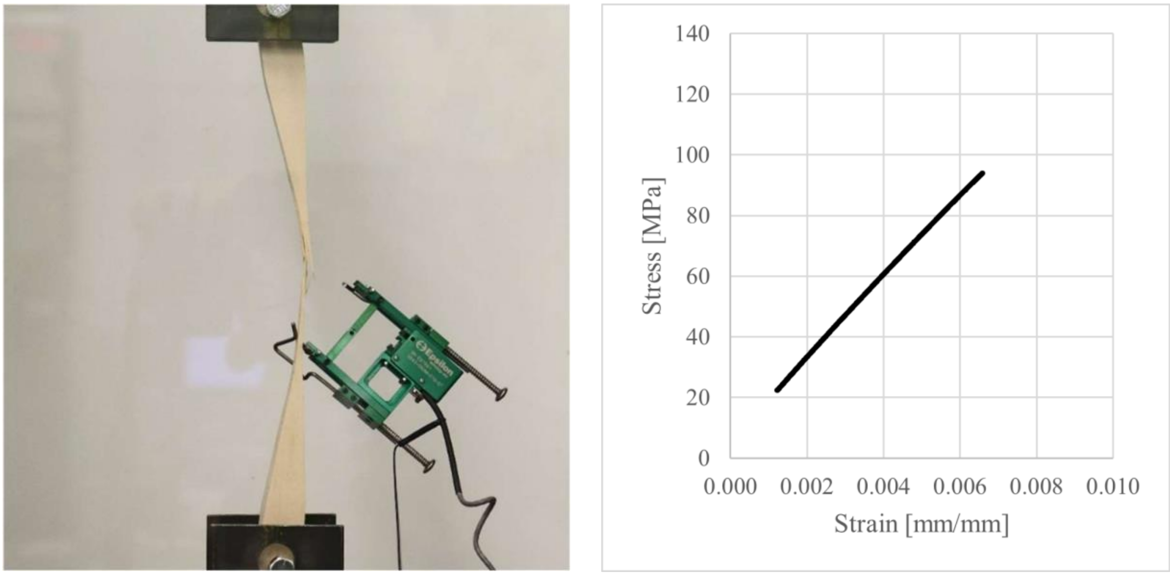

(a) Ultimate failure (b) Stress-strain behaviour

Figure B.6: Tension coupon test of GT-6

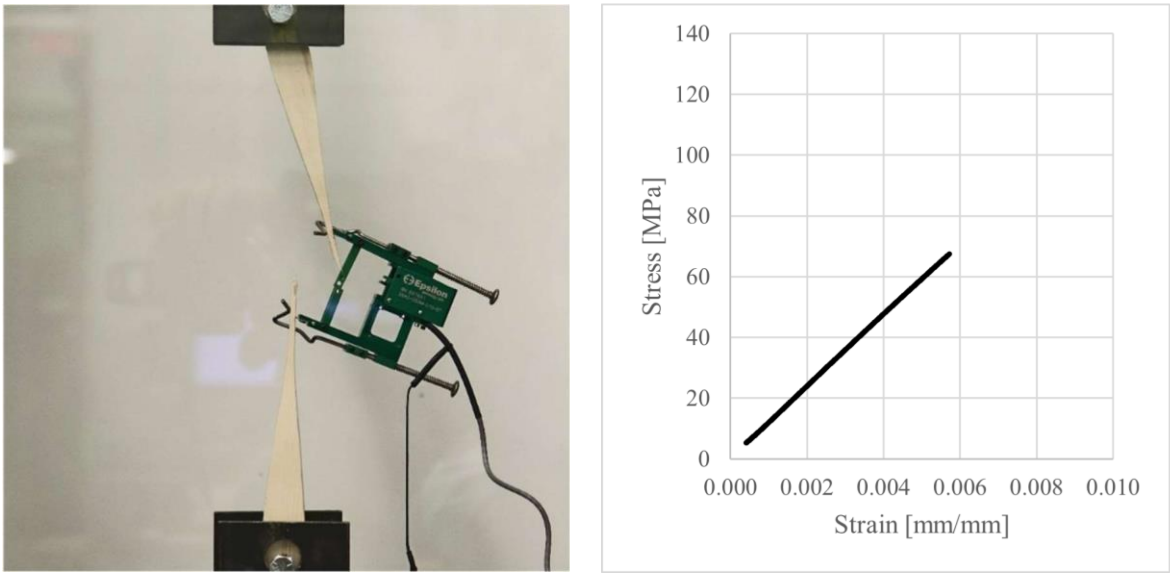

(a) Ultimate failure (b) Stress-strain behaviour

Figure B.7: Tension coupon test of ST-1

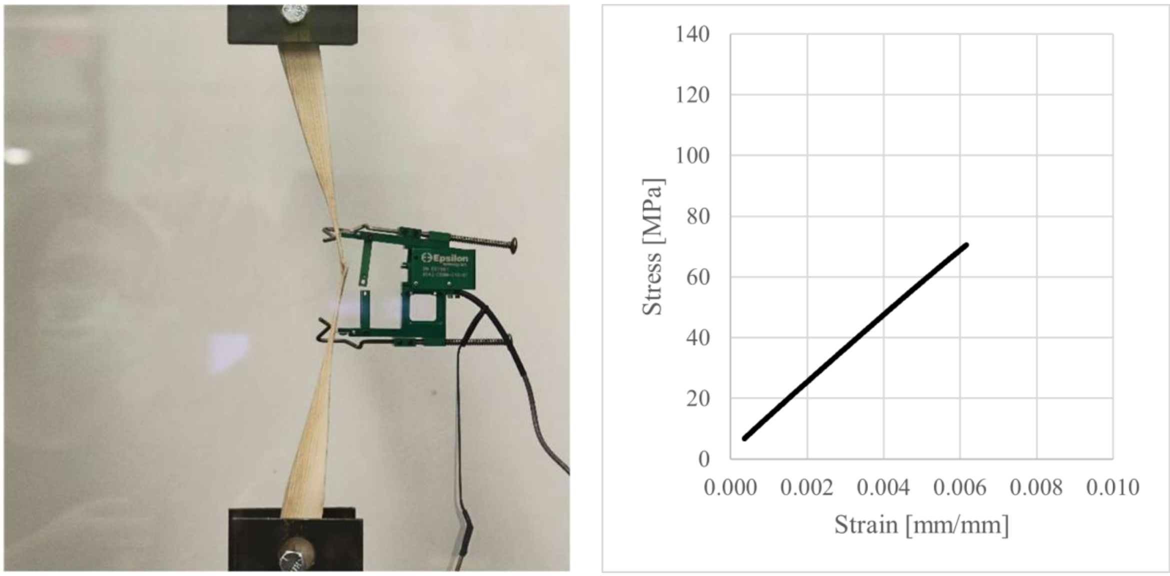

(a) Ultimate failure (b) Stress-strain behaviour

Figure B.8: Tension coupon test of ST-2

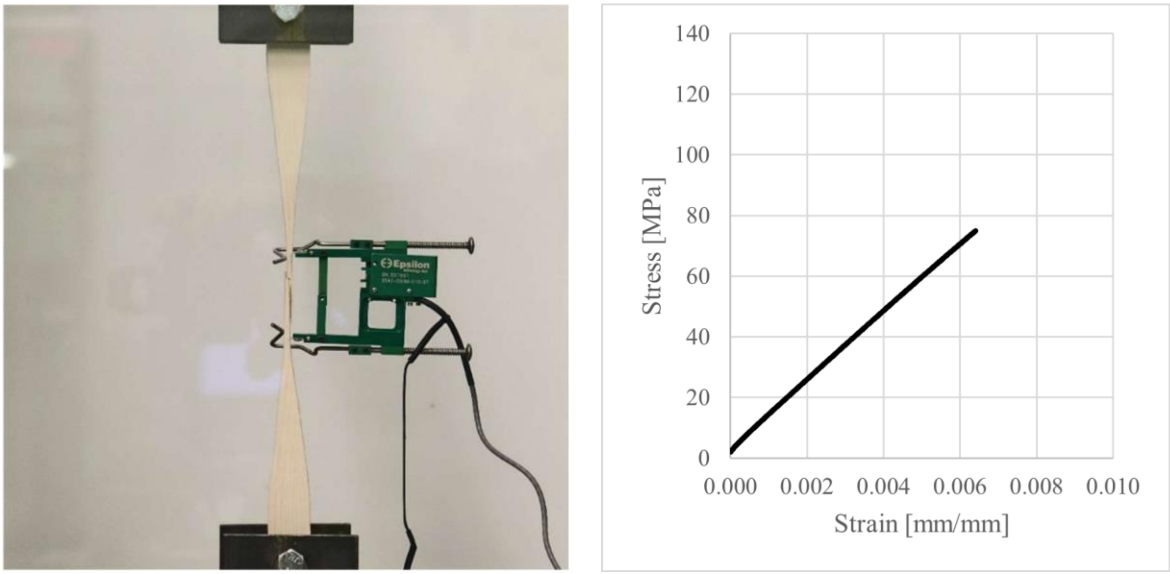

(a) Ultimate failure (b) Stress-strain behaviour

Figure B.9: Tension coupon test of ST-3

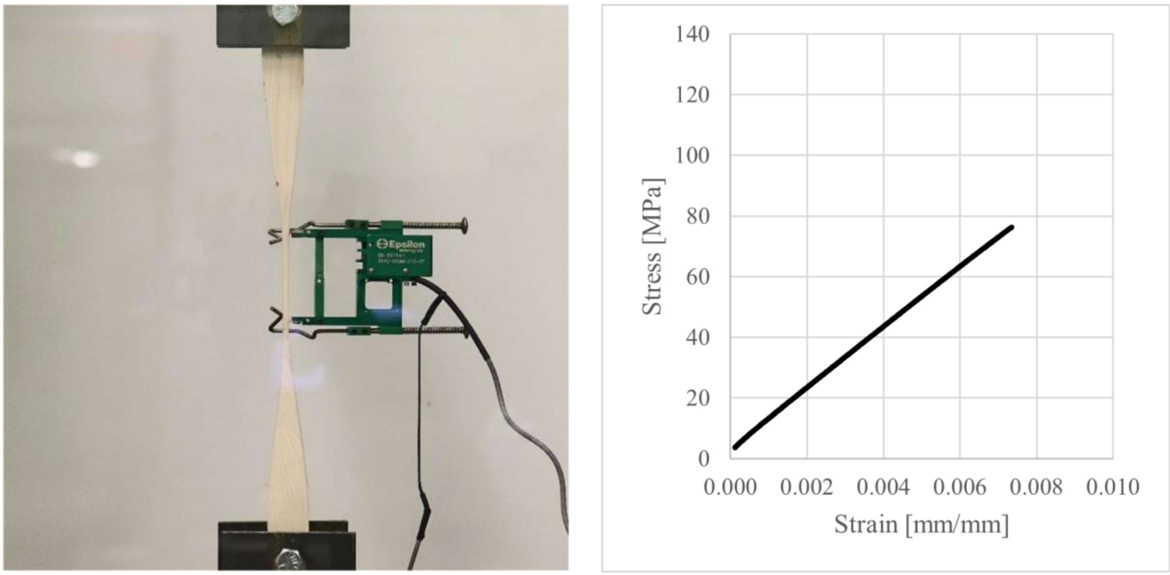

(a) Ultimate failure (b) Stress-strain behaviour

Figure B.10: Tension coupon test of ST-4

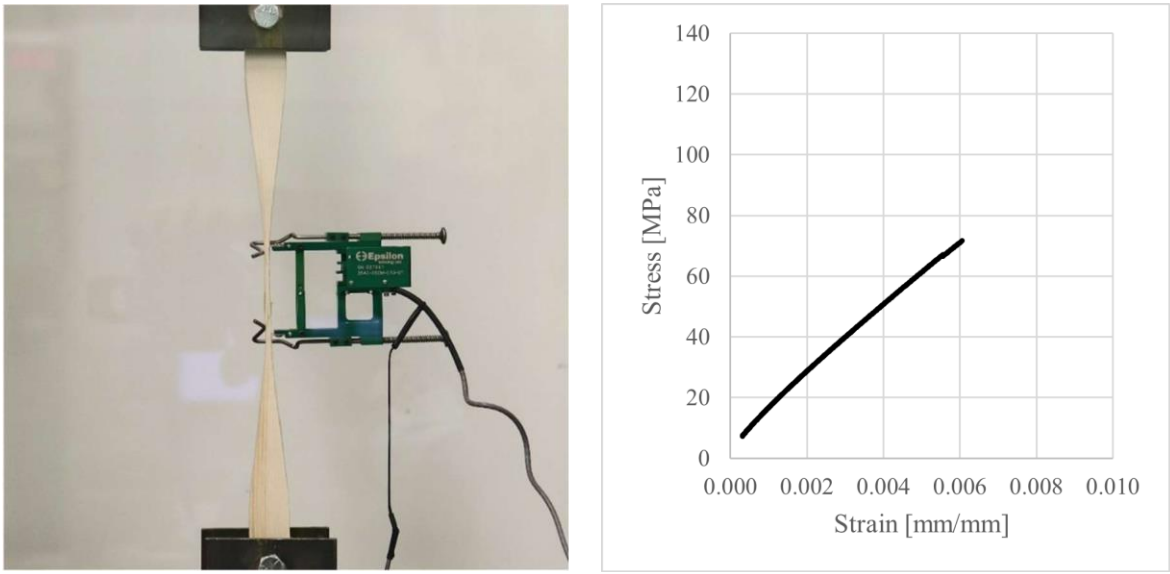

(a) Ultimate failure

(b) Stress-strain behaviour

Figure B.11: Tension coupon test of ST-5

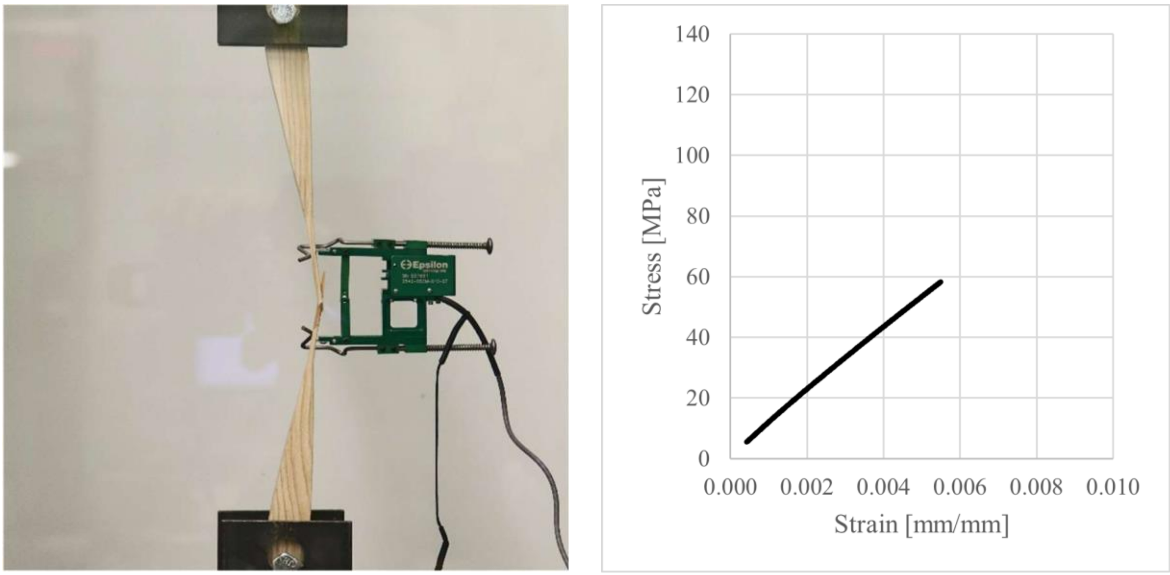

(a) Ultimate failure

(b) Stress-strain behaviour

Figure B.12: Tension coupon test of ST-6

Appendix C

Bending Test Progressions

Specimen # SN-1 **Base Material: Solid Lumber** **Reinforcement: None**

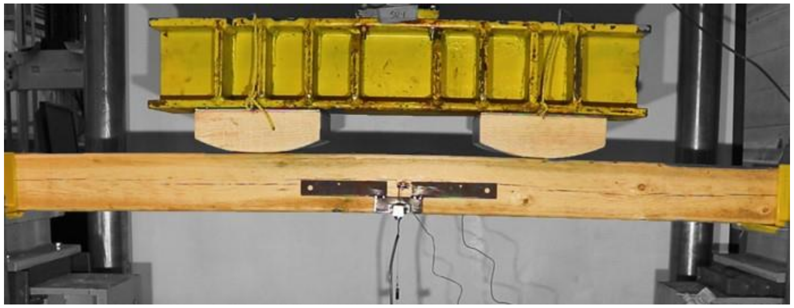

(1) Start of test

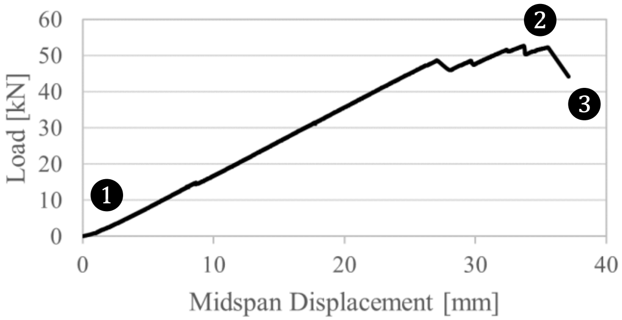

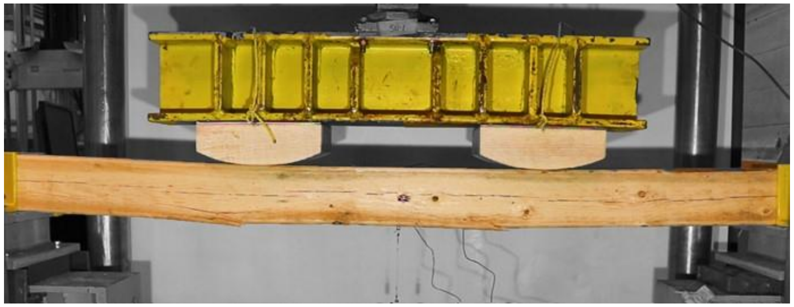

(2) Peak loading

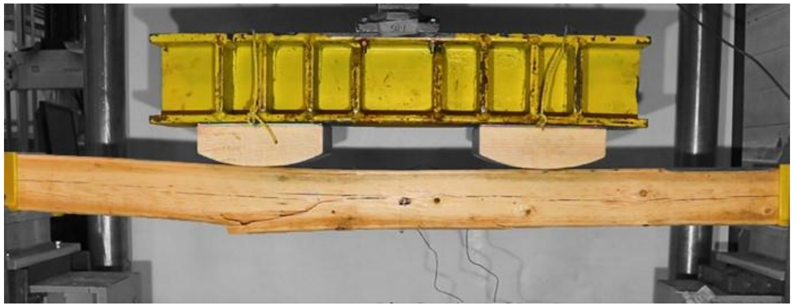

(3) Ultimate failure

Figure C.1: Flexural test progression of SN-1

Specimen # GN-1 **Base Material: Glulam** **Reinforcement: None**

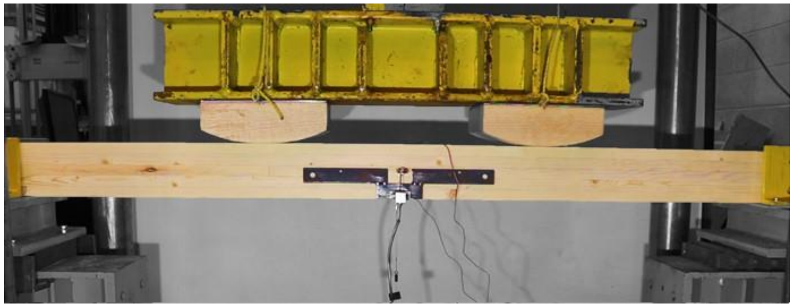
(1) Start of test

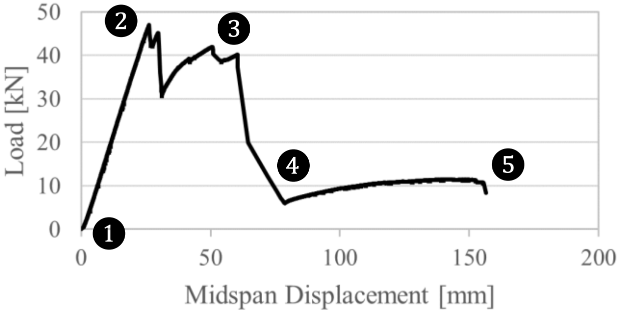

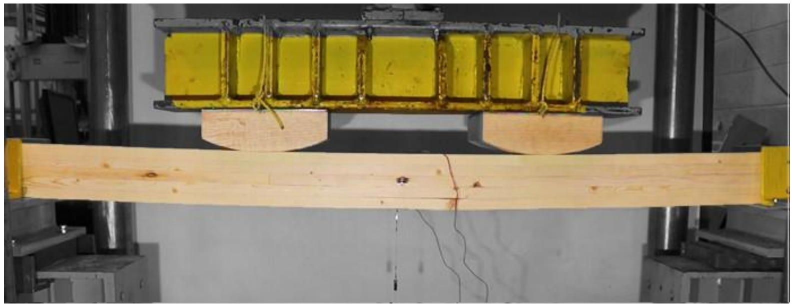
(2) Primary peak loading

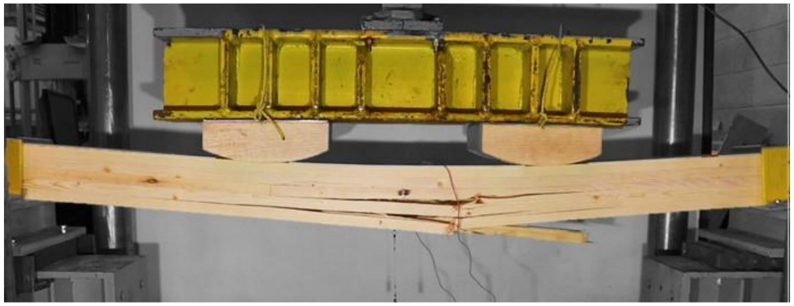
(4) Ultimate failure

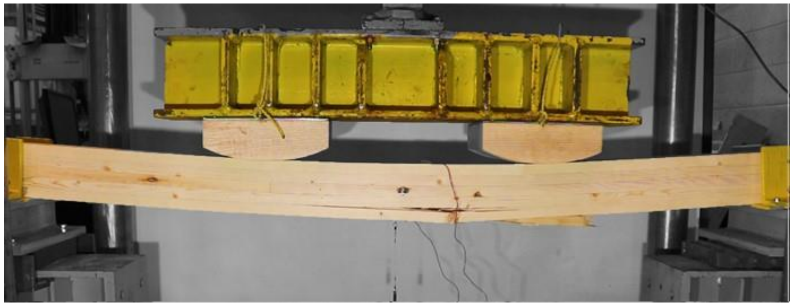
(3) Secondary peak loading

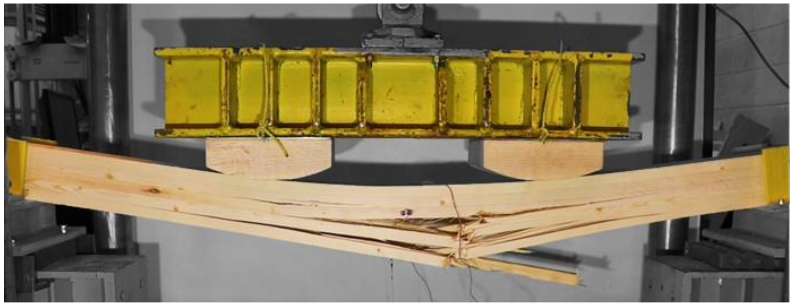
(5) End of test

Figure C.2: Flexural test progression of GN-1

Specimen # GN-2 **Base Material: Glulam** **Reinforcement: None**

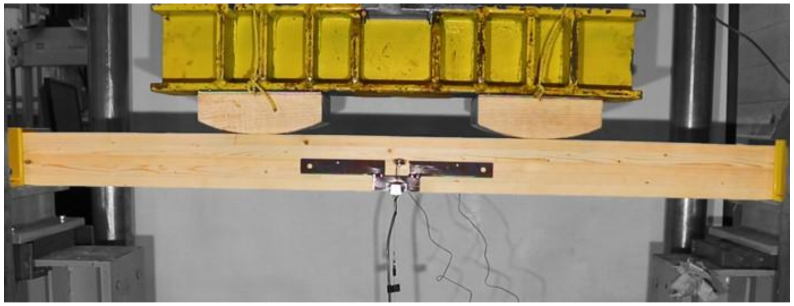

(1) Start of test

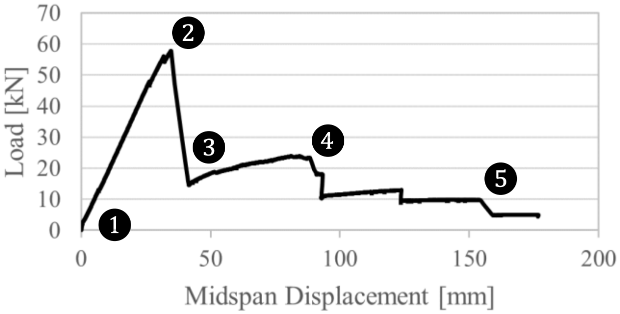

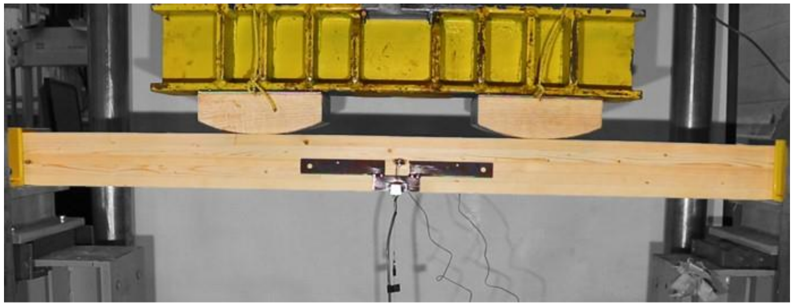

(2) Peak loading

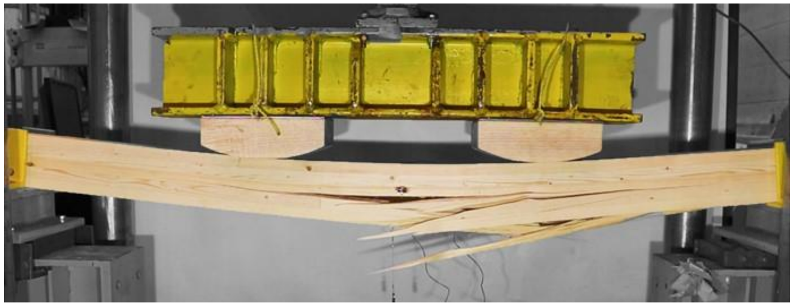

(4) Extreme tension fibre progresses upward as outer layers fail

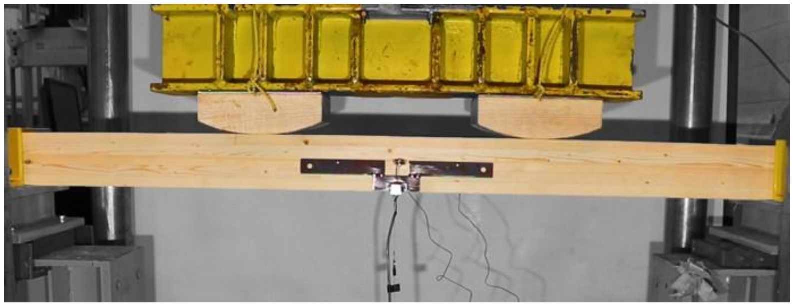

(3) Initial failure

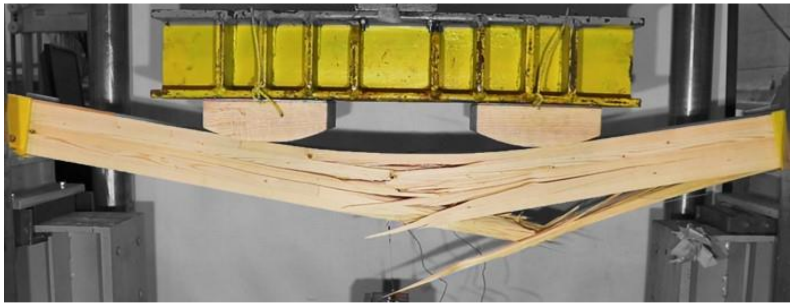

(5) End of test

Figure C.3: Flexural test progression of GN-2

Specimen # SF-1 **Base Material: Solid Lumber** **Reinforcement: FRP Fabric**

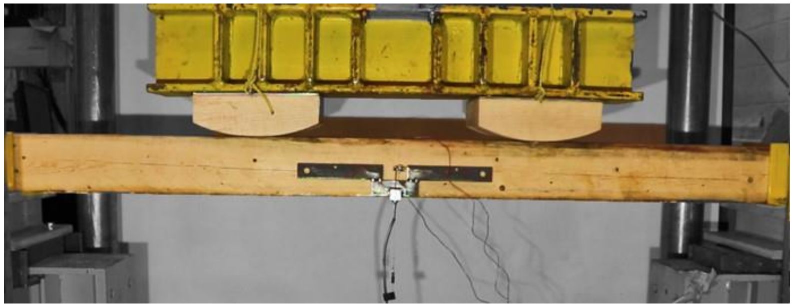

(1) Start of test

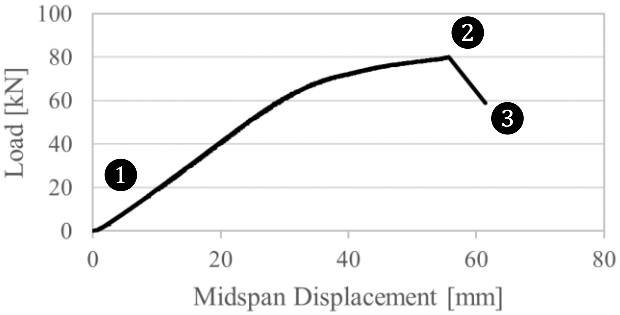

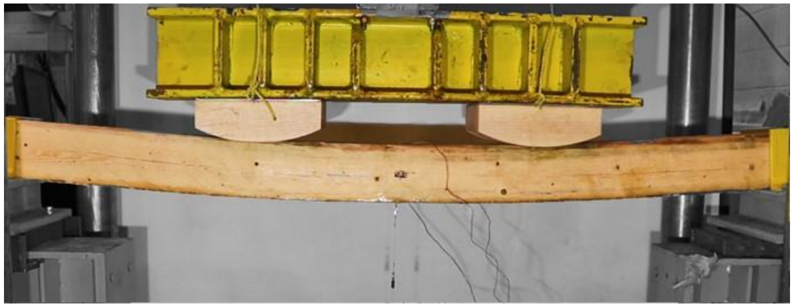

(2) Peak loading

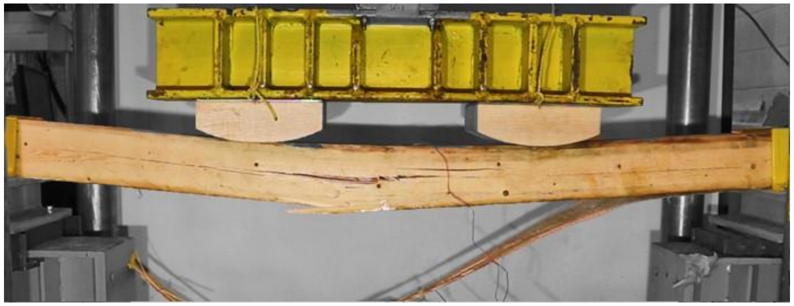

(3) Ultimate failure

Figure C.4: Flexural test progression of SF-1

Specimen # SF-2 **Base Material: Solid Lumber** **Reinforcement: FRP Fabric**

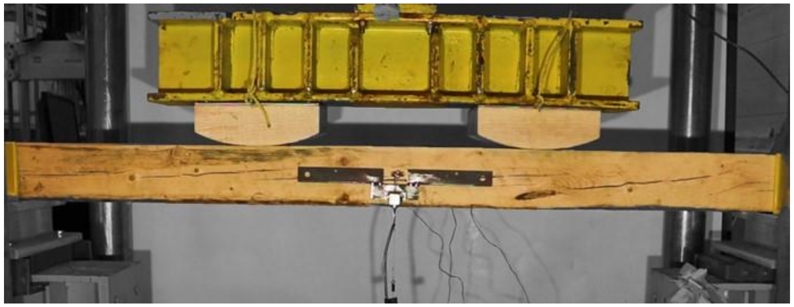

(1) Start of test

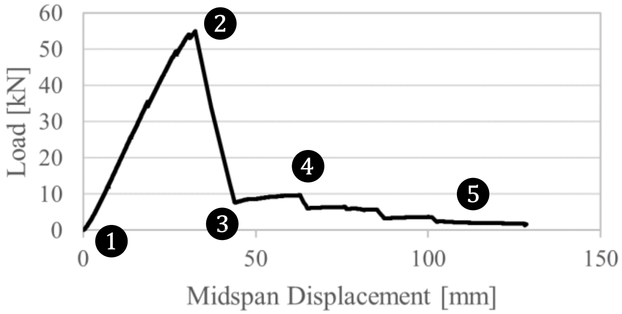

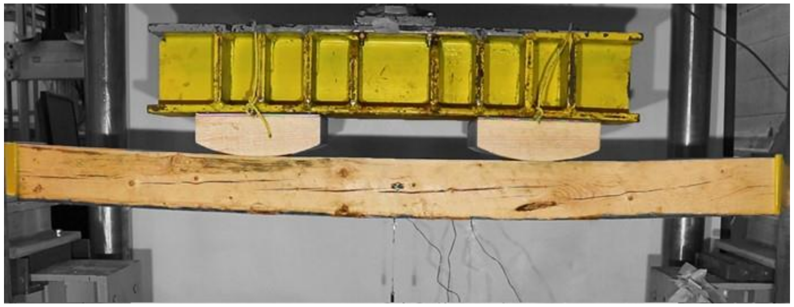

(2) Peak loading

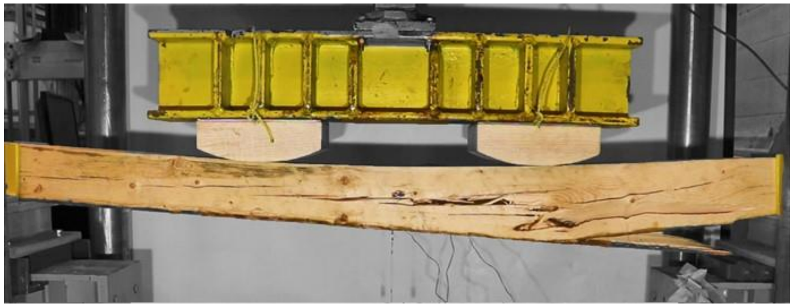

(4) Crack progresses through pre-existing surface checks

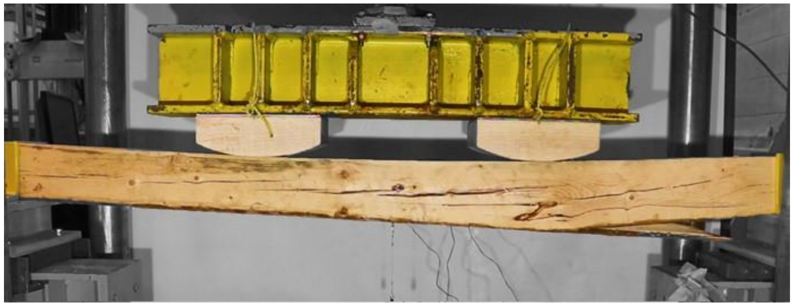

(3) Ultimate failure

(5) End of test

Figure C.5: Flexural test progression of SF-2

Specimen # GF-1 **Base Material: Glulam** **Reinforcement: FRP Fabric**

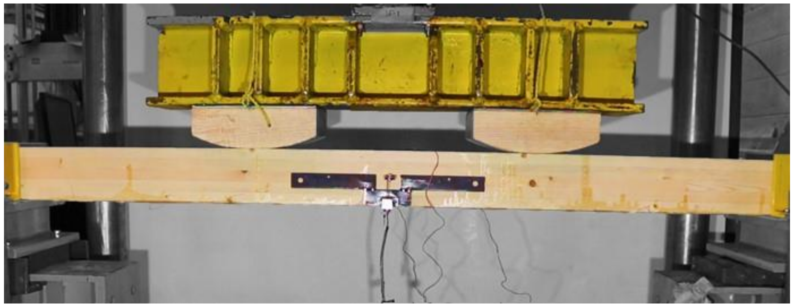

(1) Start of test

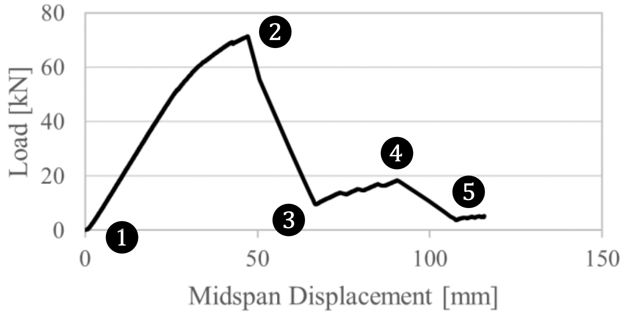

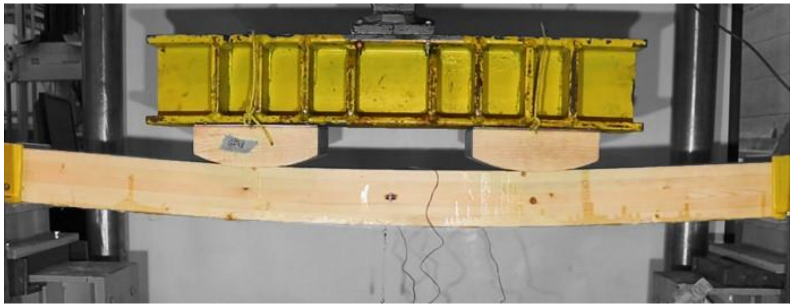

(2) Peak loading

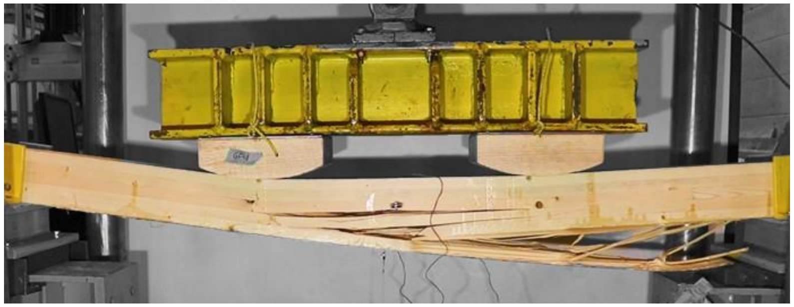

(4) Tensile rupture at mid-depth knot under left point load

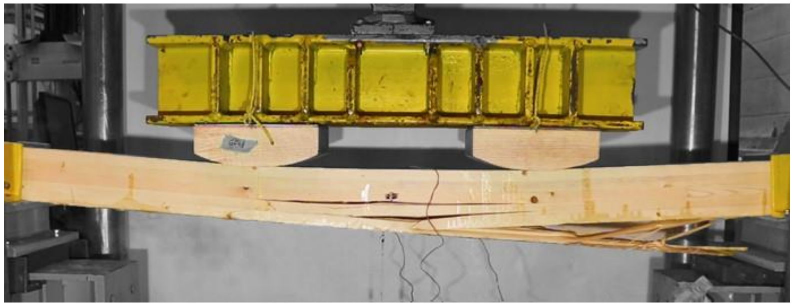

(3) Ultimate failure

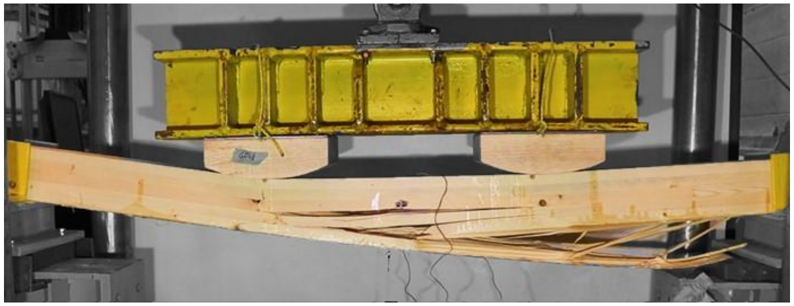

(5) End of test

Figure C.6: Flexural test progression of GF-1

Specimen # GF-2 **Base Material: Glulam** **Reinforcement: FRP Fabric**

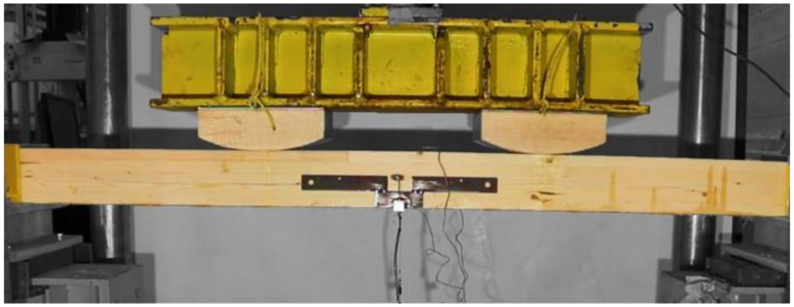

(1) Start of test

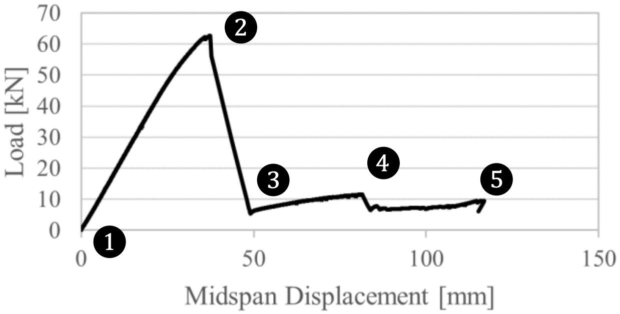

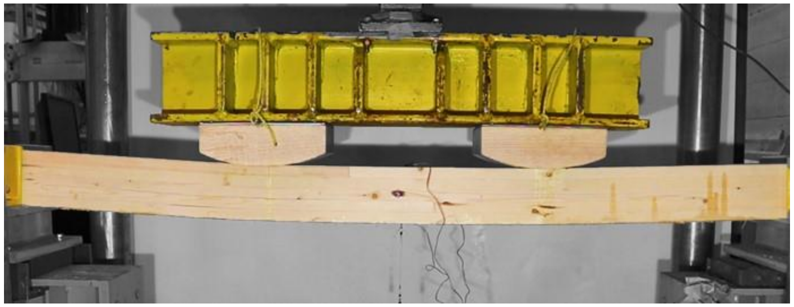

(2) Peak loading

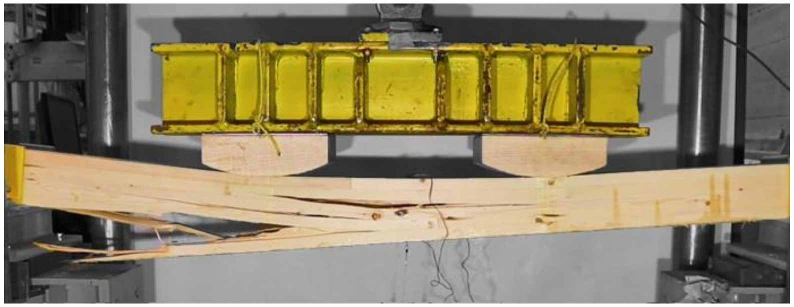

(4) Extreme tension fibre progresses upward as outer layers fail

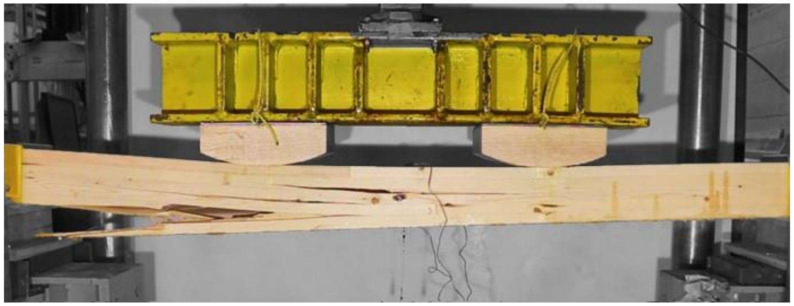

(3) Ultimate failure

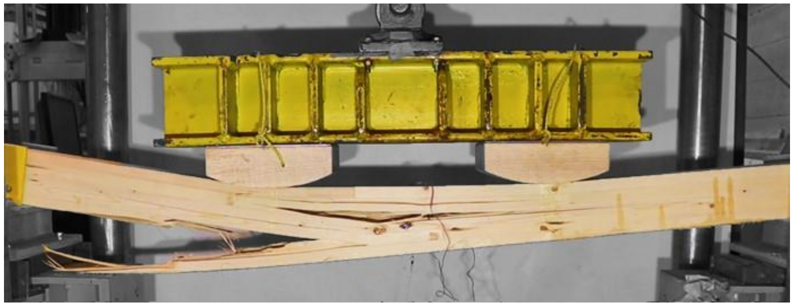

(5) End of test

Figure C.7: Flexural test progression of GF-2

Specimen # SB-1 **Base Material: Solid Lumber** **Reinforcement: FRP Bars**

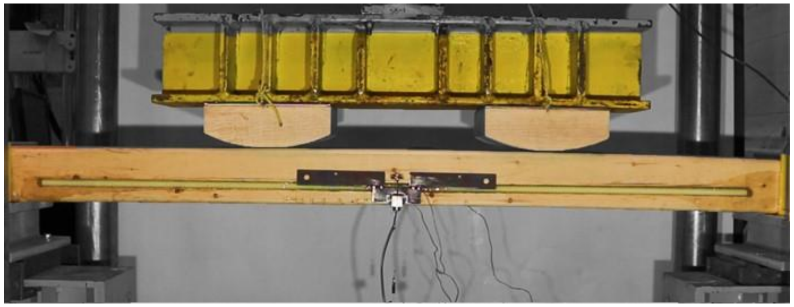
(1) Start of test

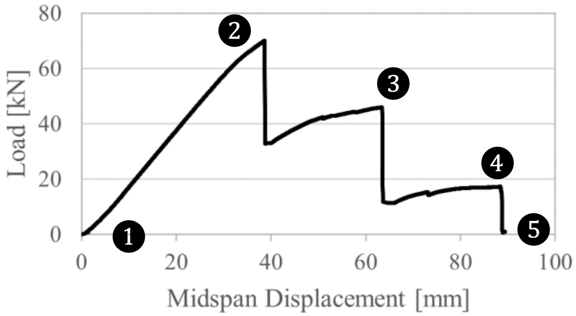

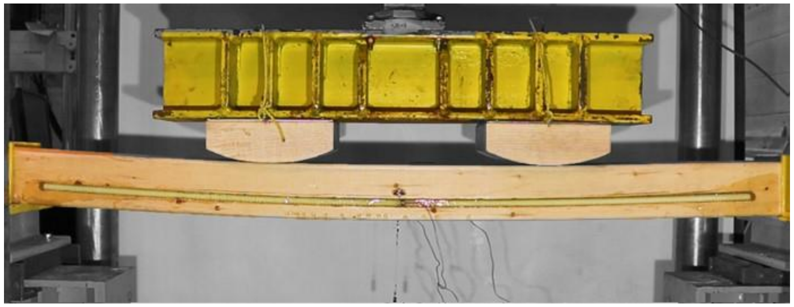
(2) Peak loading

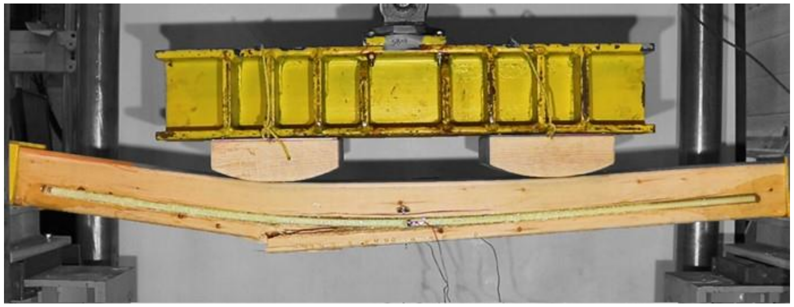
(4) Resin shattered on both sides; wood shear failure past FRP

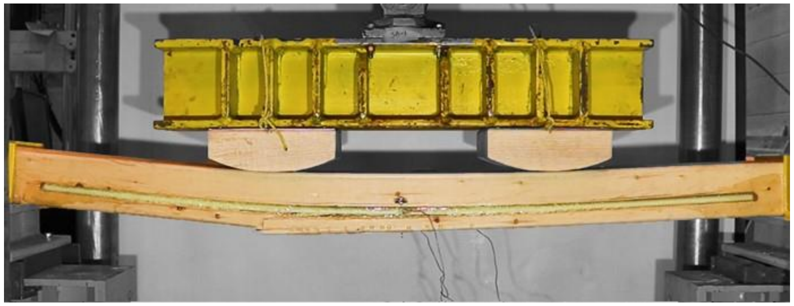
(3) Wood-cover failure; string pot disconnected

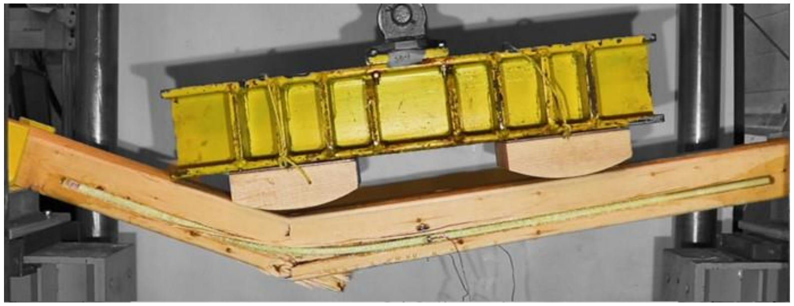
(5) End of test

Figure C.8: Flexural test progression of SB-1

Specimen # SB-2 **Base Material: Solid Lumber** **Reinforcement: FRP Bars**

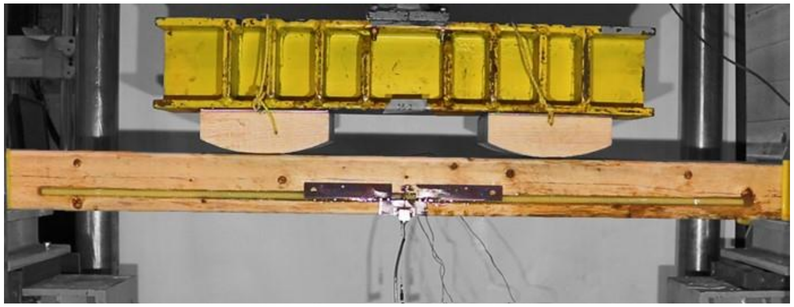

(1) Start of test

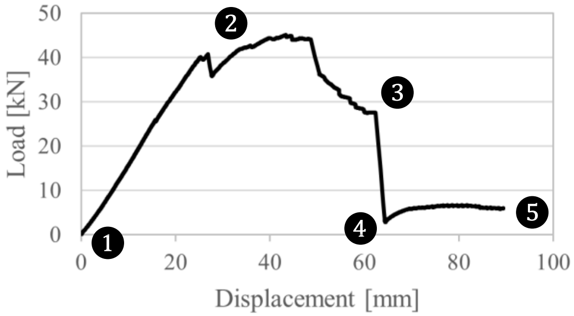

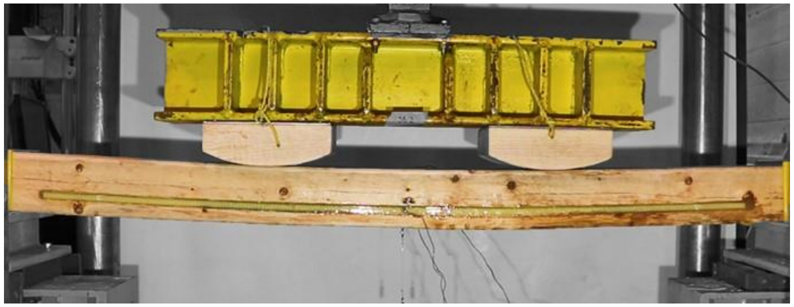

(2) Peak loading

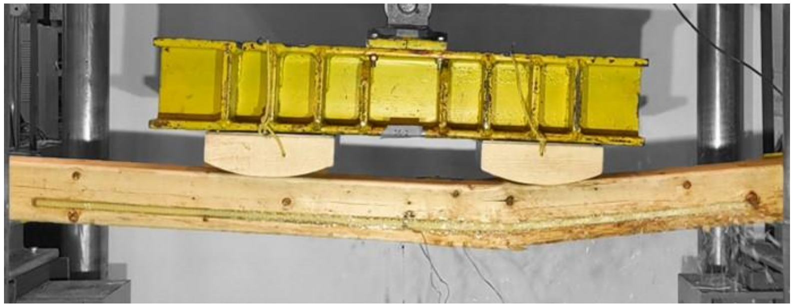

(4) Resin shatters

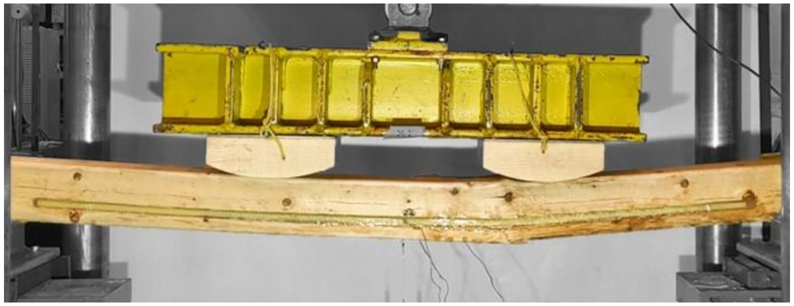

(3) Wood-cover failure

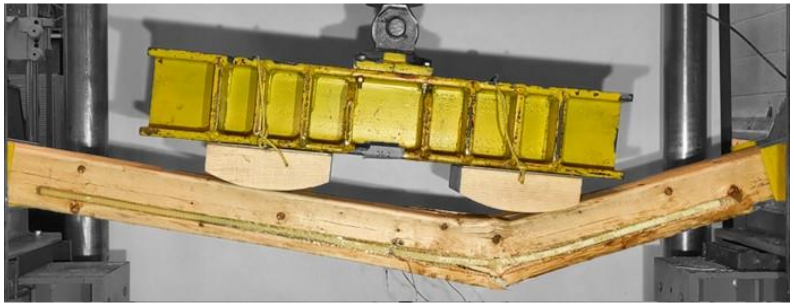

(5) End of test

Figure C.9: Flexural test progression of SB-2

Specimen # GB-1 **Base Material: Glulam** **Reinforcement: FRP Bars**

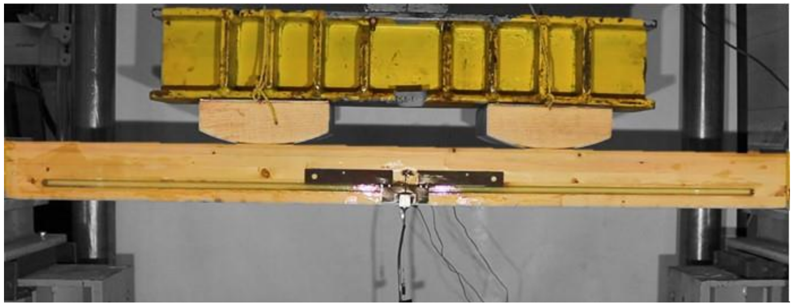

(1) Start of test

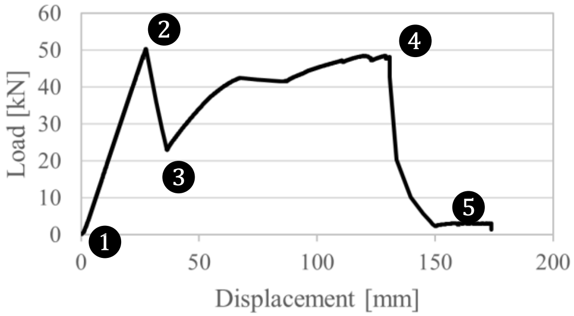

(2) Primary peak loading

(4) Secondary peak loading

(3) Wood-cover failure

(5) End of test

Figure C.10: Flexural test progression of GB-1

Specimen # GB-2 **Base Material: Glulam** **Reinforcement: FRP Bars**

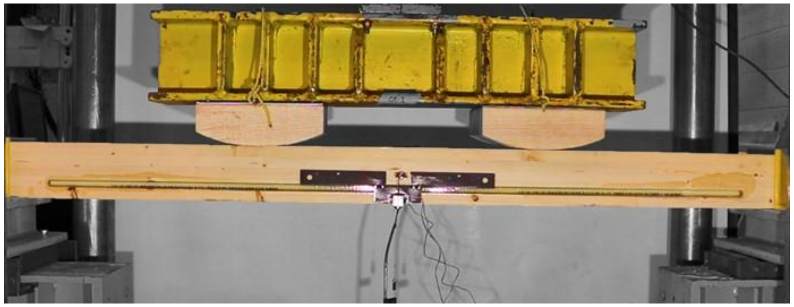

(1) Start of test

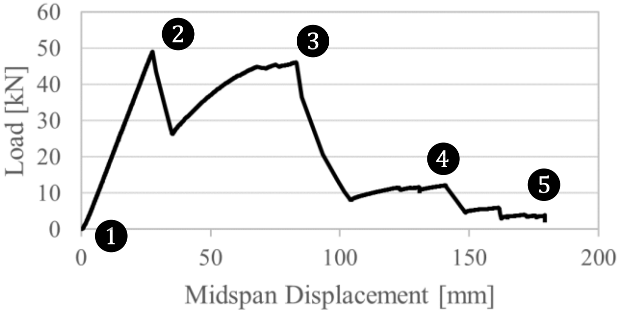

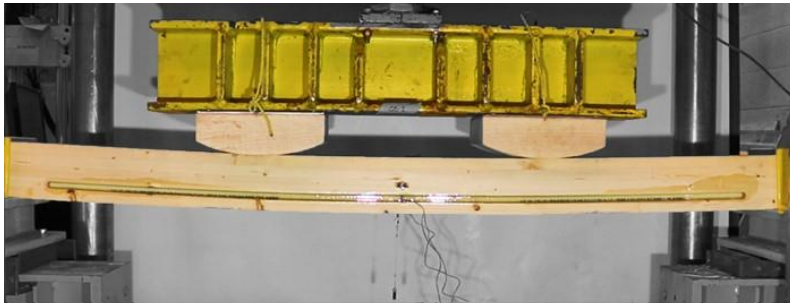

(2) Primary peak loading

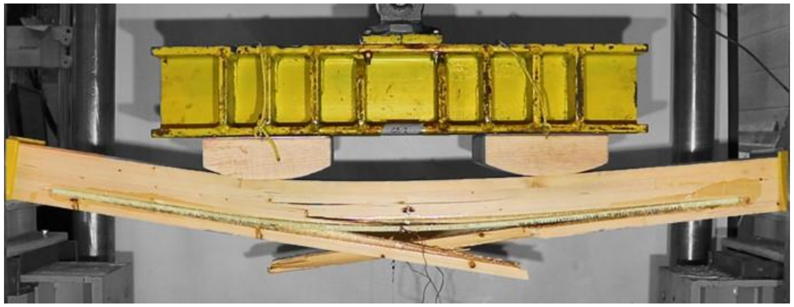

(4) Resin shattered on both sides

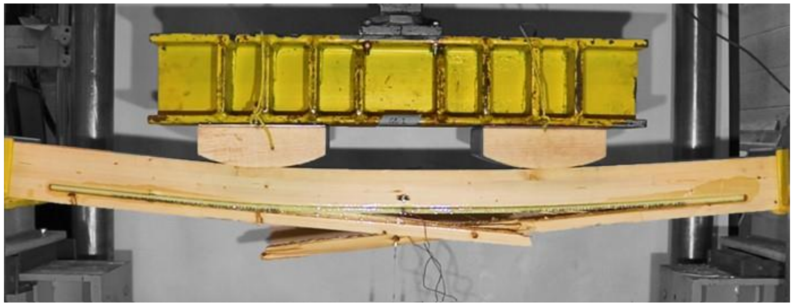

(3) Wood-cover failure; secondary peak loading

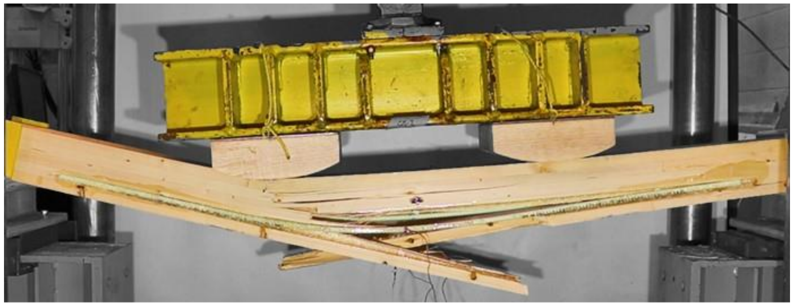

(5) End of test

Figure C.11: Flexural test progression of GB-2

Appendix D

Force and Strain Displacements

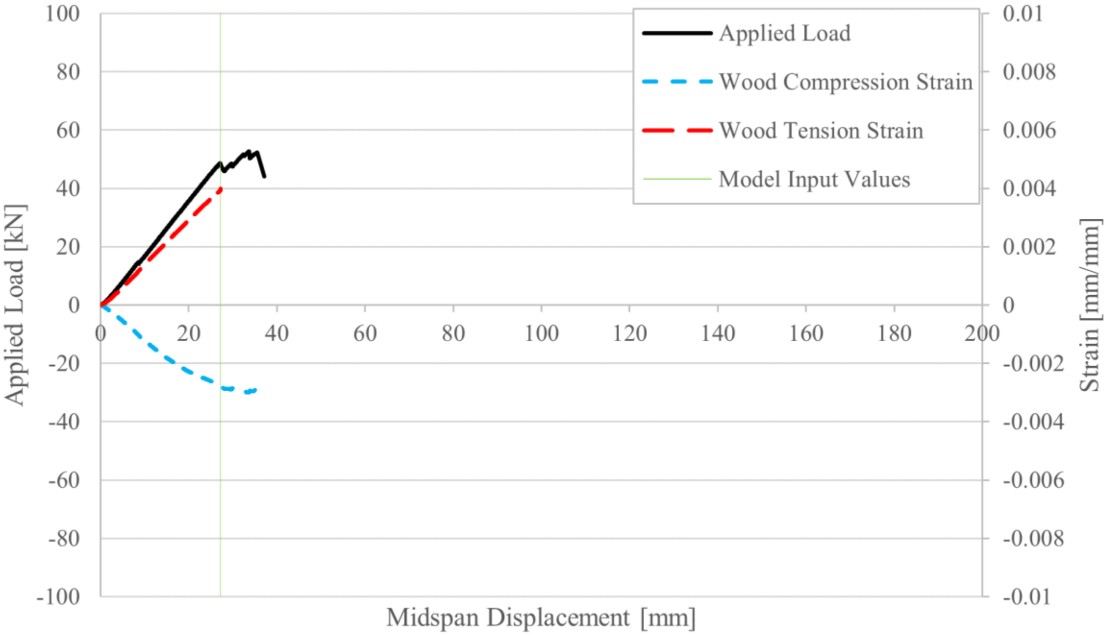

Figure D.1: Force- and strain-displacements of SN-1

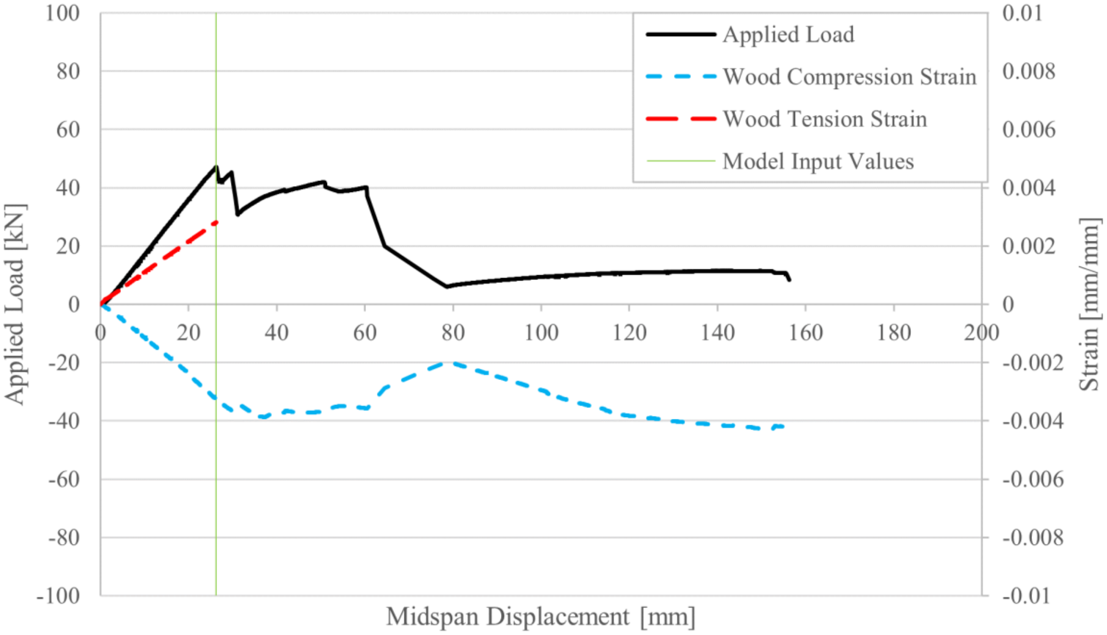

Figure D.2: Force- and strain-displacements of GN-1

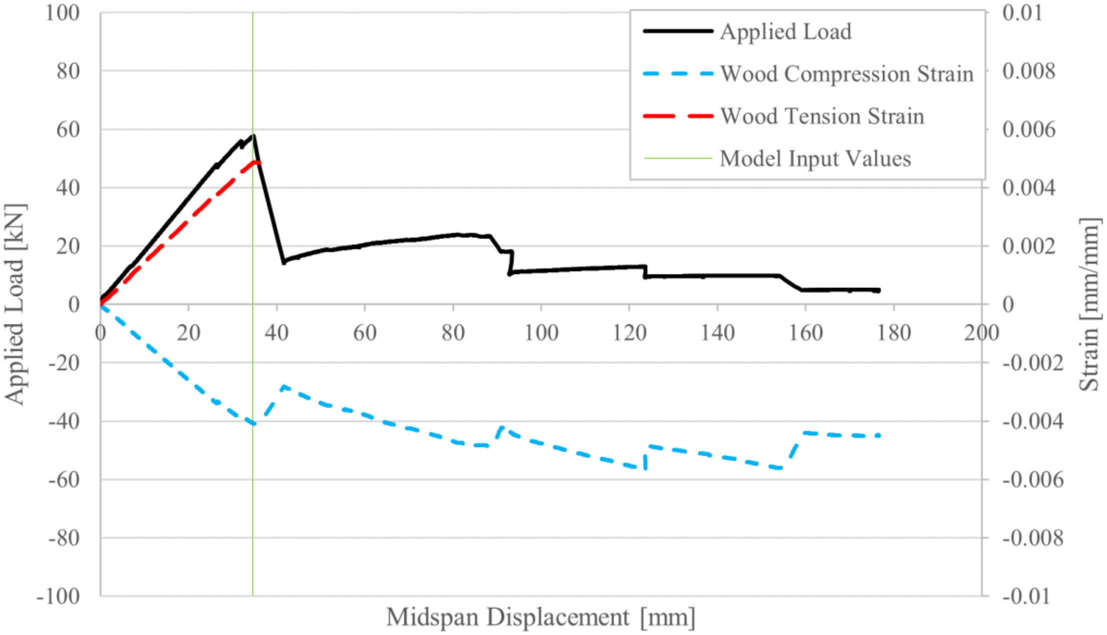

Figure D.3: Force- and strain-displacements of GN-2

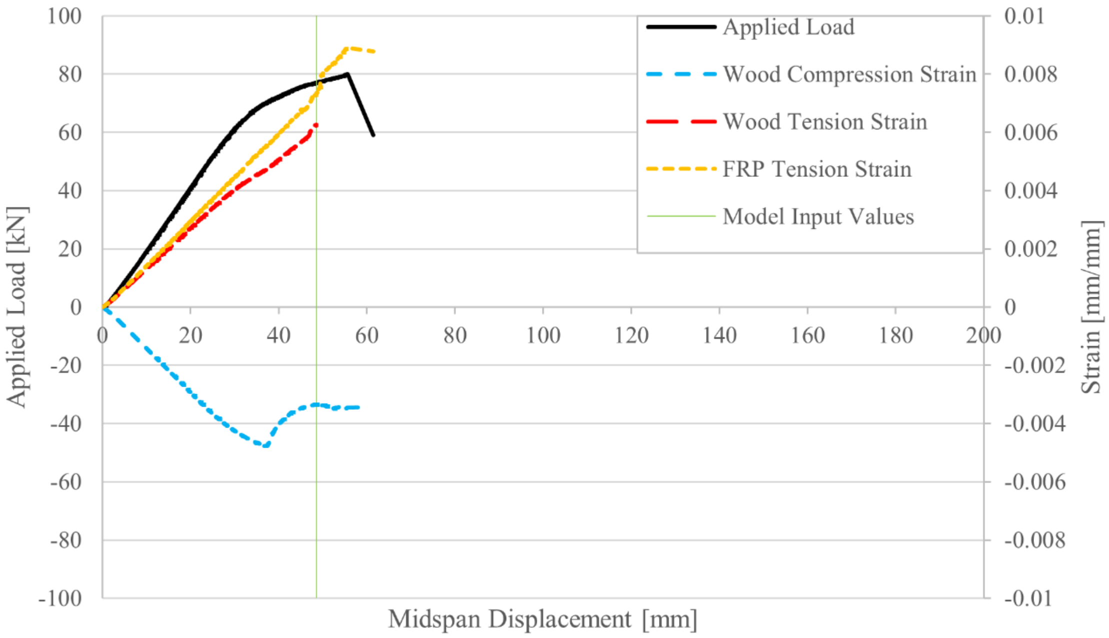

Figure D.4: Force- and strain-displacements of SF-1

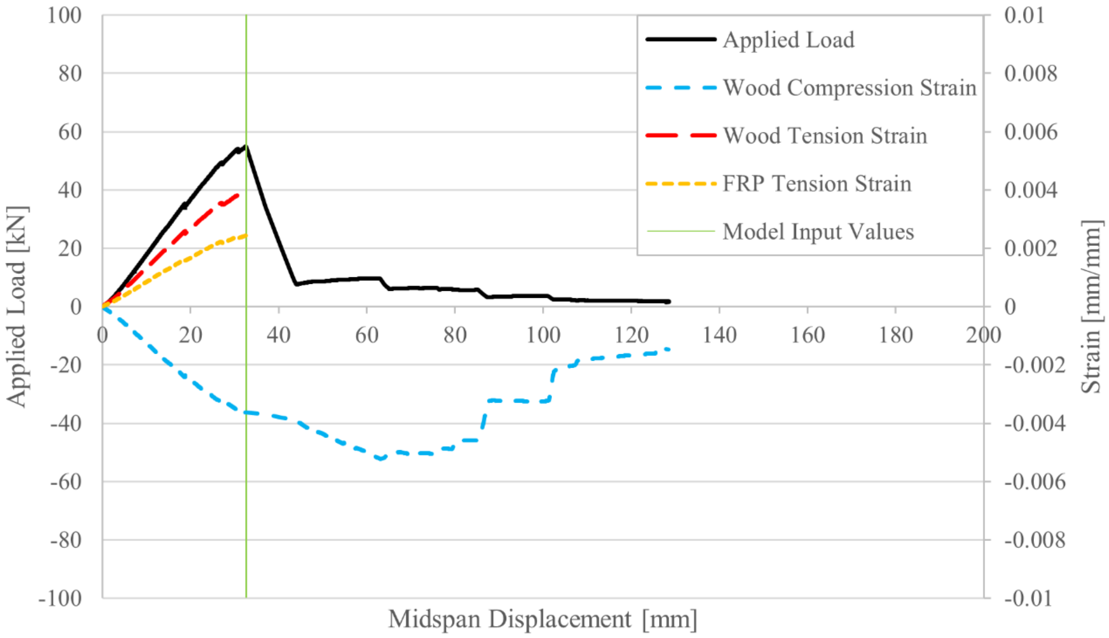

Figure D.5: Force- and strain-displacements of SF-2

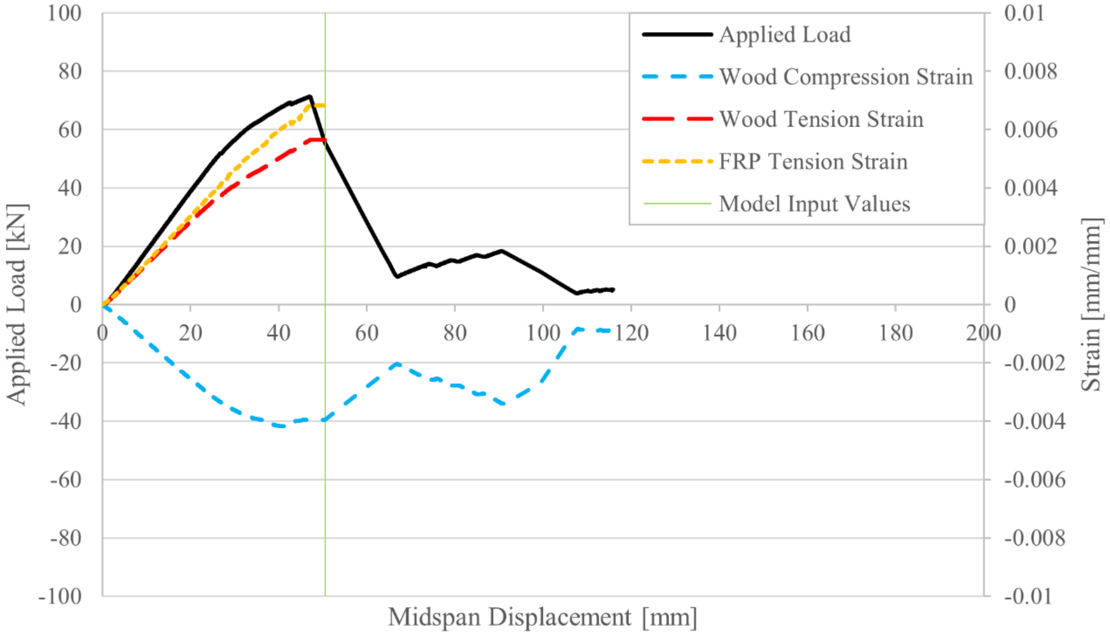

Figure D.6: Force- and strain-displacements of GF-1

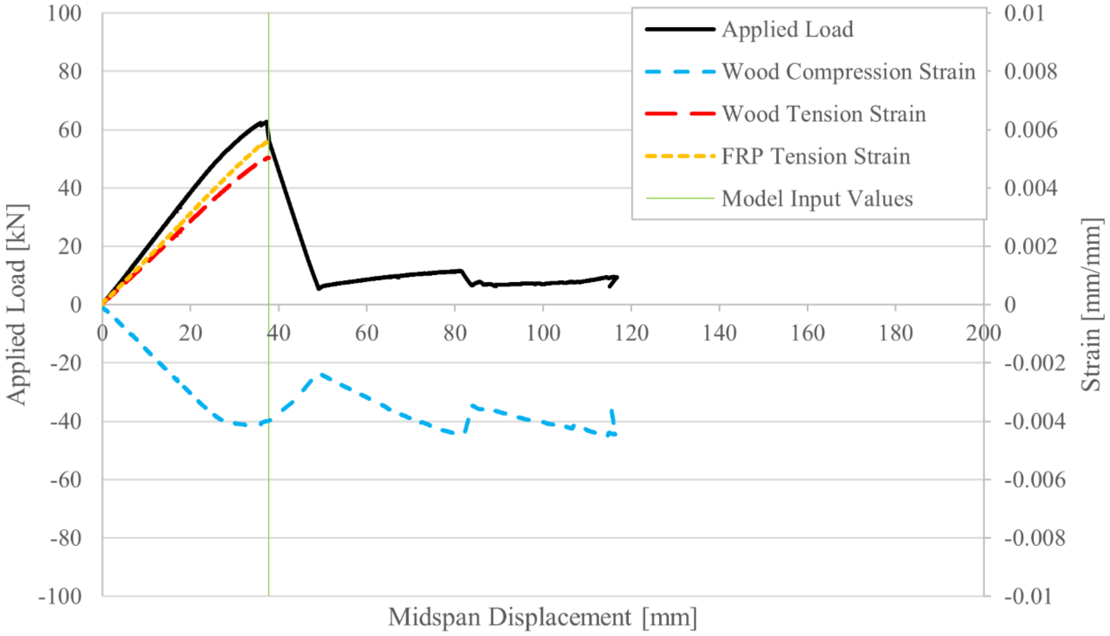

Figure D.7: Force- and strain-displacements of GF-2

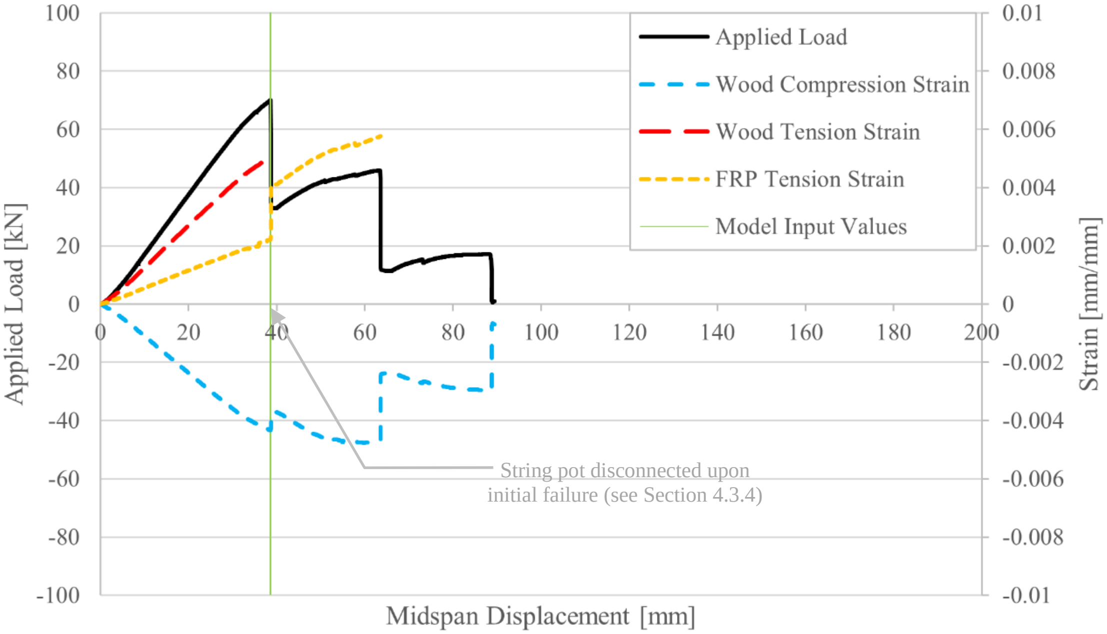

Figure D.8: Force- and strain-displacements of SB-1

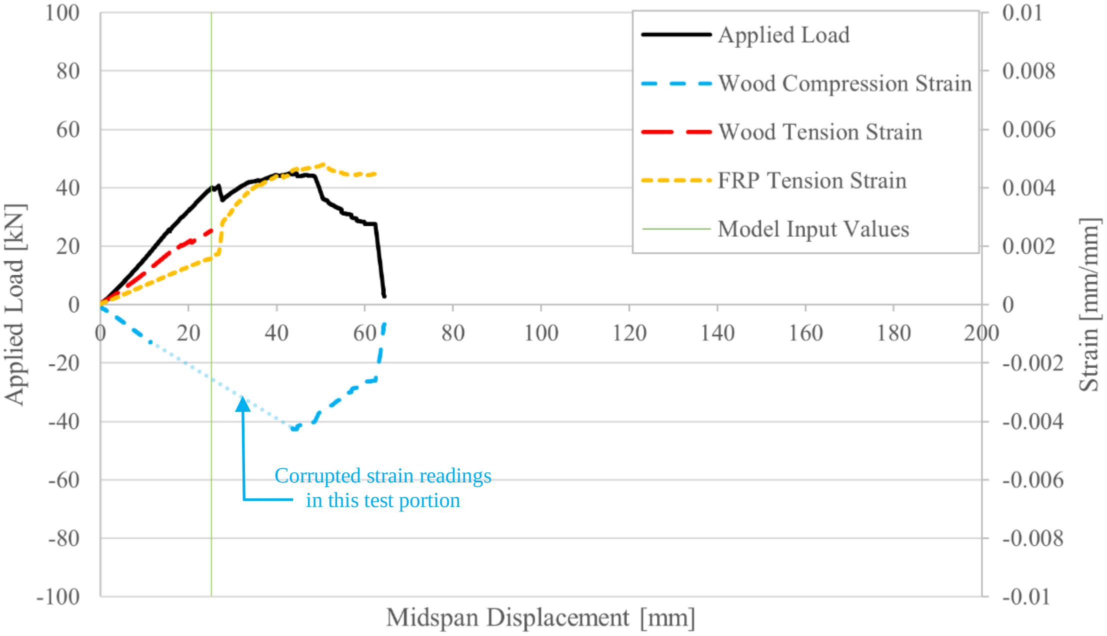

Figure D.9: Force- and strain-displacements of SB-2

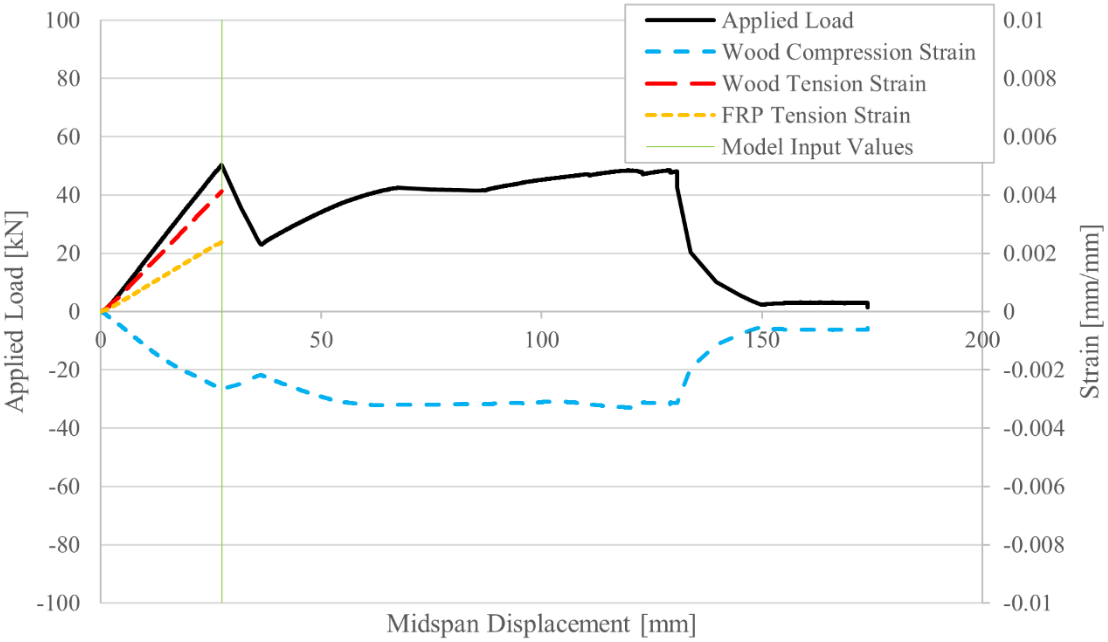

Figure D.10: Force- and strain-displacements of GB-1

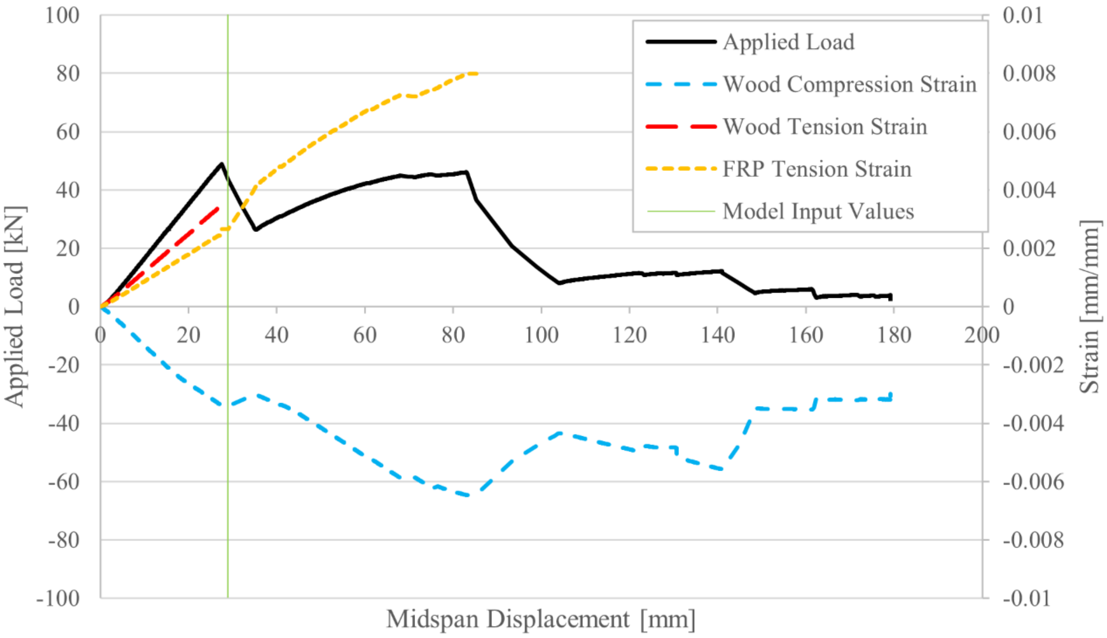

Figure D.11: Force- and strain-displacements of GB-2